INTERNATIONAL DOCTORAL
SCHOOL OF THE USC

Alexandre
Brea Rodríguez

PhD Thesis

Search for violation of leptonic universality in semileptonic decays of strange particles in LHCb

Santiago de Compostela, 2023

Doctoral Programme in Nuclear and Particles Physics

ESCOLA DE DOUTORAMENTO
INTERNACIONAL DA USC

DOCTORAL THESIS

SEARCH FOR VIOLATION OF LEPTONIC UNIVERSALITY IN SEMILEPTONIC DECAYS OF STRANGE PARTICLES IN LHCb

Author

Alexandre Brea Rodríguez

Supervisor/s: Diego Martínez Santos

Xabier Cid Vidal

Tutor: Xabier Cid Vidal

PHD PROGRAMME IN NUCLEAR AND PARTICLE PHYSICS

SANTIAGO DE COMPOSTELA

To Rocío

ABSTRACT

Theoretical studies have demonstrated that Semileptonic Hyperon Decays (SHD) can be sensitive to Beyond the Standard Model (BSM) dynamics that break leptonic flavour universality (LFU). The LFU test observable defined as the ratio between muon and electron modes

$$R^{\mu e} = \frac{\Gamma(B_1 \to B_2 \mu^- \bar{\nu}_\mu)}{\Gamma(B_1 \to B_2 e^- \bar{\nu}_e)}$$

is sensitive to non standard scalar and tensor contributions. Moreover, in the Standard Model, the dependency on the form factors is anticipated to simplify when considering the ratio, leading to a precise theoretical prediction.

$\Lambda \to p\mu^- \bar{\nu}_\mu$ was proposed as one of the most promising SHD to be studied at LHCb, due to its high acceptance efficiency and abundance in LHCb events. In addition, the electron mode has already been measured precisely and an improvement in the measurement of the$\mathcal{B}(\Lambda \to p\mu^- \bar{\nu}_\mu)$ directly translates into tighter bounds in LFU in $s \to u$ quark transitions.

In this thesis is presented the blinded measurement of the branching fraction

$$\mathcal{B}(\Lambda \to p\mu^- \bar{\nu}_\mu) = (3.485 \pm 0.059\ (stat) \pm 0.23\ (syst)) \times 10^{-4}$$

and the consequences of the precision achieved is discussed. It should be noted that this value is multiplied by a blinding constant and that the calculation of the systematic uncertainty is not completely finalized, so the final result of this uncertainty may vary slightly. The measurement is performed using Run 2 LHCb data, produced colliding protons at 13 TeV of energy in the center of mass during the years 2016-2018, reaching an integrated luminosity of 5.4 fb^{-1}.

In addition some prospects fore future SHD measurements are included.

LIMIAR

Estudos teóricos demostraron que os decaementos semileptónicos de hyperons (SHD) poden ser sensíbeis a dinámicas máis alá do modelo estándar da física de partículas que rompen a universalidade leptónica (LFU). O observábel empregado para testear a LFU, definido como a razón entre os modos muónico e electrónico

$$R^{\mu e} = \frac{\Gamma(B_1 \longrightarrow B_2 \mu^- \bar{\nu}_\mu)}{\Gamma(B_1 \longrightarrow B_2 e^- \bar{\nu}_e)},$$

é sensíble a contribucións non estándar. Ademais, no modelo estándar, a dependencia en factores de forma simplifícase ao dividir as dúas razóns de ramificación, permitindo unha predicción teórica precisa.

A canle $\Lambda \longrightarrow p\mu^- \bar{\nu}_\mu$ foi proposta como un dos SHD máis prometedores pra ser estudados en LHCb, dada a súa alta eficiencia de aceptancia e abundancia nos eventos de LHCb. A isto súmase que o modo electrónico xa foi medido con precisión, polo que unha mellora na medida do $\mathcal{B}(\Lambda \longrightarrow p\mu^- \bar{\nu}_\mu)$ tradúcese directamente en límites máis precisos da LFU en transicións dos quarks $s \longrightarrow u$.

Nesta tese preséntase a medida "a cegas" da razón de ramificación

$$\mathcal{B}(\Lambda \longrightarrow p\mu^- \bar{\nu}_\mu) = (3.485 \pm 0.059\ (stat) \pm 0.23\ (syst)) \times 10^{-4}$$

e discútense as consecuencias da precisión alcanzada. Debe terse en conta que a medida aparece multiplicada por unha constante de cegado e que o cálculo da incerteza sistemática non está completamente finalizada, polo que o resultado final desa incerteza pode variar lixeiramente. A medida foi feita empregando datos tomados no LHCb durante o chamado Run 2, producidos colisionando protóns a 13 TeV de enerxía no centro de masas entre os anos 2016 e 2018, alcanzando unha luminosidade integrada de 5.4 fb^{-1}.

Ademais engádense algunhas propostas pra medir outros SHD empregando os datos de LHCb.

CONTENTS

FOREWORD

One of the fundamental questions that has consistently intrigued us throughout time is: 'What exactly is our world made of?'. Despite remaining quite uncertain about other fundamental questions, we have made significant progress in addressing this one.

Nowadays, we know that all the matter around us is composed of atoms, with protons and neutrons in their nucleus, and electrons in quantum orbitals around them. For the first time, we gained a systematic understanding of the constituents of our world.

Yet, our journey did not culminate here; it extended deeper into the subatomic realm, revealing that protons and neutrons, once thought to be elementary particles, are themselves intricate structures composed of particles known as quarks. In our current paradigm, electrons and quarks serve as the fundamental building blocks of matter, forming the very essence of the world around us.

In our quest to delve deeper into our understanding of particles, numerous experiments have been conducted, resulting in the discovery of a vast array of particles that initially left us even more perplexed than before. Furthermore, these particles exhibited sensitivity to new fundamental interactions, the strong and weak nuclear interactions, not typically encountered in our daily experiences.

However, following significant collective theoretical efforts in the 20th century, a model describing all the known particles and their interactions, excluding gravity, was constructed. It is called Standard Model (SM), and it achieved impressive predictive power and resisted all of our attempts to uncover phenomena beyond it.

In the SM, matter is composed of particles with half-odd-integer quantum spin numbers, known as fermions, while interactions are mediated by particles with integer spin quantum numbers, referred to as bosons. It describes three fundamental interactions: electromagnetism, the strong interaction, and the weak interaction. Gravity is the only interaction that falls outside of the model.

There are two types of fermions: leptons and quarks, and we observe a similar pattern in both categories, with two types of particles (up and down quarks, and electron and electron neutrino leptons), as well as two additional, heavier-generation counterparts, known as the second and third generations.

Only quarks are affected by the strong interaction, which is mediated by gluons and confines them within mesons (typically pairs of quarks) or baryons (typically consisting of 3 quarks). In contrast, leptons do not interact with the strong interaction and can exist independently.

The photon, the particle associated with light, serves as the mediator of the electromagnetic interaction, and only charged particles can interact with it. Additionally, all fermions can interact with the $W^{\pm}$ and Z^0 bosons, which act as mediators of the weak interaction. The electromagnetic and weak interactions are, in fact, two distinct manifestations of a singular unified interaction known as the electroweak interaction. The coupling of the gauge bosons to leptons within the electroweak interaction is invariant with respect to the flavor of the lepton, a phenomenon referred to as lepton flavor universality.

In the SM, particles are initially massless and acquire mass through interactions with the Higgs field. This mechanism was proposed in 1964, and with the discovery of the Higgs boson in 2012 by the ATLAS and CMS collaborations in the Large Hadron Collider (LHC), the Standard Model was completed.

Despite the great success of the Standard Model, several well-known issues remain unexplained. Ordinary matter can only account for approximately 5 % of the observed energy in the universe, with around 25 % attributed to dark matter and approximately 70 % to dark energy. The nature of both energy sources is completely unknown as of now. Moreover, the observation of neutrino oscillations implies that they have mass, but it is not yet established how they acquire it. In addition, the observed matter-antimatter imbalance in the universe cannot be explained with the known sources of CP violation and we don't know how to fit gravity in the model.

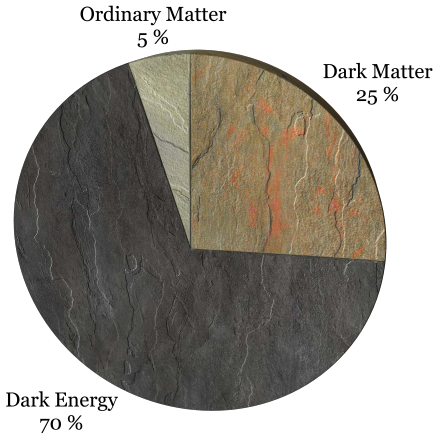

FIGURE 1: Approximate contribution from ordinary matter, dark matter and dark energy to the observed energy in the universe.

This is the context in which this thesis is framed. Semileptonic Hyperon Decays were proposed to test lepton flavor universality, one of the main features of the SM. The Λ (uds) particle is the lightest hyperon and the branching ratio of the $\Lambda \longrightarrow p\mu^{-}\bar{\nu}_{\mu}$ decay is sensitive to BSM physics since the ratio between the electronic and muonic branching fractions is precisely predicted by the SM, and the electronic mode branching ratio is accurately measured. Additionally, it can also contribute to

testing the unitarity of the CKM matrix, which will be explained in detail in the main text.

The LHC is currently our most powerful tool for testing the Standard Model in order to identify any deviations from its predictions that can give us a hint of what is going . An extensive campaign of direct and indirect searches for physics Beyond the Standard Model (BSM) is being conducted in the four major experiments at the LHC: A ToroidaL AparatuS (ATLAS), Compact Muon Solenoid (CMS), Large Hadron Collider beauty (LHCb), and A Large Ion Collider Experiment (ALICE).

Among the experiments at the LHC, LHCb is the only one capable of attempting to improve the current measurements of the $\mathcal{B}(\Lambda \to p\mu^- \bar{\nu}_\mu)$, and that it is precisely the main goal of this thesis. The measurement is done using pp collision data collected by the LHCb experiment at a centre-of-mass energy of 13 TeV in the period 2016-2018, corresponding to an integrated luminosity of 5.4 fb^{-1}.

CHAPTER 1

INTRODUCTION

The Standard Model (SM) is the theoretical framework that describes the known fundamental particles and their interactions through three of the four fundamental interactions: electromagnetic, weak and strong interactions.

In the SM, matter is composed of particles with half-odd-integer quantum spin numbers, known as fermions, while interactions are mediated by particles with integer spin quantum numbers, referred to as bosons. It describes three fundamental interactions: electromagnetism, the strong interactions, and the weak interactions. Gravity is the only force that falls outside of the model. A schematic summary of the SM particles can be found in Figure 1.1.

There are two types of fermions: leptons and quarks, and we observe a similar pattern in both categories, with two types of particles (up and down quarks, and electron and electron neutrino leptons), as well as two additional, heavier-generation counterparts, known as the second and third generations.

From a mathematical point of view, the electroweak gauge symmetry $SU(2)_W \times U(1)_Y$ is chiral and, as a consequence, quarks are organized in three left-handed doublets Q_L^i with i=1,2,3, where $Q_L^1=\begin{pmatrix} u_L \\ d_L \end{pmatrix}$, $Q_L^2=\begin{pmatrix} c_L \\ s_L \end{pmatrix}$, $Q_L^3=\begin{pmatrix} t_L \\ b_L \end{pmatrix}$ with the correspondents right-handed quark singlets u_R, d_R, c_R, s_R, t_R and b_R.

Something similar happens with the leptons, being organized in three left-handed doublets L_L^i with i=1,2,3, where $L_L^1=\begin{pmatrix} \nu_{e_L} \\ e_L \end{pmatrix}$, $L_L^2=\begin{pmatrix} \nu_{\mu_L} \\ \mu_L \end{pmatrix}$, $L_L^3=\begin{pmatrix} \nu_{\tau_L} \\ \tau_L \end{pmatrix}$ with the right-handed lepton singlets e_R, μ_R, τ_R. Notice that, from our current understanding, there are not right-handed neutrinos.

Only quarks are affected by the strong interaction, which is mediated by gluons and confines them within mesons (typically pairs of quarks) or baryons (typically consisting of 3 quarks). In contrast, leptons do not interact with gluons and can exist deconfined.

The photon, the particle associated with light, serves as the mediator of the

electromagnetic force, and only charged particles can interact with it. Additionally, all fermions can interact with the $W^{\pm}$ and Z^0 bosons, which act as mediators of the weak interaction.

In the SM, particles are initially massless and acquire mass through interactions with the Higgs field. This mechanism was proposed in 1964, and with the discovery of the Higgs boson in 2012 by the ATLAS and CMS collaborations in the Large Hadron Collider (LHC), the Standard Model was completed.

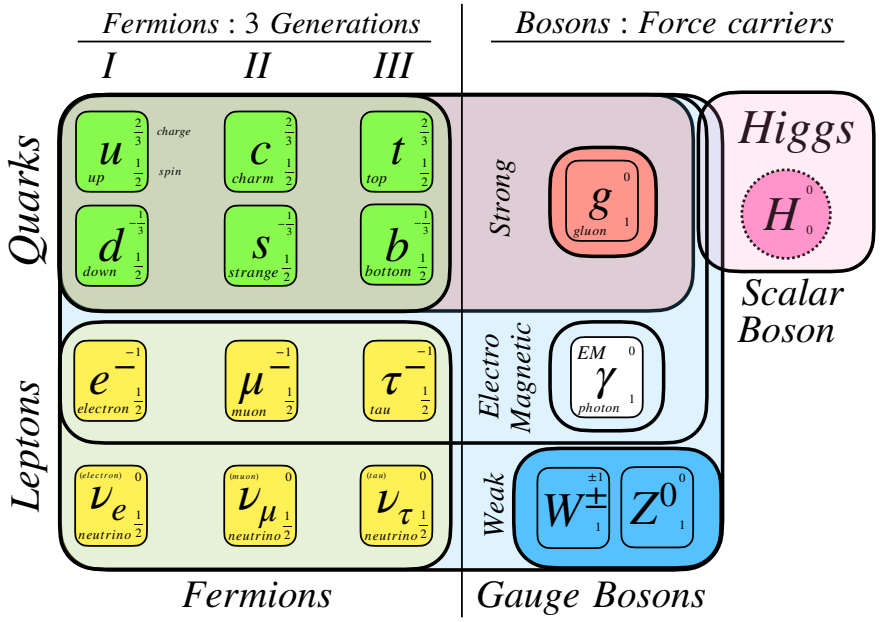

FIGURE 1.1: Standard Model particles and interactions. In the SM, every particle has a corresponding antiparticle. However, there are specific instances where a particle is its own antiparticle, such as the γ, Z^0 and Higgs bosons.

Despite the great success of the Standard Model, several well-known issues remain unexplained. Ordinary matter can only account for approximately 5 % of the observed energy in the universe, with around 25 % attributed to dark matter and approximately 70 % to dark energy. The nature of both energy sources is completely unknown as of now. Moreover, the observation of neutrino oscillations implies that they have mass, but it is not yet established how they acquire it. In addition, the observed matter-antimatter imbalance in the universe cannot be explained with the known sources of CP violation and we do not know how to fit gravity in the model.

1.1 AN ALMOST SYMMETRIC WORLD

In 1918, the mathematician Emmy Noether's proof, which showed that every differentiable symmetry of the action of a physical system subjected to conservative forces corresponds to a conservation law, was published. She had originally proved this three years earlier [62].

After Emmy Noether's groundbreaking work on symmetries and conservation laws, physicists began to delve deeper into understanding the fundamental symmetries inherent in particle interactions. These symmetries are crucial for understanding the laws that govern the subatomic world. They originate the conservation principles we observe, such as conservation of energy, momentum, and angular momentum. However, particle physics also introduces other symmetries, both exact and broken, that are not obvious at macroscopic scales.

Some of these symmetries are termed "Discrete Space-Time Symmetries", such as charge conjugation (C), parity (P), time (T), CP, and CPT. Others fall under "Number Conservation Laws", including lepton, baryon, flavor, and charge conservation.

In quantum field theories of particle physics, a charge conjugation transformation (C) is a fundamental operation that transforms a particle into its antiparticle. Meanwhile, a parity transformation (P) represents the inversion of spatial coordinates, equivalent to a point reflection.

The discovery that weak interactions do not conserve parity symmetry was shocking. This observation was first made by Chien-Shiung Wu in 1956 during her experiment on the beta decay of cobalt-60 [79]. Additionally, weak interactions also maximally violate C symmetry. This is because the charge conjugation does not change the chirality of particles. For instance, a left-handed neutrino, when subjected to charge conjugation, becomes a left-handed antineutrino, which does not participate in charged weak interactions according to the Standard Model.

To reconcile these observations, it was proposed that weak interactions would conserve the combined CP symmetry, just as the strong and electromagnetic interactions do. In other words, it was believed that if all particles in a process were swapped with their antiparticles, it would mirror the initial process, thereby conserving the combined CP-symmetry in weak interactions. Nonetheless, subsequent experiments revealed that this symmetry is slightly violated in specific weak decay processes. CP-violation is responsible for the matter-antimatter imbalance in our universe. However, the degree of CP violation observed within the SM so far is not large enough to explain the observed matter-antimatter asymmetry [74].

Invariance under the combined transformation CPT is required by general principles of relativistic field theory and implies that masses and lifetimes of a particle and its anti-particle must be equal. As as consequence, CP and T violation are equivalent.

1.2 FLAVOR STRUCTURE OF THE STANDARD MODEL

As it can be seen in Fig. 1.1, there are six types of quarks and six types of leptons. Each type is considered a different "flavor". Flavor is conserved in strong and electromagnetic interactions. But, through charged current weak interactions, quarks and

leptons can change from one flavor to another. A very well known example is the beta decay in atomic nuclei, where a neutron decays into a proton, an electron and an electron neutrino. In fact, the fundamental process that is going on is

$$d \rightarrow u\, e^-\, \overline{\nu}_e \tag{1.1}$$

where the d quark decays to an up type quark via the exchange of a W^- boson. A common way to visualize it is using a Feynman diagram:

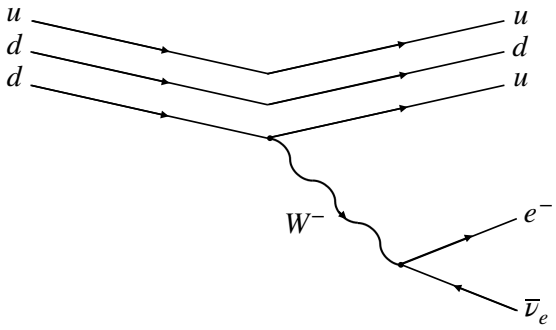

FIGURE 1.2: Feynman diagram of a neutron beta decay.

Notice that this decay is completely analogous to the semileptonic hyperon decay that we aim to study, denoted as $\Lambda \rightarrow p\mu^-\bar{\nu}_\mu$. The only differences are that in our case we study an $s \rightarrow u$ transition and that the leptons in the final state belong to the second generation. To clarify, "semileptonic" means that in the final state we have a lepton, its associated neutrino, and a hadron. A hyperon is any baryon containing one or more strange quarks, but no charm, bottom, or top quark, being the Λ the lightest of them.

The SM lagrangian can be splitted in two terms:

$$\mathcal{L}_{\text{SM}} = \mathcal{L}_{\text{Gauge}}(A_a, \Psi_i) \; + \mathcal{L}_{\text{Higgs}}(H, A_a, \Psi_i) \tag{1.2}$$

In the gauge part, we identify 3 identical replica of the basic fermion family $[\Psi = Q_L, u_R, d_R, L_L, e_R]$ and we observe a huge flavor degeneracy.

$$\mathcal{L}_{\text{Gauge}} = \sum_a -\frac{1}{4g_a^2}(F^a_{\mu\nu})^2 + \sum_\Psi \sum_{i=1,2,3} \overline{\Psi}_i i \not{D} \Psi_i \tag{1.3}$$

The Gauge lagrangian is invariant under 5 independent U(3) global rotations for each of the independent fermion fields:

$$Q^i_L \rightarrow U^{ij} Q^j_L \tag{1.4}$$

Within the SM, the flavor-degeneracy is broken only by the Yukawa interaction. In the quark sector

$$\mathcal{L}_Y = -Y^d_{ij}\overline{Q^I_{Li}}\;\phi\; d^I_{Rj} \; - Y^u_{ij}\overline{Q^I_{Li}}\epsilon\;\phi^*\; u^I_{Rj} \; + \; h.c. \tag{1.5}$$

where $Y^{u,d}$ are 3×3 complex matrices, ϕ is the Higgs field, i, j are the generation labels, ϵ is the 2×2 anti-symmetric tensor and "h.c." stands for the Hermitian conjugate, which gives the corresponding term for the W^- boson [73].

The residual flavor symmetry allows us to choose a gauge-invariant flavor basis where only one of the two Yukawa couplings is diagonal. We can choose $Y^d = diag(y_d, y_s, y_b)$ and $Y^u = V^+ \times diag(y_u, y_c, y_t)$ or $Y^d = V \times diag(y_d, y_s, y_b)$ and $Y^u = diag(y_u, y_c, y_t)$, where V is a unitary matrix.

To diagonalize also the second matrix we need to rotate separately u_L and d_L, so we do not have a gauge-invariant basis. This V matrix appears in charged-current gauge interactions.

This charged-current interactions, mediated by a $W^\pm$ boson can be written as

$$J^\mu_W = \frac{-g}{\sqrt{2}} \, \overline{u}_L \, \gamma^\mu W^+_\mu \, V_{CKM} \, d_L + h.c. \tag{1.6}$$

which basically means that the weak interactions couples to pairs $\begin{pmatrix} u \\ d' \end{pmatrix}$, $\begin{pmatrix} c \\ s' \end{pmatrix}$ and $\begin{pmatrix} t \\ b' \end{pmatrix}$, where d', s' and b' are linear combinations of the physical d, s, b:

$$\begin{pmatrix} d' \\ s' \\ b' \end{pmatrix} = \begin{pmatrix} V_{ud} & V_{us} & V_{ub} \\ V_{cd} & V_{cs} & V_{cb} \\ V_{td} & V_{ts} & V_{tb} \end{pmatrix} \begin{pmatrix} d \\ s \\ b \end{pmatrix} \tag{1.7}$$

This non-trivial mixing arises solely from the Higgs sector. Only interactions mediated by $W^\pm$ and h interactions are flavor physics. Note that the rotation of the right-handed sector is not observable and neutral currents remain flavor diagonal.

The 3×3 quark-mixing unitary matrix in question is termed the CKM matrix, named after Cabibbo, Kobayashi, and Maskawa. Originally, Cabibbo proposed this matrix structure for two generations in 1963. A decade later, Kobayashi and Maskawa extended this formulation to accommodate three generations. Essentially, the CKM matrix encapsulates information regarding the strength of flavor-changing weak interactions. Each element of the matrix signifies the probability amplitude for a transition from one quark flavor j to another quark flavor i. The probabilities of these transitions are proportional to $|V_{ij}|^2$.

Up to this point, we have consistently observed that the leptonic generation number (often simply referred to as the lepton number) is conserved in particle decays. For instance, in our $\Lambda \longrightarrow p\mu^-\bar{\nu}_\mu$ decay, we do not need to identify the specific flavor of the anti-neutrino in the final state to ascertain that it's an anti-muon neutrino, since the muonic lepton number in the initial state is 0. In a hypothetical scenario where cross-generational quark transitions do not occur, quantities such as 'upness' plus 'downness' would be conserved, similar to how the electron number is conserved. Likewise, 'strangeness' plus 'charm' and 'topness' plus 'bottomness' would also be conserved. Such a world would be described by a CKM matrix that is simply the identity matrix.

In fact, the CKM matrix is very close to the identity matrix, being the numbers in the diagonal extremely close to 1. The world average of the CKM elements is [78]:

$$V_{CKM} = \begin{pmatrix} V_{ud} & V_{us} & V_{ub} \\ V_{cd} & V_{cs} & V_{cb} \\ V_{td} & V_{ts} & V_{tb} \end{pmatrix} \tag{1.8}$$

$$\begin{pmatrix} |V_{ud}| & |V_{us}| & |V_{ub}| \\ |V_{cd}| & |V_{cs}| & |V_{cb}| \\ |V_{td}| & |V_{ts}| & |V_{tb}| \end{pmatrix} = \begin{pmatrix} 0.97435 \pm 0.00016 & 0.22500 \pm 0.00067 & 0.00369 \pm 0.00011 \\ 0.22486 \pm 0.00067 & 0.97349 \pm 0.00016 & 0.04182^{+0.00085}_{-0.00074} \\ 0.00857^{+0.00020}_{-0.00018} & 0.04110^{+0.00083}_{-0.00072} & 0.999118^{+0.000031}_{-0.000036} \end{pmatrix} \tag{1.9}$$

One can easily observe that $|V_{us}|$ and $|V_{cd}|$ are similar in magnitude and both are larger than $|V_{cb}|$ and $|V_{ts}|$, which are also comparable to each other. Transitions that involve changing two generations, such as $|V_{ub}|$ and $|V_{td}|$, are greatly suppressed.

The CKM matrix can be parameterized by three mixing angles and a CP-violating phase. A standard parameterization employs three Euler angles (θ_{12}, θ_{23} and θ_{13}) and one CP-violating phase (δ_{13}) [27]. The angle θ_{12} is known as the Cabibbo angle, which he originally introduced to explain quark mixing in the first two generations. The cosines and sines of these angles are denoted as c_{jk} and s_{jk}, respectively.

$$V_{CKM} = \begin{pmatrix} 1 & 0 & 0 \\ 0 & c_{23} & s_{23} \\ 0 & -s_{23} & c_{23} \end{pmatrix} \begin{pmatrix} c_{13} & 0 & s_{13}e^{-i\delta_{13}} \\ 0 & 1 & 0 \\ -s_{13}e^{-i\delta_{13}} & 0 & c_{13} \end{pmatrix} \begin{pmatrix} c_{12} & s_{12} & 0 \\ -s_{12} & c_{12} & 0 \\ 0 & 0 & 1 \end{pmatrix} \tag{1.10}$$

$$V_{CKM} = \begin{pmatrix} c_{12}c_{13} & s_{12}c_{13} & s_{13}e^{-i\delta_{13}} \\ -s_{12}c_{23} - c_{12}s_{23}s_{13}e^{i\delta_{13}} & c_{12}c_{13} - s_{12}s_{23}s_{13}e^{i\delta_{13}} & s_{23}c_{13} \\ s_{12}s_{23} - c_{12}c_{23}s_{13}e^{i\delta_{13}} & -c_{12}s_{13} - s_{12}c_{23}s_{13}e^{i\delta_{13}} & c_{23}c_{13} \end{pmatrix} \tag{1.11}$$

where $sin\,\theta_{12} = 0.22650 \pm 0.00048$, $sin\,\theta_{13} = 0.00361^{+0.00011}_{-0.00009}$, $sin\,\theta_{23} = 0.04053^{+0.00083}_{-0.00061}$ and $\delta = 1.196^{+0.045}_{-0.043}$.

The angles θ_{ij} are chosen to lie in the first quadrant, and the δ phase accounts for all CP-violating phenomena in flavor-changing processes within the SM.

Another possible parametrization is in terms of the four Wolfenstein parameters: λ, A, ρ, η [77].

$$V_{CKM} = \begin{pmatrix} 1 - \frac{\lambda^2}{2} & \lambda & A\lambda^3(\rho - i\eta) \\ -\lambda & 1 - \frac{\lambda^2}{2} & A\lambda^2 \\ A\lambda^3(1 - \rho - i\eta) & -A\lambda^2 & 1 \end{pmatrix} + O(\lambda^4) \tag{1.12}$$

This parameterization captures the hierarchical structure of the CKM matrix elements.

In the Standard Model, if the $SU(2)_L \times U(1)_y$ gauge symmetry were exact and unbroken, all quarks would remain massless, implying that the interaction (or flavor) eigenbasis and the mass eigenbasis would coincide. However, in the Standard Model, this gauge symmetry is spontaneously broken due to the non-zero vacuum expectation value (VEV) acquired by the Higgs doublet, leading to the generation of quark masses and a distinction between these two bases.

One of the primary characteristics of the CKM matrix is its unitarity ($(V_{CKM}^{\dagger}V_{CKM})_{ij} = (V_{CKM}V_{CKM}^{\dagger})_{ij} \equiv \delta_{ij}$). Deviations from unitarity could signal physics beyond the Standard Model, such as the presence of a fourth generation, though this would conflict with other observations that clearly indicate the existence of only three generations [54].

$$V_{\text{CKM}}^{\dagger}V_{CKM} = \begin{pmatrix} V_{ud}^* & V_{cd}^* & V_{td}^* \\ V_{us}^* & V_{cs}^* & V_{ts}^* \\ V_{ub}^* & V_{cb}^* & V_{tb}^* \end{pmatrix} \begin{pmatrix} V_{ud} & V_{us} & V_{ub} \\ V_{cd} & V_{cs} & V_{cb} \\ V_{td} & V_{ts} & V_{tb} \end{pmatrix} \equiv \begin{pmatrix} 1 & 0 & 0 \\ 0 & 1 & 0 \\ 0 & 0 & 1 \end{pmatrix} \tag{1.13}$$

$$V_{CKM}V_{\text{CKM}}^{\dagger} = \begin{pmatrix} V_{ud} & V_{us} & V_{ub} \\ V_{cd} & V_{cs} & V_{cb} \\ V_{td} & V_{ts} & V_{tb} \end{pmatrix} \begin{pmatrix} V_{ud}^* & V_{cd}^* & V_{td}^* \\ V_{us}^* & V_{cs}^* & V_{ts}^* \\ V_{ub}^* & V_{cb}^* & V_{tb}^* \end{pmatrix} \equiv \begin{pmatrix} 1 & 0 & 0 \\ 0 & 1 & 0 \\ 0 & 0 & 1 \end{pmatrix} \tag{1.14}$$

While the interactions of quarks with the $W^{\pm}$ boson are influenced by their flavor, as governed by the CKM matrix, all charged leptons interact with the W boson in weak interactions uniformly, irrespective of their flavor. This is called Lepton Universality (LFU) and it is remarkable considering the significant mass differences among leptons.

This universality emerges naturally from the structure of the SM, particularly from the way leptons couple to the $W^{\pm}$ and Z^0 bosons. In essence, the coupling constants which govern the force of interaction between leptons and these bosons remain uniform for every lepton flavor. This is what leads to the prediction that weak processes should exhibit this universality across lepton flavors. Experimental tests of Lepton Flavor Universality (LFU) typically involve comparing rates of processes like decays or scatterings across different lepton flavors and looking for deviations from the expected ratios.

However, recent experimental results have hinted at possible violations of LFU. While these indications are not conclusive and remain under active investigation, a verified violation would point to Beyond the Standard Model (BSM) physics. Such a discovery would be groundbreaking, potentially pointing the way to a more complete theory that includes new particles or interactions. This makes the study and testing of LFU one of the forefront topics in modern particle physics research.

In the context of our semileptonic hyperon decay ($\Lambda \to p\mu^-\bar{\nu}_\mu$), the observable

$$R^{\mu e} = \frac{\Gamma(\Lambda \to p\mu^-\bar{\nu}_\mu)}{\Gamma(\Lambda \to pe^-\bar{\nu}_e)} \tag{1.15}$$

it is sensible to violations of LFU, since couplings of charged leptons to the gauge bosons are expected to be identical, with the only difference emerging from the lepton masses.

1.3 LEPTON FLAVOR UNIVERSALITY

Lepton flavor universality is one of the key features of the SM. Any observed deviation from LFU will imply the discovery of New Physics (NP) since, in the SM, the coupling constants which govern the force of interaction between leptons and the $W^{\pm}$ and Z^0 bosons remain uniform for every lepton flavor.

In recent years, several tests of LFU have been conducted at Large Hadron Collider beauty (LHCb) and the B factories. Some of the results have shown significant deviations from LFU expectations [52].

Currently, theoretical predictions for LFU tests generally possess lower uncertainties compared to experimental measurements. Consequently, numerous experimental enhancements are anticipated. These include enlarging data samples to diminish statistical uncertainties and undertaking various initiatives to reduce systematic uncertainties as well.

1.3.1 TWO-HIGGS-DOUBLET MODELS

In the framework of the Standard Model, the Higgs boson is the only particle that interacts with the various types of charged leptons in a distinctive way, having a unique coupling strength for each lepton flavor. Taking that into account, considering a SM extension including a second higgs doublet can be a natural solution to explain LFU deviations.

A unique aspect of the Two-Higgs-Doublet Model (2HDM) is the inclusion of a charged Higgs boson in its array of particles. This charged Higgs has the potential to violate LFU in decays involving semileptonic and leptonic hadrons, contributing at the same level than the Standard Model processes [25].

Nevertheless, numerous observed quantities place constraints on this model. Measurements such as the g-2 anomaly and vacuum stability [75] imply constraints and $b \to s\gamma$ transitions restricts the mass of the charged Higgs [61].

1.3.2 LEPTOQUARKS

Leptoquark models have been suggested as a potential explanation for the anomalies observed in LFU tests. These hypothetical particles are bosons that carry both strong and electroweak interaction charges, enabling direct transitions between quarks and leptons through leptoquark-mediated processes. Various leptoquark models have been put forward, especially to account for anomalies involving τ leptons; in these models, there exists a flavor symmetry that implies dominant couplings to third-generation fermions [43].

Observational evidence places several constraints on leptoquark models. These include the absence of signals in various flavor-changing processes [9], the impact on electroweak precision measurements, details observed in τ decays [46], and the outcomes of searches for high-transverse-momentum events [51].

1.4 SEMILEPTONIC HYPERON DECAY FEATURES

Quantum Chromodynamics (QCD), the theory describing the strong interactions within the SM, exhibits an SU(3) flavor symmetry. This symmetry is related to the exchangeability of quark flavors and is exact in the realm of QCD. When we consider the quarks confined within hadrons, this flavor symmetry would allow the

interchange of different quark flavors without altering the strong interactions (SU(3)-flavor symmetry). However, this symmetry is not exact due to the varying masses of the quarks.

Examining the quark mass spectrum reveals a distinct separation: the up, down, and strange quarks are significantly lighter than their heavier counterparts. At energy scales where the strong interaction is the predominant interaction, the differences in masses among the u, d, and s quarks are sufficiently small that they can be considered nearly interchangeable in terms of QCD dynamics. This leads to an approximate SU(3)-flavor symmetry, particularly relevant for hyperons — those baryons that include one or more strange quarks but no charm, bottom, or top quarks.

Semileptonic Hyperon Decays (SHD) exhibit several distinct characteristics when compared to the β decay processes (notice that in the regular β decay we observe a $d \rightarrow u$ transition and in the SHD we observe a $s \rightarrow u$ transition). The intrinsic spin $\frac{1}{2}$ nature of hyperons endows the hadronic component of their semileptonic decay matrix elements with a greater depth of insight into the strong interactions, surpassing that offered by the matrix elements of spin-zero meson leptonic and semileptonic decays. Owing to the mass variances among hyperons, a broader set of form factors must be considered relative to those in nuclear or neutron β decays. Furthermore, hyperons are marked by their strangeness—a property absent in nucleons—and often possess isospin configurations distinct from nucleons. Additionally, many SHD can produce a $\mu\bar{\nu}_\mu$ pair, an option not often available in meson and nucleon β decays. These attributes underscore the enhanced richness of SHD as a field of study [50].

1.4.1 LFU IN SHD

In the SM, the lagrangian responsible for the $s \rightarrow u$ quark transition during the semileptonic decay of a baryon to another baryon, a lepton (l), and an antineutrino ($\bar{\nu}_l$), originates from the weak interaction lagrangian term. This particular term pertains to the charged current interactions mediated by the $W^\pm$ bosons [65]:

$$\mathcal{L}_{cc} = -\frac{g}{\sqrt{2}}\left(\bar{u}_L\ \gamma_\mu V_{us}\ s_L\right) W^+_\mu + h.c. \tag{1.16}$$

For energies much less than the electroweak symmetry breaking scale, given by $v = (\sqrt{2}G_F)^{1/2} \approx 246$ GeV, all processes with charged weak currents that include up and strange quarks are captured by a Fermi (V - A) × (V - A) four-particle interaction [26]. The effective lagrangian for a SHD, without considering BSM contributions, is:

$$\mathcal{L} = -\frac{G_F V_{us}}{\sqrt{2}} \sum_{l=e,\mu} [\bar{l}\gamma_\mu(1-\gamma_5)\nu_l].[\bar{u}\gamma_\mu(1-\gamma_5)s] + h.c. \tag{1.17}$$

where γ_5= - $\begin{pmatrix} 0 & 1 \\ 1 & 0 \end{pmatrix}$ and G_F is the Fermi coupling constant, related with the weak coupling constant g and the $W^\pm$ boson mass (M_W) by

$$\frac{G_F}{(\hbar c)^3} = \frac{\sqrt{2}g^2}{8M_W^2 c^4}$$

Since this is not a simply $s \rightarrow u$ quark transition, we have to consider the quarks being confined inside the baryon environment. Disregarding electromagnetic corrections, the amplitude for a generic semileptonic hyperon decay ($B_1(p_1) \rightarrow B_2(p_2) l^-(p_l) \bar{\nu}_l(p_\nu)$) can be separated into distinct leptonic and baryonic matrix elements. The hadronic currents are parameterizable via form factors, being the axial current [22] [26]:

$$\langle B_2(p_2)|\bar{u}\gamma_\mu s|B_1(p_1)\rangle = \bar{u}_2(p_2)\Big[f_1(q^2)\gamma_\mu + \frac{f_2(q^2)}{M_1}\sigma_{\mu\nu}q^\nu + \frac{f_3(q^2)}{M_1}q_\mu\Big]u_1(p_1) \quad (1.18)$$

and the vector hadronic current:

$$\langle B_2(p_2)|\bar{u}\gamma_\mu\gamma_5 s|B_1(p_1)\rangle = \bar{u}_2(p_2)\Big[g_1(q^2)\gamma_\mu + \frac{g_2(q^2)}{M_1}\sigma_{\mu\nu}q^\nu + \frac{g_3(q^2)}{M_1}q_\mu\Big]\gamma_5 u_1(p_1) \quad (1.19)$$

where $u_{1,2}$ and $M_{1,2}$ are the $B_{1,2}$ spinor amplitudes and masses respectively, q is the momentum transfer to the dilepton pair ($q = p_1 - p_2$) and $\sigma_{\mu\nu} = [\gamma_\mu, \gamma_\nu]/2.$.

The approximate SU(3)-flavor symmetry present in the hyperons regulates the decay's phase space and permits a systematic expansion of observables based on the generic parameter that governs symmetry breaking [26] [50]

$$\delta = \frac{M_1 - M_2}{M_1}$$

Expanded in δ up to next-to-leading order (NLO) and disregarding m_e (since m_e is much smaller than the other mass scales in the process, such as the mass difference Δ), the integrated ($B_1 \rightarrow B_2 e^- \bar{\nu}_e$) decay rate assuming real form factors and going to order δ^2 is given by [22]:

$$\Gamma^{\mathrm{SM}}(B_1 \rightarrow B_2 e^- \bar{\nu}_e) \simeq \frac{G_F^2 |V_{us}\, f_1(0)|^2 \Delta^5}{60\pi^3}\Big[\big(1-\frac{3}{2}\delta\big) + 3\big(1-\frac{3}{2}\delta\big)\frac{g_1(0)^2}{f_1(0)^2} - 4\delta\frac{g_2(0)}{f_1(0)}\frac{g_1(0)}{f_1(0)}\Big] \quad (1.20)$$

This formula demonstrates a very small dependence on the form factors; it does not need the behavior with respect to q^2, and additionally, the last term may be disregarded as the weak-electric charge, $g_2(0)$, is on the order of $O(\delta)$ [26]. Therefore, within a theoretical precision of $O(\delta^2)$, estimated to be between 1 to 5 %, the overall decay rate for the electron mode in the SM depends only on the mother axial and vector charges, $g_1(0)$ and $f_1(0)$ [26].

The BSM physics can generate additional contributions to the vector and axial vector couplings of the standard model, with coupling constants ϵ_L and ϵ_R, as well as chirality-flipping currents scalar, pseudo-scalar, and tensor, with couplings ϵ_S, ϵ_P,

and ϵ_T, respectively) [31]. So, considering BSM physics, the most general effective field theory would be expressed by the following lagrangian [26]:

$$\mathcal{L} = -\frac{G_F V_{us}}{\sqrt{2}}(1+\epsilon_L+\epsilon_R)\times\sum_{l=e,\mu}[\bar{l}\gamma_\mu(1-\gamma_5)\nu_l.\bar{u}[\gamma_\mu-(1-2\epsilon_R)\gamma_\mu\gamma_5]s + \bar{l}(1-\gamma_5)\nu_l.\bar{u}[\epsilon_S-\epsilon_P\gamma_5]s+\epsilon_T\bar{l}\sigma_{\mu\nu}(1-\gamma_5)s]+h.c. \tag{1.21}$$

This formulation of the lagrangian utilizes solely those SM fields pertinent at lower energy scales while ensuring that the operators are singlets with respect to both color and electromagnetism. Additionally, the focus has been narrowed to those non-standard interactions that uphold lepton flavor conservation and exhibit universality across leptons. In conclusion, this derivation operates under the presumption that the Wilson coefficients (WC), denoted by ϵ_i , are real numbers, given that our interest lies in observables that do not violate CP symmetry [26].

Typically known as the SM effective field theory (SMEFT), this structure permits an inductive approach to probing NP, exploring the implications of collider findings for low-energy experiments, and the other way around. This synergy will play a pivotal role in defining the nature of the NP should any deviations from the SM predictions emerge. Instances of how this approach is applied from a top-down perspective, where interconnected effects manifest at both high and low energies, are observable in situations involving leptoquarks [40] or additional scalar fields [71].

These non-standard scalar, pseudoscalar and tensor sources introduce additional form factors in the hadronic currents [26] [76]:

$$\langle B_2(p_2)|\bar{u}s|B_1(p_1)\rangle = f_S(q^2)\bar{u}_2(p_2)u_1(p_1) \tag{1.22}$$

$$\langle B_2(p_2)|\bar{u}\gamma_5 s|B_1(p_1)\rangle = g_P(q^2)\bar{u}_2(p_2)\gamma_5 u_1(p_1) \tag{1.23}$$

$$\langle B_2(p_2)|\bar{u}\sigma_{\mu\nu}s|B_1(p_1)\rangle \simeq f_T(q^2)\bar{u}_2(p_2)\sigma_{\mu\nu}u_1(p_1) \tag{1.24}$$

The LFU test observable defined as the ratio between muon and electron modes

$$R^{\mu e} = \frac{\Gamma(B_1\to B_2\mu^-\bar{\nu}_\mu)}{\Gamma(B_1\to B_2 e^-\bar{\nu}_e)} \tag{1.25}$$

is sensitive to non standard scalar and tensor contributions [26] . Moreover, in the SM, the dependency on the form factors is anticipated to simplify when considering the ratio. Indeed, by operating at Next-to-Leading Order (NLO), we achieve:

$$R^{\mu e}_{\rm SM} = \sqrt{1-\frac{m_\mu^2}{\Delta^2}}\left(1-\frac{9}{2}\frac{m_\mu^2}{\Delta^2}-4\frac{m_\mu^4}{\Delta^4}\right)+\frac{15}{2}\frac{m_\mu^4}{\Delta^4}\operatorname{arctanh}\left(\sqrt{1-\frac{m_\mu^2}{\Delta^2}}\right) \tag{1.26}$$

where $\Delta = M_2 - M_1$.

The LFU test observable defined in 1.25 is predicted by theory to be $R^{\mu e} = 0.153 \pm 0.008$ working at next-to-leading order [26]. This prediction is remarkable, since up

to this relative theoretical precision ($O(\frac{(M_1-M_2)^2}{M_1^2})$) the ratio does not depend on form factors.

A precise measurement of $R^{\mu e}$ implies a constraint on the Wilson coefficients, since the mentioned new physics scalar and tensor operators will contribute to the ratio in the following way [26]:

$$R^{\mu e}_{\rm NP} = \frac{\left(\epsilon_S \frac{f_S(0)}{f_1(0)} + 12\epsilon_T \frac{g_1(0)}{f_1(0)} \frac{f_T(0)}{f_1(0)}\right)}{(1-\frac{3}{2}\delta)\left(1+3\frac{g_1(0^2)}{f_1(0)^2}\right)} \Pi(\Delta, m_\mu) \tag{1.27}$$

where the phase-space integral $\Pi(\Delta, m_\mu)$ is

$$\Pi(\Delta, m_\mu) = \frac{5}{2}\frac{m_\mu}{\Delta}\left[(2+13\frac{m_\mu^2}{\Delta^2})\sqrt{1-\frac{m_\mu^2}{\Delta^2}} - 3\left(4\frac{m_\mu^2}{\Delta^2}+\frac{m_\mu^4}{\Delta^4}\right)\text{arctanh}(\sqrt{1-\frac{m_\mu^2}{\Delta^2}})\right] \tag{1.28}$$

It is useful to express the ratio of $R^{\mu e}_{\rm NP}$ and $R^{\mu e}_{\rm SM}$ encapsulating the scalar and tensor related dimensionless contributions in r_S and r_T in order to express the sensitivity to the Wilson coefficients [26]:

$$\frac{R^{\mu e}_{\rm NP}}{R^{\mu e}_{\rm SM}} = 1 + r_S\epsilon_S + r_T\epsilon_T \tag{1.29}$$

being the SHD sensitivity to the Wilson coefficients very channel-dependent [26].

Given that the SM-NLO predictions, $R^{\mu e}_{\rm SM}$, for the various SHD modes are precise, these decays are excellent candidates for performing tests of LFU.

Combining Eq. 1.26 and Eq. 1.20 we arrive to the SM prediction for the muon mode branching ratio.

$$\Gamma^{\rm SM}(B_1 \to B_2\mu^-\bar{\nu}_\mu) \simeq \frac{G_F^2|V_{us}\, f_1(0)|^2\Delta^5}{60\pi^3}\left[\left(1-\frac{3}{2}\delta\right)+3\left(1-\frac{3}{2}\delta\right)\frac{g_1(0)^2}{f_1(0)^2} - 4\delta\frac{g_2(0)}{f_1(0)}\frac{g_1(0)}{f_1(0)}\right] \left(\sqrt{1-\frac{m_\mu^2}{\Delta^2}}\left(1-\frac{9}{2}\frac{m_\mu^2}{\Delta^2}-4\frac{m_\mu^4}{\Delta^4}\right)+\frac{15}{2}\frac{m_\mu^4}{\Delta^4}\text{arctanh}\left(\sqrt{1-\frac{m_\mu^2}{\Delta^2}}\right)\right) \tag{1.30}$$

1.4.2 V_{us} FROM $\mathcal{B}(\Lambda \to p\mu^-\bar{\nu}_\mu)$

Condensing the $R^{\mu e}$ term in Eq. 1.30 and considering no BSM contributions, we can write V_{us} in terms of the form factors predicted by theory and the decay rates ratio.

$$|V_{us}|^2 \simeq \frac{\Gamma^{\rm SM}(B_1 \to B_2\mu^-\bar{\nu}_\mu)\; 60\pi^3}{R^{\mu e}G_F^2\, f_1(0)^2\Delta^5\left[\left(1-\frac{3}{2}\delta\right)+3\left(1-\frac{3}{2}\delta\right)\frac{g_1(0)^2}{f_1(0)^2}\right]} \tag{1.31}$$

where the - $4\delta\frac{g_2(0)}{f_1(0)}\frac{g_1(0)}{f_1(0)}$ term is not being considered, since it is $O(\delta)$.

For the $\Lambda \to p\mu^-\bar{\nu}_\mu$ case, using the current PDG measurements and theoretical computation, the values for the parameters involved in this expressions are $\Delta^{\text{exp}} = 177.4110 \pm 0.0060$, $\delta^{\text{exp}} = 0.1590160 \pm 0.0000050$, $f_1(0) = -\sqrt{\frac{3}{2}}$, $\frac{g_1(0)}{f_1(0)} = 0.718 \pm 0.015$, $R^{\mu e} = 0.153 \pm 0.008$ [26] and $\frac{G_F}{(\hbar c)^3} = 1.1663787(6) \times 10^{-5} GeV^{-2}$ [78].

Considering that we aim to measure $\mathcal{B}(\Lambda \to p\mu^-\bar{\nu}_\mu)$, we should rewrite the decay rate

$$\Gamma(\Lambda \to p\mu^-\bar{\nu}_\mu) = \Gamma(\Lambda)\ \mathcal{B}(\Lambda \to p\mu^-\bar{\nu}_\mu) \tag{1.32}$$

where the $\Gamma(\Lambda)$ can be obtained from the particle life-time ($\tau(\Lambda) = (2.632 \pm 0.020) \times 10^{-10}$ [78]) using

$$\Gamma(\Lambda) = \frac{\hbar}{\tau(\Lambda)} = (2.501 \pm 0.019) \times 10^{-15} [GeV] \tag{1.33}$$

Including the values in GeV units in Eq. 1.31, we obtain:

$$|V_{us}|^2 \simeq \frac{\mathcal{B}^{\text{SM}}(B_1 \to B_2\mu^-\bar{\nu}_\mu)\ (4.652 \pm 0.035) \times 10^{-12}}{(1.06 \times 0.06) \times 10^{-14}} = \mathcal{B}^{\text{SM}}(B_1 \to B_2\mu^-\bar{\nu}_\mu) \cdot (437 \pm 26) \tag{1.34}$$

Using the current $\mathcal{B}(\Lambda \to p\mu^-\bar{\nu}_\mu)$ PDG value [78] we obtain $V_{us} \simeq 0.257 \pm 0.018$, with a large uncertainty compared to our current knowledge on this CKM matrix element, $V_{us} = 0.22500 \pm 0.00067$. On top of this, this V_{us} prediction was done within a theoretical precision of $O(\delta^2)$, estimated to be between 1 to 5 %.

Even having a large uncertainty using the current available values for the $\mathcal{B}(\Lambda \to p\mu^-\bar{\nu}_\mu)$ and the theoretical prediction, this uncertainty can be reduced performing a precise measurement of the $\mathcal{B}(\Lambda \to p\mu^-\bar{\nu}_\mu)$ in LHCb, as we plan to do in this thesis. Moreover, as it is explained in detail in the next section, the two most precise V_{us} measurements exhibit a 3σ discrepancy. In this context, precise SHD V_{us} measurements are required to put light in this puzzle.

Despite the considerable uncertainty in the current values of the branching ratio ($\mathcal{B}(\Lambda \to p\mu^-\bar{\nu}_\mu)$) and the theoretical prediction, this uncertainty can be mitigated with theoretical efforts and by conducting a precise measurement of the $\mathcal{B}(\Lambda \to p\mu^-\bar{\nu}_\mu)$ at LHCb, which is a key objective of this thesis. Furthermore, as detailed in the following section, the two most precise measurements of V_{us} currently show a 3σ discrepancy. In this context, accurate measurements of V_{us} from SHD are essential to shed light on this puzzle

1.5 MOTIVATION OF THIS MEASUREMENT

In the last decades the focus was in the higher mass sector of the CKM matrix. However it is the low mass sector, V_{ud} and V_{us}, where is it possible to obtain the highest precision and the most sensitive test of the unitary of the CKM matrix.

One of the strongest tests of the unitarity of the CKM matrix can be achieved by accurately measuring $|V_{us}|$. This is because eq. 1.14, implies that:

$$|V_{ud}|^2 + |V_{us}|^2 + |V_{ub}|^2 \equiv 1 \tag{1.35}$$

Given that the contribution from $|V_{ub}|^2$ element is almost entirely negligible (approximately 1.3×10^{-5} [78]), this relation is reduced to the Cabibbo universality ($|V_{ud}| \approx cos\ \theta_{12}$, $|V_{us}| \approx sin\ \theta_{12}$).

Since $|V_{ud}|$ has already been measured with great precision, with a value of $|V_{ud}| = 0.97436 \pm 0.00016$ [78], the focus shifts to V_{us}.

In fact, using our current best measurements of V_{ud}, V_{us} and V_{ub} we obtain

$$|V_{ud}|^2 + |V_{us}|^2 + |V_{ub}|^2 = 0.9985 \pm 0.0007 \tag{1.36}$$

showing a 2.2σ tension with the expected unitarity in the first CKM row. Currently, enhanced precision in theoretical uncertainties when estimating $|V_{ud}|$ and $|V_{us}|$ is uncovering potential anomalies. These anomalies might indicate the presence of NP phenomena at the TeV scale [47].

Moreover, the measurements of V_{us} in leptonic ($K_{\mu 2}$) and semileptonic (K_{l3}) kaon decays exhibit a 3σ discrepancy. Such a disagreement can hint towards two potential scenarios: the existence of physics beyond the Standard Model or a significant, yet unidentified, systematic effect within the Standard Model itself [72].

Given this context, it becomes paramount to explore other avenues to measure V_{us} with high precision. In this regard, semileptonic hyperon decays emerge as a promising alternative. If these decays yield values of V_{us} consistent with one set of kaon decays and not the other, it could potentially pinpoint the origin of the aforementioned discrepancy. On the other hand, if the value from hyperon decays stands in contrast to both kaon measurements, it would further complicate our understanding and suggest deeper underlying issues.

Thus, intensifying the focus on measuring V_{us} from semileptonic hyperon decays could be instrumental in shedding light on this puzzle. Whether it ends up reinforcing the Standard Model, identifying systematic flaws, or pointing towards new physics, the endeavor will undoubtedly provide valuable insights into the realm of particle physics.

It is also natural to investigate if contributions in charged-current quark decays breaking LFU can be found in s $\rightarrow$ u since this can open a door to physics BSM. Especially taking into account the results coming from b $\rightarrow$ c transitions that point in this direction [30].

From a theoretical perspective, hyperon semileptonic decays have been identified as potentially sensible to BSM mechanisms that break lepton universality. These decays are governed by a minor SU(3) flavor symmetry breaking parameter, enabling systematic expansions and precise forecasts with minimal reliance on hadronic form factors. The muonic decay channels are particularly receptive to non-standard scalar and tensor contributions, potentially offering a significant complementary approach to direct new physics searches at the LHC [26].

In the $\Lambda \rightarrow p l^- \bar{\nu}_l$ case, the LFU test observable defined in 1.15 is predicted by theory to be $R^{\mu e} = 0.153 \pm 0.008$ working at next-to-leading order [26]. Current best measurent of this observable was performed by BESIII in 2021, obtaining $R^{\mu e} = 0.178 \pm 0.028$, consistent within uncertainties with the predicted value [6].

However, since the decay mode involving the electron is measured with greater precision, $\mathcal{B}(\Lambda \rightarrow pe^{-}\bar{\nu}_{e}) = (8.34 \pm 0.14) \times 10^{-4}$ [78], most of the uncertainty arises from the BESIII measurement of the muonic mode, given by $\mathcal{B}(\Lambda \rightarrow p\mu^{-}\bar{\nu}_{\mu}) = [1.48 \pm 0.21, (\text{stat}) \pm 0.08, (\text{syst})] \times 10^{-4}$.

Increasing the precision in the $\mathcal{B}(\Lambda \rightarrow p\mu^{-}\bar{\nu}_{\mu})$ is essential to test lepton universality in $s \rightarrow u$ transitions.

CHAPTER 2

EXPERIMENTAL CONDITIONS

2.1 THE LHC

The Large Hadron Collider (LHC) is the most powerful and the largest particle accelerator of the world. It began operations on September 10, 2008. It is the most recent expansion to CERN's complex of accelerators. This accelerator features a 27-kilometre ring equipped with superconducting magnets, along with several accelerating structures designed to incrementally increase the energy of the particles as they travel through the ring [45].

Within the accelerator, two beams of high-energy particles are accelerated to nearly the speed of light and are then directed to collide with each other. These beams move in opposite directions, each contained within its own beam pipe – a pair of tubes maintained under ultra-high vacuum conditions. A powerful magnetic field, generated by superconducting electromagnets, maintain the beams around the ring of the accelerator.

The particle beams within the LHC are made to collide at four specific points along the accelerator's ring. These collision points align with the locations of four major particle detectors: A ToroidaL AparatuS (ATLAS), Compact Muon Solenoid (CMS), A Large Ion Collider Experiment (ALICE), and LHCb.

2.2 THE LHCb DETECTOR

LHCb is one of the four big detectors collecting data in the LHC, at CERN. The name comes from its purpose of detecting the decay of particles that contain b quarks. These particles, formed in pp collisions, and the particles in which they decay, do not move away too much from the direction of incidence of the beam. This is reflected in the forward design of the detector [58] which, unlike other LHC detectors which

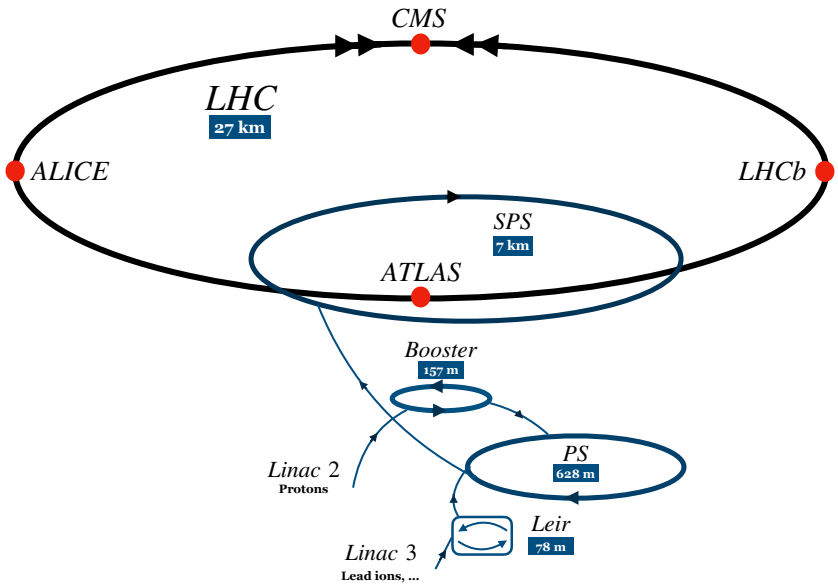

FIGURE 2.1: Display of the CERN accelerator complex, including the LHC and its four experiments.

cover the entire solid angle around the collision of the protons, presents its multiple subdetectors arranged in the forward direction

The LHCb, one of the four major detectors at the LHC located at CERN, is specifically designed for the detection of decays involving b quarks. Originating from pp collisions, these particles and their decay products tend to travel close to the incident beam's direction. This characteristic is the basis for the forward design of the LHCb detector, as detailed in [58]. Unlike other detectors at the LHC, which cover the entire solid angle around the proton collisions, the LHCb has its subdetectors on the forward direction [37] with an acceptance of $1.6 \leq \eta \leq 4.9$, where η is the pseudorapidity

$$\eta = \frac{1}{2} \ln \frac{p + p_z}{p - p_z} = -\ln \tan \frac{\theta}{2} \tag{2.1}$$

In this expression p is the magnitude of the particle momentum, p_z the magnitude in the direction of the colliding protons and θ is the angle between the particle's path and the trajectory of the colliding protons. This acceptance is equivalent to an angular acceptance of 10 mrad $\leq \theta \leq$ 300 mrad.

The LHCb detector was specifically designed for the accurate measurement of CP symmetry violation and the rare decay of mesons, particularly those comprising b quarks or their antiparticles ($\overline{b}$). Its unique design is tailored to efficiently study these specific processes. This optimization has facilitated significant discoveries, including the determination of the branching ratio for the rare decay of the B_s meson into a muon-antimuon pair, as well as the measurement of the CP violation phase in the

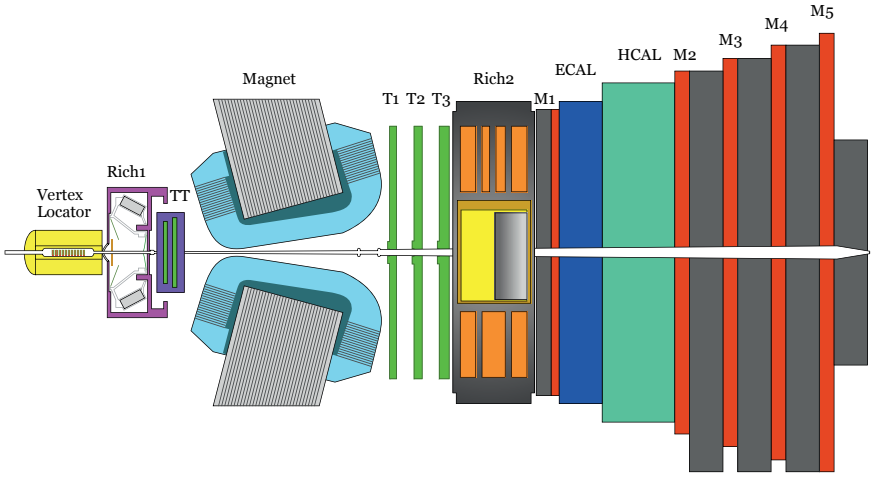

FIGURE 2.2: The LHCb detector according to the plane of curvature of the trajectory of the charged particles.

decay of $B_s \rightarrow J/\Psi\ \phi$. Examples of the key physics measurements by LHCb can be found in [7].

The LHCb experiment is designed to operate at a reduced instantaneous luminosity of $2 - 5 \cdot 10^{32}\ cm^{-2} \cdot s^{-1}$, which is lower than the nominal LHC luminosity of $10^{34}\ cm^{-2} \cdot s^{-1}$. This is achieved by employing larger β^* (which denote the amplitude modulation of the beam at the interaction point and are directly related to the beam size) compared to other LHC detectors, resulting in less focused beams.

The idea behind this approach is to simplify the task of accurately pinpointing the location of the initial proton-proton collision Primary Vertex (PV) and the subsequent decay points of other short-lived particles Secondary Vertex (SV). Accurately identifying these vertices is crucial for the physics objectives of the LHCb experiment.

The LHCb experiment adopts a coordinate system consistently utilized throughout this thesis. The origin is designated at the pp interaction point, extending the z axis along the beam direction towards the remainder of the detector apparatus. Oriented vertically upwards, influenced by gravity, the y axis is established, while the x axis maintains the system's "right-handedness" ($\hat{x} \times \hat{y} = \hat{z}$), positioned horizontally, facing the detector's left when observed from the negative z side. A prevalent metric, "transverse momentum" (p_T), referencing a particle, is defined within this particular coordinate framework as

$$p_T = \sqrt{p_x^2 + p_y^2} \tag{2.2}$$

The first period of data taking, Run I, took place from 2009 to 2012. Run II refers to the second data-taking run of the LHCb experiment, that took place from 2015 to 2018. In Run II, the LHC operated at a higher energy, with proton-proton collision energies reaching 13 TeV and a luminosity of almost 6 fb^{-1} was recorded.

TABLE 2.1: Energy in the center of mass (s) and integrated luminosity recorded for each year of data taking during Run1 and Run2.

Year	Energy (TeV)	Integrated Luminosity (fb^{-1})
2010	7	0.04
2011	7	1.11
2012	8	2.08
2015	13	0.33
2016	13	1.67
2017	13	1.71
2018	13	2.19

This analysis uses Run II LHCb data. As a consequence, the detector described is the one that took data from 2015 to 2018 and not the upgraded one that is taking data currently [48].

2.2.1 TECHNICAL SPECIFICATIONS.

LHCb features a single-arm spectrometer design, providing forward angular coverage ranging from roughly 10 mrad to 300 mrad in the bending plane and up to 250 mrad in the non-bending plane. This specific geometry is chosen because, at high energies, both b and $\bar{b}$ hadrons are predominantly produced within the same forward or backward directional cone.

The basic characteristics of LHCb are:

Dimensions: 21 meters long, 13 meters wide and 10 meters high.

Weight: 5 600 tons.

2.3 SUBDETECTORS

We essentially have a Vertex Locator (**VELO**) (to determine the trajectory of the particles near the point of interaction, with the main objective of separating the primary vertices where, for example, the B-mesons are produced and the secondary ones, where they decay), **RICH** (to identify the particles producing each track by obtaining their mass and charge), **T-stations** (give the trajectories and momentum of charged particles), **ECAL** (detect electrons and photons), **HCAL** (detect hadrons), **Muon Chambers** (detect muons).

2.3.1 MAGNET:

The LHCb dipole magnet [59] provides a magnetic field of 4 T.m that curve the charged particles in the horizontal plane of the detector with the idea of allowing the

measurement of their momenta. The measurement covers the forward acceptance of ± 250 mrad vertically and of ± 300 mrad horizontally.
To account for potential systematic effects, the orientation of the magnetic field is alternated periodically between upward and downward directions.
The magnetic field provided by the dipole must be known with excellent precision, in order to yield a momentum resolution as good as possible. The precision of the measurement obtained for the field mapping in the tracking volume is about $4 \cdot 10^{-4}$.
The trajectory of beams circulating within the LHC is influenced by the existence of the LHCb dipole magnet. To mitigate this impact, three compensatory magnets are strategically positioned around the detector [45].

2.3.2 VERTEX LOCATOR:

The Vertex Locator (VELO) [[37],[36],[35]] is the subdetector placed closer to the proton interaction point (primary vertex). It is designed to locate the primary and secondary vertices, focusing in b and c-hadrons decays.
The VELO also provides an excellent time resolution to measure the lifetimes of this particles, something crucial to investigate CP violation effects.
The Run 2 VELO contains two halves with 21 stations each, positioned along and perpendicular to the beam axis. Two types of silicon sensors are used: one measures the r coordinate with circular strips centered around the beam axis, the other measures the ϕ coordinate with straight, almost radial strips (including a stereo-angle built in).
The VELO is retractable, which allows to increase the separation between the two halves during injection and to adjust it (± 5mm) to the position of the beam.
The sensors are housed in a vacuum, isolated from the LHC vacuum by a slender, corrugated aluminum sheet. The design geometry enables the two halves of the VELO to overlap when completely closed, reducing the material a charged particle traverses from the interaction point to the sensors.
The uncertainty in the primary vertex's position primarily depends on the number of tracks generated during a proton-proton collision. On average, the resolution is 42 μm in the z-direction and 10 μm in the direction perpendicular to the beam. The resolution of the impact parameter is 20 μm, excluding the influence of the primary vertex, for tracks exhibiting the maximum transverse momentum. The accuracy of the decay length measurement varies between 220 μm and 370 μm, contingent on the specific decay channel. For the $B_s^0 \rightarrow D_s^- \pi^+$ decay channel, a lifetime resolution of 40 fs has been attained, enabling a 5σ measuring of Δm_s up to 54 ps^{-1} after a year of data collection [36].

2.3.3 TRACKING SYSTEM:

In LHCb tracks are reconstructed forming particle trajectories from the hits that the tracking system collects. Appart from the VELO, the LHCb tracking system is composed by the Tracker Turicensis (TT) [35], a single station right upstream the magnet, and by three tracking stations downstream the magnet and before RICH2.
The tracking stations have two different substructures: the inner tracker (IT) [14]

in the most inner part and the OT (outer tracker) [16] surrounding it. Since the technology of the TT and the three IT modules is the same (silicon microstrips), both are typically grouped in what is called the Silicon Tracker (ST).

The ST modules exhibit a spatial resolution of approximately 50 μm. Additionally, the hit efficiency has been observed to exceed 99.7% for the TT and 99.8% for the IT [58].

The Outer Tracker (OT) is structured into three stations, each being assembled from arrays of straw-tube modules. Every module comprises two offset layers, each containing 64 tubes with an internal diameter of 5 mm. The tubes are filled with a gas mixture consisting of 70% Argon and 30% CO_2, a choice made to guarantee a drift time that is less than 50 ns. It provides a single hit resolution of 205 μm [16] and it is positioned downstream of the magnet, co-located with the IT, serving as a drift-time detector. The IT is situated closer to the beam pipe, focusing on the regions with the highest particle density due to its proximity, while the OT extends coverage to the remaining areas within the LHCb acceptance. This strategic placement is influenced by the concentration of particles produced at lower angles, which allows for more flexible requirements concerning resolution, occupancy, and resistance to radiation in the outer regions. Both the OT and IT stations are commonly considered components of unified stations, referred to as T-stations and denoted as T1, T2, and T3.

In LHCb we define different types of tracks depending on the starting point and the end point of the track. Following this criterion, we can separate the tracks of the particles in LHCb in the following categories (see Fig. 2.3):

- VELO tracks: Those wich only pass through the VELO and follow its trajectory out of the LHCb acceptance.

- Upstream Tracks: Those tracks with hits on the VELO and on the TT (Tracker Turicensis), but without any hit on the T-stations.

- Downstream Tracks: Those tracks with hits on the TT (Tracker Turicensis) and on the T-stations (if the particle associated to this track is a muon, also in the Muon Chambers), but without any hit on the VELO. This track type is associated with particles with a long lifetime, decaying after the VELO.

- Long Tracks: Those tracks with hits on all the sub-detectors (the VELO and the following trackers), associated to particles that go through the entire detector.

- T Tracks: Those tracks with present hits only on the T-stations and on the following sub-detectors.

2.3.4 RICH:

The particle identification is based on the Cherenkov radiation of the particles. When a charged particle travels through a specific medium at a speed faster than light, it results in the emission of a light cone. The radius of this light cone is influenced

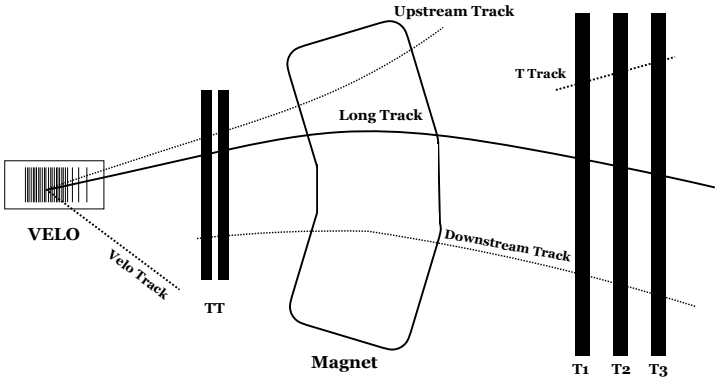

FIGURE 2.3: Different LHCb track types.

by the particle's speed. By analyzing this in conjunction with the particle's momentum, the particle's mass, and consequently its identity, can be ascertained. For the LHCb experiment's physics program, accurately identifying hadrons across a broad momentum spectrum is essential.

LHCb includes two Ring Imaging Cherenkov detectors [12], aiming at different momentum ranges. Both RICH detectors utilize mirrors to redirect the radiation towards a series of hybrid photon detectors (HPDs). These HPDs measure the positions where the Cherenkov photons are emitted.

The upstream detector covering the full LHCb acceptance, RICH1, covers the low momentum charged particle range 1- 60 GeV/c using aerogel and C_4F_{10} radiators, while the downstream detector, RICH2, covers the high momentum range from 15 GeV/c up to and beyond 100 GeV/c using a CF_4 radiator. This second RICH2 detector has an acceptance limited to the low-angle region, aiming to detect high-momentum particles.

The likelihood of accurately identifying each charged hadron consistently remains above 90% for a misidentification probability of 5% [24].

2.3.5 CALORIMETER SYSTEM:

The LHCb calorimeter system [11] has the function of selecting transverse energy hadron, electron and photon candidates for the first trigger level (L0) and providing the identification of electrons, photons and hadrons as well as the measurement of their energies and positions.

The calorimeter system is composed by a Preshower detector (PS) and a Scintillator Pad Detector (SPD) plane before the PS, and an Electromagnetic Calorimeter (ECAL) to which it follows a Hadron Calorimeter (HCAL). The purpose of having these four substructures is properly discriminating between hadrons, electrons/positrons and photons, since the energy deposition in each of the calorimeter components will depend on the nature of the particles.

The PS and SPS subdetectors are strategically positioned in front of the ECAL. Initially, the PS differentiates between charged particles and neutrals. After it, a singular 15 mm thick lead sheet is situated between the PS and the SPD. This configuration prompts electrons and photons to initiate showers, while the heavier hadrons, due to their extended interaction lengths, are more inclined to proceed through. Following this, the SPD identifies the electromagnetic showers. Utilizing this system in conjunction with the data from the ECAL facilitates the rapid identification of electrons for the triggering system.

The ECAL and HCAL are placed between the muon stations M1 and M2, as can be seen in Fig. 2.2. The ECAL covers the full LHCb acceptance and is placed at z = 12.5 m. Only angles where the radiation level is too high, those below 25 mrad, are not covered. Its energy resolution during Run 1 and 2 was measured [5] to be

$$\frac{\sigma_E}{E} = \frac{(9.0 \pm 0.5)\%}{\sqrt{E_{\text{GeV}}}} \oplus (0.8 \pm 0.2)\% \oplus \frac{0.003}{E_{\text{GeV}} \sin\theta}$$

where E is the particle energy in GeV and θ is the angle between the beam and a line from the LHCb proton-proton interaction point and the centre of the respective ECAL cell.

Finally, The HCAL has a thickness equivalent to 5.6 interaction lengths, constrained by spatial limitations. A sampling configuration, composed of iron and scintillating tiles, was selected, serving as the absorber and active material, respectively. Its energy resolution during Run 1 and 2 was measured [5] to be

$$\frac{\sigma_E}{E} = \frac{(67 \pm 5)}{\sqrt{E_{\text{GeV}}}}\% \oplus (9 \pm 2)\%$$

In the whole calorimeter system, the scintillation light is transmitted to Photo Multipliers (PMTs), that turn this light into an electric signal.

2.3.6 MUON STATIONS:

In the LHCb experiment, the muon system, as detailed in [15], features five tracking stations arranged along the beam axis. Station M1 is positioned before the preshower of the calorimeter. The subsequent four stations—M2, M3, M4, and M5—are situated beyond the calorimeter, interspersed with three iron filters[69].

The muon stations are equipped with Multi Wire Proportional Chambers [15] (MWPCs) operating with an Ar:CO_2:CF_4 (40% : 55% : 5 % in volume) gas mixture.

It is important to mention that when a charged particle (normally a muon) passes through the muon chamber it produces a hit (x, y and z position and error in x and y coordinates).

The process of muon identification begins by associating the hits in the muon chambers to each track. This is achieved by linear extrapolation of the incoming tracks to the muon stations. Based on factors like the track's momentum, the specific muon station, and the region, a Field of Interest (FoI) is defined around the extrapolated point. Within these FoIs at different muon stations, hits are sought, taking into account the

track's momentum. The closest hits are then selected. Only those tracks with valid hits in the muon chambers are further processed by the subsequent algorithms. From this procedure, a boolean variable known as 'IsMuon' in LHCb terminology is derived. This variable serves as the most fundamental form of muon identification.

2.4 TRIGGER.

In the field of particle physics, a trigger refers to a mechanism that rapidly selects specific events in a particle detector for retention, as only a limited number of events can be recorded due to practical constraints. This necessity arises from the limitations in computational power, data storage capabilities, and data transfer rates. Given that particle physics experiments often aim to detect "interesting" events (like the decay of rare particles), which happen infrequently, triggers are employed to pinpoint and record events for subsequent analysis.

2.4.1 LHCb TRIGGER

The existing system for online event selection (trigger) is composed of two stages. The initial stage, known as Level 0 (L0), filters events based on substantial energy deposits and the presence of high-momentum muon tracks, utilizing data exclusively from the calorimeters and muon system. This stage, executed through hardware, reduces the event rate from a maximum of 30 MHz during collisions to roughly 900 kHz. The L0 trigger decision is made within a total latency of 4 microseconds. For events that pass this level, the complete detector data is collected and forwarded to the High-Level Trigger (HLT) system, which operates on a software basis within a CPU farm. Here, events undergo full reconstruction, and those that exhibit characteristics of both inclusive and exclusive signals are earmarked for offline examination. The HLT ultimately produces an output event rate of around 4.5 kHz [44].

Following the HLT, events are stored for subsequent processing, which involves more precise alignment and calibration of the sub-detectors, as well as the utilization of advanced reconstruction software. This phase, encompassing both the detailed reconstruction and the targeted selection of noteworthy events, is known as the offline reconstruction and selection process.

2.4.2 LEVEL-0 HARDWARE TRIGGER.

The L0 trigger of the LHCb experiment is divided into three distinct segments: the L0-Calorimeter trigger, the L0-Muon trigger, and the L0-PileUp trigger, which is specifically used for luminosity measurements.

The L0-Calorimeter system manage data from the SPD, Pre-Shower (PS), ECAL, and HCAL detectors. It calculates the transverse energy (E_T) generated by particles in clusters of 2x2 cells and creates three types of candidates. The L0Hadron candidate is the highest E_T cluster in the HCAL, inclusive of the energy from the corresponding ECAL cluster. The LoPhoton candidate is identified as the highest E_T cluster in the ECAL. The LoElectron, similar to LoPhoton, additionally requires at least one hit

in an SPD cell located in front of the PS cells. Candidates that exceed a certain E_T threshold activate the L0 trigger.

In the muon detection process, the L0 muon processors search for the two highest p_T muon tracks in each quadrant, determining their p_T based on their positions in the first two stations.

The total output rate of the L0 trigger is limited to 1MHz, matching the maximum readout rate of the LHCb detector. This output rate is comprised of approximately 400 kHz from muon triggers, 500 kHz from hadron triggers, and 150 kHz from electron and photon triggers.

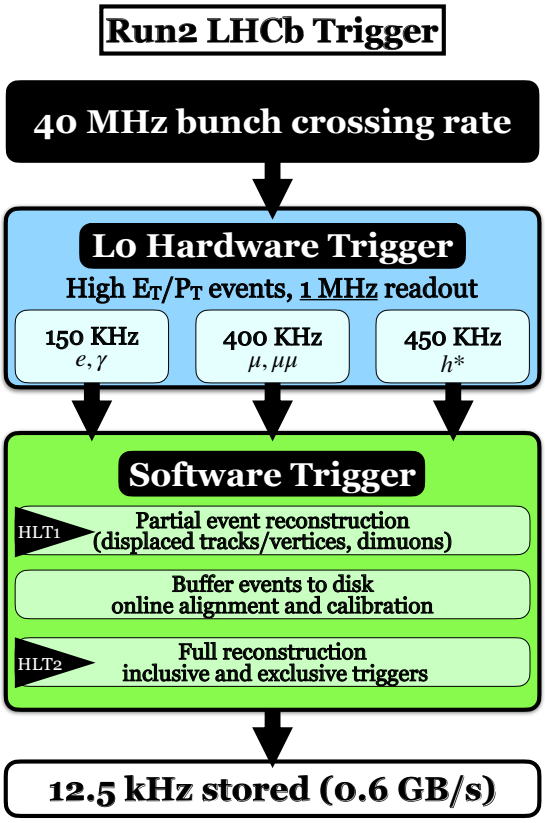

FIGURE 2.4: LHCb trigger strategy.

2.4.3 HIGH LEVEL TRIGGER.

Events that pass the L0 stage are forwarded through the data acquisition network to a processor in the Event Filter Farm (EFF). Within the EFF, the HLT operates as a software-based application, with around 29,500 instances running independently.

Each instance comprises various trigger "lines," with each line setting specific selection criteria for particular types of events.

The HLT utilizes the same software framework as the rest of LHCb. Due to the limited resources in the EFF, the processing time per event in the HLT is about fifty times shorter than in offline analysis. The HLT is structured into two stages: HLT1 and HLT2. HLT1 conducts a preliminary event reconstruction, while HLT2 completes the full event reconstruction.

A key component of the HLT is the inclusive charm and beauty trigger, which focuses on the properties of a single, high-quality track candidate. The selection criteria for this trigger involve the track's transverse momentum (p_T), typically greater than 1.6 to 1.7 GeV/c, and its impact parameter (IP), usually more than 0.1 mm. This specific trigger line produces an output of around 58 kHz, constituting the largest share of the total bandwidth allocated for HLT1 [58].

HLT1 restricts the quantity of VELO tracks that successfully passed the algorithm designed to find corresponding hits in the T-stations. These VELO tracks must either exhibit a notable IP relative to all PVs or be connected to hits in the muon chambers through a rapid muon identification process. This identification algorithm is activated only in events initially triggered by a muon line during the hardware stage.

There is also a comparable line for tracks associated with hits in the muon chambers. This specific muon trigger line selects high-quality muon candidates that are offset from the primary vertex and have a p_T exceeding 1 GeV/c. For single muon candidates with p_T over 4.8 GeV/c, a unique trigger line selects them without the need for vertex separation. Dimuon candidates are chosen based on their mass ($m_\mu >$ 2.5 GeV/c^2) without any displacement criteria, or by displacement if there is no mass constraint.

HLT1 effectively reduces the event rate to around 80 kHz, allowing all VELO tracks to undergo forward tracking in HLT2. The offline reconstruction employs two distinct tracking algorithms. HLT2, the second stage of the software trigger, now archives events at approximately 12.5 kHz for offline storage. As a deferred trigger, HLT2 operates continuously in a separate tree hierarchy, conducting filtering tasks. This secondary software trigger runs at a lower priority, fully utilizing periods when the LHC is not delivering stable beams, like during preparations for new physics runs or machine development phases, as detailed in [49]. This deferred method aids in calibrating between HLT1 and HLT2 and allows extra time for reconstruction.

Beauty decays are typically detected using multivariate analysis of displaced vertices, alongside inclusive triggers for D^0 decays and various specific decay lines. Events containing leptons with significant transverse momentum are also selected.

Due to CPU limitations, HLT2 focuses solely on identifying long tracks from VELO seeds, leading to a slightly reduced tracking efficiency of 1 - 2 % per track compared to offline reconstruction.

The processing time is further minimized by narrowing the search to tracks with $p_T >$ 80 MeV/c and p > 3 GeV/c. In HLT2, muon identification is executed using the offline muon identification algorithm.

2.4.4 TIS / TOS DEFINITION

The LHCbIDs [1] associated with the final state particles of an offline candidate can be cross-referenced with those archived by the High-Level Trigger (HLT) to ascertain if the offline candidate received approval by the trigger. This comparative analysis yields a classification termed TISTOS (Trigger independent of Signal / Trigger on Signal).

An offline candidate is categorized as TOS relative to a trigger selection if it gains acceptance by the respective trigger selection. To articulate this more formally, an offline candidate is Tos if the LHCbIDs of each of its final state particles coincide by over 70% with the LHCbIDs of the final state particles of a trigger-accepted candidate.

Conversely, an offline candidate achieves a TIS classification relative to a trigger selection if its removal from the event doesn't impede the trigger selection's acceptance of the event. This implies the presence of an alternative particle within the event that also secures acceptance by the trigger selection. Formally, this is validated when the LHCbIDs of all final state particles of any accepted candidates exhibit less than a 1% overlap with the LHCbIDs of the final state particles of the offline candidate.

For example, an event is identified as TISTISIS if it is TIS for the three trigger levels: L0, HLT1 and HLT2. The strategy for the $\mathcal{B}(\Lambda \to p\mu^-\bar{\nu}_\mu)$ measurement involves using TISTISTIS Data both for measuring the $\Lambda \to p\mu^-\bar{\nu}_\mu$ and $\Lambda \to p\pi^-$ yields to reduce uncertainties as much as possible, since any trigger requirement will imply an extra systematic uncertainty. This is possible due to the large Λ production ratio at LHCb.

2.5 LHCb UPGRADE

After the Run 2 data taking, LHC stopped for 4 years (Long Shutdown 2). During this period, the detector underwent a comprehensive upgrade, with many significant enhancements being made. These improvements enable LHCb to operate at an instantaneous luminosity five times greater than during Run 1 and Run 2 and to reconstruct data at 40 MHz LHC crossing rate, with the goal of accumulating a total integrated luminosity of approximately 50 fb^{-1} by the end of LHC Run 4 [34]. A side view of the upgraded detector can be seen in 2.5.

The **VELO** underwent a total renovation, with the main technology now centered around hybrid silicon pixel detectors. The integration of pixel-based geometry, coupled with a reduced proximity to the initial measured point and minimized material usage, has markedly enhanced the VELO's performance [32].

The **Upstream Tracker** (UT) is situated between RICH1 and the Magnet and enables a significant enhancement in acceptance compared to its predecessor, the TT. As charged particles traverse this tracking system, they produce hits; these UT hits are crucial for the initial stages of the software trigger. When combined with VELO hits, VELO-UT tracks are formed. The presence of a magnetic field in the

[1] The LHCbID class serves as a universal channel identifier across the LHCb framework. Its primary function is within the updated track model, ensuring each measurement contributing to a track's construction is distinctly marked. By having access to a set of LHCbIDs and their associated measurements, one should be able to replicate the track fitting outcomes.

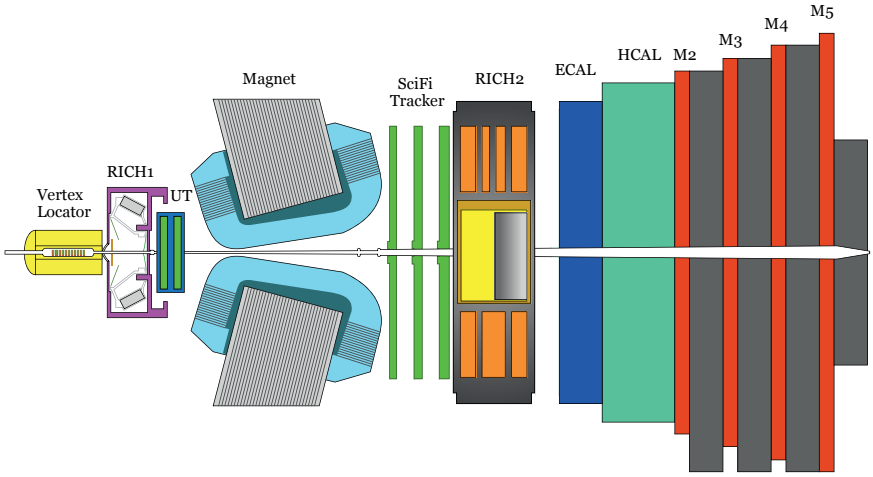

FIGURE 2.5: The LHCb upgraded detector according to the plane of curvature of the trajectory of the charged particles.

UT region enables an initial estimation of particle momentum with approximately 15% uncertainty. Additionally, UT hits substantially reduce the rate of fake tracks and can markedly boost the statistics for long-lived particles such as K_S^0 or Λ, by providing measurements of the secondary vertex for particles that decay after passing the VELO [34].

The three tracking stations downstream the magnet and before RICH2 (T1, T2 and T3) were replaced by the **Scintillating Fibre tracker** (SciFi), tasked with tracking charged particles and determining their momentum. The system must attain a momentum resolution and track efficiency for b- and c-hadrons that is on par with the performance from Run 1 and Run 2, despite operating under conditions of increased particle density [34].

The RICH detectors and calorimeters were also upgraded, while maintaining the fundamental design principles of their predecessors.

Concerning the muon system, the M_1 station was removed as it was previously utilized for the Level-0 hardware trigger, which is no longer necessary. A detailed account of the trigger system implemented in the upgrade is provided in Section 3.4.

2.6 LHCb DATA FLOW

The first step in the data flow involves data collection using the LHCb subdetectors for actual data and the simulation and digitisation processes for the Monte Carlo simulation (MC).

The simulation of events unfolds in three distinct phases: the generation of particles, facilitated by Pythia [19]; the decay of particles, managed by EvtGen [56]; and the propagation of particles through the detector, orchestrated by Geant4 [8].

The Gauss software package oversees the entire simulation process. Subsequently, the digitisation process is simulated using Boole.

The remaining stages of the data flow are consistent for both Monte Carlo (MC) and actual data. Initially, there are three trigger steps (refer to Section 2.4), supervised by the Moore software package. This is followed by the reconstruction process, conducted by Brunel, and ultimately, the stripping process, managed by DaVinci. The stripped data is stored and made accessible to analysts, who can utilize DaVinci to generate data and MC NTuples for their analyses.

A comprehensive depiction of the LHCb data flow is available in Figure 2.6.

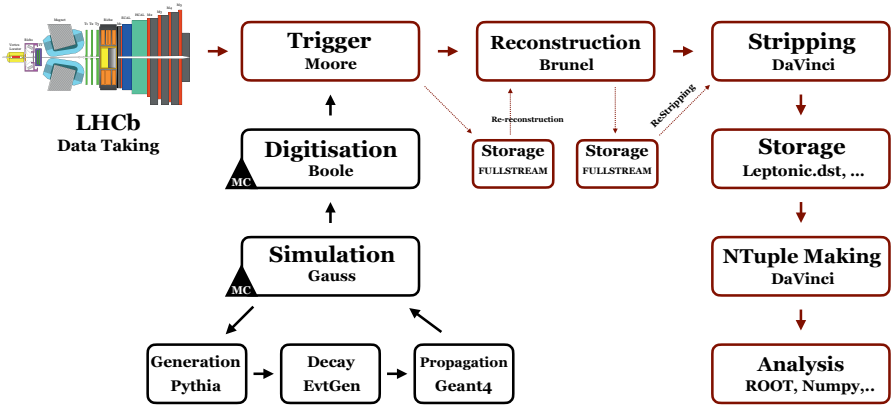

FIGURE 2.6: LHCb Data flow.

2.7 STRIPPING

The stripping process follows the trigger system and reconstruction in the data selection hierarchy. It is an software offline selection that filters specific decay channels or events of interest.

In the stripping process, predefined selection criteria, known as "lines," are applied. Each line corresponds to a specific decay channel or a set of requirements. Multiple lines collectively form a "stripping version" or "stripping configuration".

This selection is based on particle identification, kinematics, or other event characteristics. The cuts are optimized to retain as many signal events as possible while reducing the background.

Events that pass the stripping criteria are retained for further analysis. These events are stored in a more accessible format, allowing physicists to analyze them in detail.

2.8 SIMULATION SOFTWARE AND FRAMEWORKS

Simulation plays a pivotal role in high-energy physics experiments such as those conducted at LHCb. It involves the use of computational models to mimic the physical processes occurring during particle collisions and their interactions with the detector. Simulations provide a theoretical framework that aids in the interpretation and understanding of the experimental data, helping physicists to unravel the mysteries of fundamental particles and their interactions.

In the realm of LHCb experiments, various sophisticated software and frameworks play an indispensable role in the generation of accurate and reliable simulations. A notable mention is Gauss, the official LHCb software for event simulation. Gauss allows for the meticulous modeling of proton-proton collisions, subsequent particle decays, and their interactions with the detector's material, based on the prevailing theoretical models and Monte Carlo techniques. It is complemented by the Gaudi framework [17], a versatile and robust environment used for data processing and analysis within LHCb. Gaudi facilitates the efficient handling of event data, ensuring that both simulated and real data are processed through identical reconstruction and analysis chains. This congruence ensures a coherent and straightforward comparison between experimental observations and theoretical expectations, ensuring the integrity of the results.

2.8.1 EVENT GENERATION

Event generation is a key part of simulating physical processes, like those happening in experiments at LHCb. It helps turn theoretical physics ideas into a virtual form that can be studied and analyzed in detail. In LHCb experiments, event generators help simulate the first proton-proton collisions and the following series of particle decays and interactions.

These generators use Monte Carlo methods, creating many possible events that show the random nature of quantum processes. This allows for a detailed study of all possible outcomes. The event generators work based on a given particle physics theory (not only the SM, BSM models can also be considered), helping the simulations closely match what we expect to see in the real world under the correspondent theory.

Event generators are especially important for simulating rare particle decays, which are crucial for LHCb's mission to study the behaviour of particles. The events created by these generators act as a base, allowing us to compare real-life experimental results with theoretical expectations, helping us to understand the physics involved.

Pythia is a powerful tool used in the field of particle physics to simulate the generation of events in high-energy interactions, such as proton-proton collisions [19]. It provides detailed models of high-energy reactions, allowing us to understand the production and decay of particles and antiparticles. In the context of the LHCb experiment, Pythia is used by Gauss to accurately simulate the particles produced immediately after proton-proton collisions.

EvtGen is another essential tool used in particle physics simulations, specializing in the simulation of the decay of heavy particles, like those produced in proton-proton collisions [56]. After Pythia simulates the initial collision and production of particles,

EvtGen takes over to handle the detailed simulation of how these generated particles decay into lighter particles. Gauss, the overarching simulation software used in the LHCb experiment, orchestrates this process.

2.8.2 DETECTOR SIMULATION

Detector simulation is a crucial part of analyzing results in high-energy physics, helping to connect theory with actual experiment results. In the LHCb experiment, detector simulation carefully mimics the paths of particles as they move through the detector, interact with its parts, and leave behind electronic traces that we can measure. Specialized software helps to recreate the physical happenings inside the detector, capturing details like particle interactions and energy left behind. This helps us understand how the detector responds to various particles and events, making it easier to pull out useful information from the raw data.

Detector simulation creates a virtual model of the detector's actions, improving the reliability and precision of the experiment's analysis. This ensures that the conclusions drawn are based on a detailed understanding of how the detector works and performs.

Geant4 is a powerful software tool used to simulate how particles move through and interact with detectors in experiments [8] like those conducted at LHCb. Gauss is a program that uses various tools, including Geant4, to simulate the entire journey of particles produced in high-energy collisions.

After the initial collision is simulated, and the particles are produced and decayed using tools like Pythia and EvtGen, Gauss uses Geant4 to simulate the next part of the particles' journey. Geant4 helps Gauss to create a virtual replica of the LHCb detector. It carefully simulates how the particles travel through the detector, how they interact with the materials in the detector, and how these interactions leave behind signals that can be measured.

Geant4 is very detailed and can mimic the real physical processes happening inside the detector, like how particles lose energy and how they scatter. This makes the simulation very realistic, helping researchers to better understand and interpret the actual experimental data collected by the LHCb detector. By using Geant4, Gauss ensures that the simulations are as accurate and useful as possible, helping scientists to make sense of their experiments and explore the mysteries of particle physics.

2.8.3 RECONSTRUCTION AND ANALYSIS

Reconstruction and analysis are key steps in turning raw data from experiments or computer simulations into useful scientific findings. In the LHCb experiment, reconstruction means taking the basic electronic signals from the detector and turning them into a clear picture of each event. This includes figuring out which particles are present and determining their paths, speeds, and energy. Both real experiment data and simulated data go through the same reconstruction process, making sure the results are consistent and trustworthy.

During the analysis part, the refined data is closely studied to find important information about physical properties and behaviors. Different statistical methods and

data selection criteria are used to focus on specific particles or decay types. Insights from both real and simulated data work together to improve our understanding of the physics involved. This collaboration helps to make sure that the experiment results are accurate and can be confidently compared with theoretical expectations. Overall, this process helps to carefully assess the experiment's methods and results, supporting detailed and reliable discoveries about particle behaviors.

2.8.4 VALIDATION AND CALIBRATION

Validation and calibration are important steps that make simulations in the LHCb experiment more accurate and trustworthy. Validation means carefully checking that the simulated data matches up with the real experiment results. This makes sure that the simulations are a reliable tool for testing ideas and understanding data. Any differences found during validation are studied closely to improve the simulations, making them better at predicting what will happen.

Calibration is about adjusting the simulations to make sure they match the actual responses of the detector and the real experimental conditions. Since experiments can be complicated and changeable, calibration helps keep the simulations up-to-date and accurate in reflecting what is actually happening in the experiments.

Together, validation and calibration help make sure that the simulations are strong and dependable, accurately showing what happens in high-energy physics experiments. This helps increase trust in the results from the simulations, making them useful for planning experiments, understanding results, and discovering new things about the basic particles and how they interact.

2.8.5 USE OF SIMULATION IN THIS RESEARCH

In this thesis, simulation has been instrumental in refining the analysis strategy and enhancing the robustness of the results. Using the Gauss and Gaudi software frameworks, a detailed simulation of the signal and background processes was conducted. This allowed for a meticulous evaluation of the detector's response, enabling a comprehensive comparison between the simulated and real data, thereby facilitating a more accurate extraction of the physical parameters under study. For the $\mathcal{B}(\Lambda \to p\mu^-\bar{\nu}_\mu)$ measurement, we generated specific $\Lambda \to p\mu^-\bar{\nu}_\mu$ and $\Lambda \to p\pi^-$ simulation samples (using a specific EvtGen model for the $\Lambda \to p\mu^-\bar{\nu}_\mu$) passing the $\Lambda \to p\mu^-\bar{\nu}_\mu$ stripping line. For the normalization, we used MinBias MC (see next section) samples to compute the efficiencies needed to compute the total amount of Λ particles in the data sample.

2.8.6 MINIMUM BIAS SIMULATION

A minimum bias (MinBias) simulation aims to resemble as close as possible typical LHCb events without introducing any bias. A complete list of the Pythia processes that are included in the MinBias MC can be found in [33]. This kind of simulation will be used in the normalization process in our case.

When normalizing against modes that exhibit high yields in Minimum Bias events (such as $\Lambda \to p\pi^-$, $K_S^0 \to \pi^+\pi^-$), utilizing specific Decay Files with imposed generator-level cuts for these modes offers no particular advantage. Note that such two-body decays do not require a dedicated EvtGen model. In practice, one is likely to encounter a greater number of these decays in the underlying event. Implementing generator-level cuts complicates matters, as it becomes challenging to ascertain which decay the cuts have impacted, making efficiency calculations increasingly complex. Opting for Minimum Bias allows for a straightforward calculation of the combined generation-level and reconstruction efficiencies in a single step. With an adequately sized Minimum Bias sample, statistical concerns should not arise.

CHAPTER 3

STRANGE PHYSICS AT LHCb

Precise measurements of the $b \to c$ transition provide hints of Lepton Flavor Universality (LFU) breaking [30], which could point to physics Beyond the Standard Model (BSM). It is natural to investigate whether similar behavior occurs in other charged-current decays of d-type quarks, namely $s \to u$.

The LHCb experiment has shown its capability to obtain leading strange physics measurements, particularly searching for their rare decays. In fact, the LHCb collaboration has published the world's most precise measurement in $K_S^0 \to \mu^+\mu^-$, $K_S^0 \to \mu^+\mu^-\mu^+\mu^-$, and $\Sigma^+ \to p\mu^+\mu^-$ [2] [4], [3].

In the last decades the focus was in the higher mass sector of the CKM matrix. However it is the low mass sector, V_{ud} and V_{us}, where is it possible to obtain the highest precision and the most sensitive test of the unitary of the CKM matrix [23].

For the CKM matrix to be unitary, $|V_{ud}|^2 + |V_{us}|^2 + |V_{ub}|^2 \equiv 1$. Since $|V_{ub}|$ has been measured to be 0.00369 ± 0.00011 [78], $|V_{ub}|^2$ is almost negligible and the unitary test reduces to $|V_{ud}|^2 + |V_{us}|^2 = 1$, which can be expressed in terms of the Cabibbo angle (θ_c) as $\cos^2\theta_c + \sin^2\theta_c = 1$. Experimentally, $|V_{ud}|$ can be determined from nuclear beta decay [53], and $|V_{us}|$ can be measured in strangeness-changing semileptonic decays [20]. Precise determination of the $s \to u$ transition is therefore an important component of validating the unitarity of the CKM matrix.

As it was explained in the Introduction, a 2.2σ tension with the expected unitarity was observed in the first CKM row unitarity test. The measurements of V_{us} in leptonic ($K_{\mu 2}$) and semileptonic (K_{l3}) kaon decays exhibit also a 3σ discrepancy [72].

Taking this into account, it is necessary to measure V_{us} with high precision and Semileptonic Hyperon Decays (SHD) are the natural alternative.

From a theoretical standpoint, studies have demonstrated that the SHD (refer to Fig. 3.1 for a list of hyperons) can potentially detect specific BSM dynamics that break leptonic universality. These decays are governed by a minor SU(3) flavor breaking parameter, enabling systematic expansions and precise predictions in terms of a reduced dependence on hadronic form factors. Muonic decays are particularly

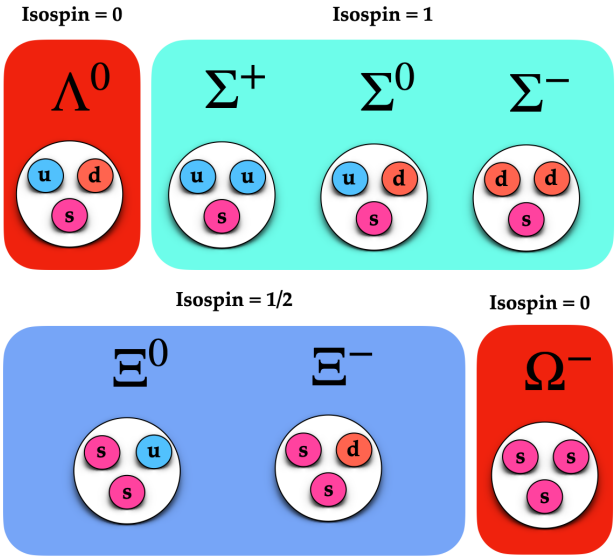

FIGURE 3.1: A hyperon is any baryon containing one or more strange quarks, but no charm bottom, or top quark, being the Λ the lightest of them. The expected yields for semileptonic hyperon decays in LHCb are large.

sensitive to scalar and tensor deviation contributions. Such patterns could complement direct searches for new physical phenomena at the LHC [26].

The LFU test observable defined as the ratio between muon and electron modes

$$R^{\mu e} = \frac{\Gamma(B_1 \to B_2 \mu^- \bar{\nu}_\mu)}{\Gamma(B_1 \to B_2 e^- \bar{\nu}_e)} \tag{3.1}$$

is sensitive to non standard scalar and tensor contributions [26] . Moreover, in the SM, the dependency on the form factors is anticipated to simplify when considering the ratio. Indeed, by operating at Next-to-Leading Order (NLO), we achieve:

$$R^{\mu e}_{\mathrm{SM}} = \sqrt{1 - \frac{m_\mu^2}{\Delta^2}}\left(1 - \frac{9}{2}\frac{m_\mu^2}{\Delta^2} - 4\frac{m_\mu^4}{\Delta^4}\right) + \frac{15}{2}\frac{m_\mu^4}{\Delta^4}\operatorname{arctanh}\left(\sqrt{1 - \frac{m_\mu^2}{\Delta^2}}\right)$$

where $\Delta = M_2 - M_1$.

This prediction is remarkable, since up to this relative theoretical precision ($O(\frac{(M_1-M_2)^2}{M_1^2})$) the ratio does not depend on form factors [26].

In 2019 we published a paper, Ref. [10] describing some prospects for measurements with strange hadrons at LHCb. A table with the acceptance efficiencies and invariant mass resolutions for the studied strange hadron decays can be found in Tab. 3.1. The production rate in LHCb, compared to the K^0_S one, was also computed (see Fig. 3.2).

TABLE 3.1: In this study, the acceptances and invariant mass resolutions for key strange channels were evaluated using a simulation based on the upgraded tracking of the LHCb. The calculated acceptances were then normalized with respect to the fully reconstructed $K_S^0 \to \mu^+\mu^-$, which has been determined to be 1%. The efficiency has been presented for both long and downstream tracks, and the invariant mass resolution has been shown for each reconstruction method, as detailed in [10]. Here, $\mathcal{R}$ represents the production ratio relative to the K_S^0 one.

Channel	$\mathcal{R}$	ϵ_L	ϵ_D	σ_L $(\frac{MeV}{c^2})$	σ_D $(\frac{MeV}{c^2})$
$K_S^0 \to \mu^+\mu^-$	1	1.0 (1.0)	1.8 (1.8)	~3.0	~8.0
$K_S^0 \to \pi^+\pi^-$	1	1.0 (0.30)	1.9 (0.91)	~2.5	~7.0
$K_S^0 \to \pi^0\mu^+\mu^-$	1	0.93 (0.93)	1.5 (1.5)	~35	~45
$K_S^0 \to \gamma\mu^+\mu^-$	1	0.85 (0.85)	1.4 (1.4)	~60	~60
$K_S^0 \to \mu^+\mu^-\mu^+\mu^-$	1	0.37 (0.37)	1.1 (1.1)	~1.0	~6.0
$K_L^0 \to \mu^+\mu^-$	~1	2.7 (2.7) $\times 10^{-3}$	0.014 (0.014)	~3.0	~7.0
$K^+ \to \pi^+\pi^+\pi^-$	~2	9.0 (0.75) $\times 10^{-3}$	41 (8.6) $\times 10^{-3}$	~1.0	~4.0
$K^+ \to \pi^+\mu^+\mu^-$	~2	6.4 (2.3) $\times 10^{-3}$	0.030 (0.014)	~1.5	~4.5
$\Sigma^+ \to p\mu^+\mu^-$	~0.13	0.28 (0.28)	0.64 (0.64)	~1.0	~3.0
$\Lambda \to p\pi^-$	~0.45	0.41 (0.075)	1.3 (0.39)	~1.5	~5.0
$\Lambda \to p\mu^-\bar{\nu}_\mu$	~0.45	0.32 (0.31)	0.88 (0.86)	-	-
$\Xi^- \to \Lambda\mu^-\bar{\nu}_\mu$	~0.04	39 (5.7) $\times 10^{-3}$	0.27 (0.09)	-	-
$\Xi^- \to \Sigma^0\mu^-\bar{\nu}_\mu$	~0.04	24 (4.9) $\times 10^{-3}$	0.21 (0.068)	-	-
$\Xi^- \to p\pi^+\pi^-$	~0.04	0.41 (0.05)	0.94 (0.20)	~3.0	~9.0
$\Xi^0 \to p\pi^-$	~0.03	1.0 (0.48)	2.0 (1.3)	~5.0	~10
$\Omega^- \to \Lambda\pi^-$	$\sim 10^{-3}$	95 (6.7) $\times 10^{-3}$	0.32 (0.10)	~7.0	~20

3.1 $\Lambda \to p\mu^-\bar{\nu}_\mu$

Among the studied channels, $\Lambda \to p\mu^-\bar{\nu}_\mu$[1] is one of the more interesting SHD due to its high reconstruction efficiency and because, being the lightest hyperon, it is the most abundant in LHCb. The purpose of the main analysis in this thesis is to measure its branching ratio using the LHCb Run2 data sample.

In [10] we proposed a strategy to separate $\Lambda \to p\mu^-\bar{\nu}_\mu$ from the main background, $\Lambda \to p\pi^-$, using the missing perpendicular momentum in the Λ direction of flight vs $M(p\mu)$ plane.

[1] From now on, when discussing the decay modes such as $\Lambda \to p\mu^-\bar{\nu}_\mu$, $\Lambda \to p\pi^-$, among others, we will always implicitly include the charge-conjugate modes as well.

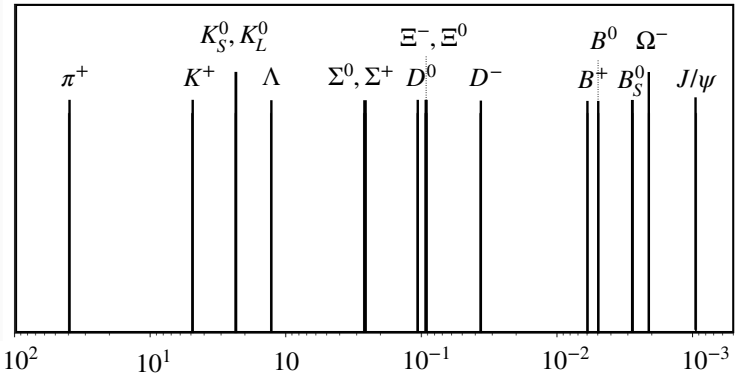

FIGURE 3.2: Multiplicity of particles produced in a single pp interaction at $\sqrt{s}$ = 13 TeV within LHCb acceptance.

In 2019, I studied a background rejection strategy in the search for $\Lambda \to p\mu^-\bar{\nu}_\mu$, published as an LHCb public figure [13], where the $\Lambda \to p\pi^-$ yield in LHCb Run 2 was presented. In addition, the strategy to separate $\Lambda \to p\mu^-\bar{\nu}_\mu$ and $\Lambda \to p\pi^-$ proposed in our previous paper using the 2D plane was verified using a LHCb full simulation.

Using this public result, I presented in a talk at the KAON 2019 conference the $\Lambda \to p\mu^-\bar{\nu}_\mu$ expected yield in LHCb after the selection. The statistical uncertainty should be at the level of 1%, which implies that we will be dominated by systematic uncertainties. The talk is summarized in my proceedings [68].

Considering that we will be dominated by systematic uncertainties was crucial in order to design the analysis strategy. For example, as can be seen in Tab. 3.1, the use of downstream tracks can significantly enhance the $\Lambda \to p\mu^-\bar{\nu}_\mu$ statistics. The trade-off would be worse resolution in several observables and larger systematic uncertainties. Considering that we will be dominated by systematic uncertainties and that a good vertex, mass, and momentum resolution are essential for this analysis, we decided to use exclusively long tracks.

In a similar way, aiming to reduce systematics as much as possible, we decided to use only TISTISTIS (see 2.4.4) data both for normalization and signal samples. By doing this we avoid the MC/Data corrections related to the trigger process.

It is crucial to note that $\Lambda \to p\pi^-$ will be utilized as the normalization channel. Consequently, it will serve simultaneously as the primary background in the signal yield fit and as normalization channel.

In 2021, BESIII published the first measurement of the absolute branching fraction of $\Lambda \to p\mu^-\bar{\nu}_\mu$, obtaining the current best branching fraction measurement, $\mathcal{B}(\Lambda \to p\mu^-\bar{\nu}_\mu) = (1.48 \pm 0.21) \times 10^{-4}$ [6]. The current PDG average is $(1.51 \pm 0.19) \times 10^{-4}$ [78].

The LFU test observable is predicted by theory to be $R^{\mu e} = 0.153 \pm 0.008$ working

at next-to-leading order [26]. Current best measurement of this observable, using the BESIII result, obtaining $R^{\mu e} = 0.178 \pm 0.028$, consistent within uncertainties with the predicted value [6].

Our goal is to obtain a better measurement of $\mathcal{B}(\Lambda \to p\mu^-\bar{\nu}_\mu)$, and subsequently of $R^{\mu e}$, using the data collected in LHCb during the Run II. For this, we need a total uncertainty below 14 % to improve the accuracy.

3.2 PROSPECTS FOR OTHER SEMILEPTONIC HYPERON DECAYS AT LHCb

The general SHD case can be descripted as $B_1 \to B_2 l^- \bar{\nu}_l$, where B_1 is the hyperon, B_2 is the baryon in the final state and l can be any lepton flavor. As it will be explained in detail in the $\mathcal{B}(\Lambda \to p\mu^-\bar{\nu}_\mu)$ analysis description (Sec. 5.1), the $\Delta = B_1 - B_2$ magnitude is directly related to the success of the developed strategy to separate signal and background.

This is because a bigger Δ implies more momentum available for the neutrino. In the $\Lambda \to p\mu^-\bar{\nu}_\mu$ case, the neutrino momentum distribution is relatively close to to the LHCb momentum resolution. This makes harder to separate $\Lambda \to p\mu^-\bar{\nu}_\mu$ events and $\Lambda \to p\pi^-$ events (where there is not neutrino at all and the computed missing momentum should be 0).

Additionally, we found that the abundance of Λ particles can introduce certain disadvantages, as it necessitates very tight cuts in the stripping lines. Consequently, generating MC simulations for $\Lambda \to p\pi^-$ and minimum bias that pass the stripping line, specifically designed to select $\Lambda \to p\mu^-\bar{\nu}_\mu$, becomes exceptionally resource-intensive. However, this issue will be reduced for heavier hyperon modes.

Lastly, the combinatorial background emerged as one biggest challenges to deal with. This is partly due to the complexities involved in generating combinatorial background MC passing the signal stripping line. But also because it is harder to separate from signal than peaking backgrounds.

Considering all these ideas, the ideal SHD case will have a big Δ and will allow us to reduce the combinatorial background. In Tab. 3.2 the Δ value for several SHD is listed, including also the production ratio and the acceptance efficiencies using long and downstream tracks. The current PDG branching ratio is also listed [78].

3.2.1 $\Xi^- \to \Lambda\mu^-\bar{\nu}_\mu$

Among the semileptonic hyperon decays presented in Tab. 3.2, the most promising channel based on its high Δ is $\Xi^- \to \Lambda\mu^-\bar{\nu}_\mu$. Its branching ratio has an uncertainty at the 100 % level, and it presents a bigger Δ than the $\Lambda \to p\mu^-\bar{\nu}_\mu$ case.

Despite having one order of magnitude less both in acceptance efficiency in the LHCb detector and in production ratio, the strategy designed for $\Lambda \to p\mu^-\bar{\nu}_\mu$ should be enough to improve its branching ratio measurement. Downstream tracks can be included if needed to enhance statistics by one order of magnitude.

Moreover, having a Λ in the final state, that will be reconstructed in the $\Lambda \to p\pi^-$ mode, will reduce significantly the combinatorial background pollution. This makes

TABLE 3.2: The acceptances and invariant mass resolutions for different SHD channels were evaluated using a simulation based on the upgraded tracking of the LHCb. The calculated acceptances were then normalized with respect to the fully reconstructed $K_S^0 \to \mu^+\mu^-$, which has been determined to be 1%. The efficiency has been presented for both long and downstream tracks. Here, $\mathcal{R}$ represents the production ratio relative to the K_S^0 one. The difference between mother and daughter baryons (Δ) and the branching ratio of each channel is also presented.

Channel	$\mathcal{R}$	$\Delta\ (MeV/c^2)$	ϵ_L	ϵ_D	$\mathcal{B}$
$\Lambda \to p\mu^-\bar{\nu}_\mu$	~ 0.45	~ 177.41	0.32	0.88	$(1.51 \pm 0.19) \times 10^{-4}$
$\Xi^- \to \Lambda\mu^-\bar{\nu}_\mu$	~ 0.04	~ 206.03	0.039	0.27	$(3.5^{+3.5}_{-2.2}) \times 10^{-4}$
$\Xi^- \to \Sigma^0\mu^-\bar{\nu}_\mu$	~ 0.04	~ 129.07	0.024	0.21	$< 8.0 \times 10^{-4} (90\% CL)$
$\Xi^0 \to \Sigma^+\mu^-\bar{\nu}_\mu$	~ 0.04	~ 125.49	-	-	$(2.33 \pm 0.35) \times 10^{-6}$
$\Sigma^- \to n\mu^-\bar{\nu}_\mu$	~ 0.13	~ 249.80	-	-	$(4.5 \pm 0.4) \times 10^{-4}$

the $\Xi^- \to \Lambda\mu^-\bar{\nu}_\mu$ channel the most promising one to continue measuring SHD branching ratios at LHCb.

Additionally, $\Xi^- \to p\pi^+\pi^-$ can be used as normalization channel. This mode has an acceptance efficiency similar to the $\Lambda \to p\pi^-$ one (see Tab. 3.1) and we will have a huge amount of statistics for the normalization process.

Notice that the $\Sigma^- \to n\mu^-\bar{\nu}_\mu$ channel, even having a bigger Δ, presents a neutron in the final state, which makes it harder to measure.

3.2.2 $\Lambda \to pe^-\bar{\nu}_e$

This branching ratio is already well measured, $\mathcal{B}(\Lambda \to pe^-\nu_e) = (8.34 \pm 0.14) \times 10^{-4}$ [78]. Despite this, to measure also the $\mathcal{B}(\Lambda \to pe^-\nu_e)$ in LHCb will be the ideal case in order to measure $R^{\mu e}$ directly using only LHCb data.

The pros of this channel are that its branching ratio is approximately one order of magnitude greater than the $\Lambda \to p\mu^-\bar{\nu}_\mu$ one and that the $\Lambda \to p\pi^-$ pollution will be reduced, since pions mainly decay in flight to a muon and a neutrino due to helicity suppression.

Even taking into account that is easier to measure muons than electrons in LHCb, the posibility of studying also this mode in order to measure $R^{\mu e}$ in LHCb deserves consideration.

3.2.3 MILESTONES

As part of this thesis work, stripping lines for several SHD were designed and merged in the DaVinci software. This means that we already have Run2 stripped data to study other SHD.

In addition, I developed a EvtGen model that can properly simulate SHD decays (see Ch. 5.3. This model is also merged in Gauss, the official LHCb software for simulation, allowing to generate MC for any SHD analysis.

With stripped data, the EvtGen model and a functional strategy, the door for studying SHD at LHCb is now open.

3.3 $K_S^0 \to \mu^+\mu^-$

The LHCb collaboration has published in 2020 the world's most precise limit for the $\mathcal{B}(K_S^0 \to \mu^+\mu^-)$, reaching the impressive result of $\mathcal{B}(K_S^0 \to \mu^+\mu^-) < 2.1 \times 10^{-10}$ at 90 % CL [2].

This flavor changing neutral current process has never been observed. The $K_S^0 \to \mu^+\mu^-$ decay is extremely suppressed in the SM, and its branching ratio is predicted to be [55] [39]:

$$\mathcal{B}(K_S^0 \to \mu^+\mu^-)_{\text{SM}} = (5.18 \pm 1.50_{LD} \pm 0.02_{SD}) \times 10^{-12} \tag{3.2}$$

where LD stands for long distance and SD for short distance contributions.

Consequently, tiny BSM contributions ($O(10^{-12})$) will produce observable deviations in the $\mathcal{B}(K_S^0 \to \mu^+\mu^-)$. This makes this channel extremely useful for testing leptoquark[21] and Supersymmetry (SUSY) [29] models.

This thesis made a significant contribution to the LHCb measurement, allowing to effectively control the background from the $K_S^0 \to \pi^+\mu^-\bar{\nu}_\mu$ decay process by developing a new EvtGen model and generating a full simulation as explained below.

3.3.1 SKD EVTGEN MODEL

A specific EvtGen Model was created in order to generate $K_S^0 \to \pi\mu\nu$ with the proper kinematic distributions.

The differential decay rate por Semileptonic Kaon Decays (SKD) is described in the (E_l^*, E_π^*) Dalitz plot as

$$\frac{d^2\Gamma}{dE_l^* dE_\pi^*} = N(A_1|f_+(t)|^2 + A_2 f_+(t) f_-(t) + A_3|f_-(t)|^2) \tag{3.3}$$

where E_l^* and E_π^* are the lepton and pion energies in the kaon rest frame; t is the 4-momentum transfer to the leptonic system; N is just a numerical factor; $f_-(t) = (f_0(t) - f_+(t))(m_K^2 - m_\pi^2)/t$; m_K and m_π are the kaon and pion masses. In (3.3),

$$A_1 = m_K(2E_l^* E_\nu^* - m_k(E_\pi^{*,max} - E_\pi^*)) + m_l^2((E_\pi^{*,max} - E_\pi^*)/4 - E_\nu^*) \tag{3.4}$$

$$A_2 = m_l^2(E_\nu^* - (E_\pi^{*,max} - E_\pi^*)/2) \tag{3.5}$$

$$A_3 = m_l^2(E_\pi^{*,max} - E_\pi^*)/4 \tag{3.6}$$

where $E_\pi^{*,max} = (m_K^2 + m_\pi^2 - m_l^2)/2m_K$. The f functions were parameterizated with a Taylor expansion, including second order terms.

$$f_+(t) = 1 + \lambda_+^{'}\frac{t}{m_\pi^2} + \frac{1}{2}\lambda_+^{''}(\frac{t}{m_\pi^2})^2, \quad f_0(t) = 1 + \lambda_0\frac{t}{m_\pi^2} \tag{3.7}$$

We used the results of the recent NA48/2 measurement of the form factors of kaon semileptonic decays [18]:

TABLE 3.3: Form factor results of the joint $K^{\pm}_{l3}$ analysis. The units of λ'_+, λ''_+ and λ_0 are 10^-3.

	λ'_+	λ''_+	λ_0
Central values	24.24	1.67	14.47
Statistical error	0.75	0.29	0.63

I developed an EvtGenProb Model that uses the value obtained from 3.3 in an accept-reject method [28]. The resulting EvtGen model is called **SKD** and it takes as an input only the maximum value of the differential rate.

SKD model was tested, showing a good agreement between the output and the NA48/2 results.

This model was used to generate the $K^0_S \to \pi^+\mu^-\bar{\nu}_\mu$ simulation used to consider this background contribution in the LHCb search for $K^0_S \to \mu^+\mu^-$.

3.4 ALLEN AND STRANGE PHYSICS IN THE UPGRADE

Although this thesis exclusively utilizes data from LHCb Run 2, it is noteworthy that the detector underwent an upgrade during the Long Shutdown 2 period from 2018 to 2022, which may have implications for the LHCb program's studies of strange physics.

The primary potential enhancement to the strange physics program is not a result of the detector upgrade, but rather from the implementation of the new trigger system. This new trigger is called Allen [1] and it is a fully GPU-based high-level trigger.

Before the upgrade, the LHCb experiment had a system with two steps for deciding which particle collision events to keep for study. The first step, called L0 (Level 0), was hardware-based and made very fast decisions to reduce the data rate significantly before passing it to the next trigger step, the High Level Trigger, HLT. Then, the second HLT step, used computer software to look more closely at those chosen events to decide which ones were really worth saving to look at later.

One of the most significant trigger criteria implemented during LHCb Run 1-2 in the L0 trigger was related to the transverse momentum (p_T) of the particles. Given that strange particles generally have lower p_T compared to the typical particles targeted by LHCb for reconstruction, this hardware-based trigger posed challenges for efficiently triggering on strange particles.

One of the suggested strategies to trigger in some benchmarks strange channels as $K^0_S \to \mu^+\mu^-$, proposed even before the Allen proposal, was the VELO-UT-Muon matching algorithm.

3.4.1 VELO-UT-MUON MATCHING ALGORITHM

This algorithm was proposed to trigger on low p_T muons, one of the main challenges in the study of the strange particles in LHCb. The algorithm's idea is to construct VELO-UT (the UT is the Upstream Tracker, subdetector of the LHCb upgraded detector)

tracks and to extrapolate those tracks to the muon stations without considering the SciFi hits. The VELO-UT tracks are extrapolated to the muon chambers by applying a kink to reproduce the magnet bending effect. As a consequence, a track is stored based only in the hits distributions in the muon chambers. Considering the low occupancy in the muon chambers, this will allow to reconstruct muons with a p_T similar to the LHCb acceptance threshold, $\approx 80\ MeV/c$.

A depiction of the algorithm's operation is illustrated in Fig. 3.3. Initially, tracks are formed by correlating hits from the VELO and the UT. Owing to the magnetic field in the UT area, these VELO-UT tracks exhibit a momentum resolution of about 15%. The approximation of the magnetic field's influence involves a kink at the deflection point, equivalent to the magnet focal plane, which is located at

$$z_f = a - b.t_x^2 \tag{3.8}$$

where t_x represents the measured slope of the VELO track, with parameters a and b derived from fitting the intersections of the SciFi and VELO segments [67]. The adjustment in the track slopes introduced by the magnet is associated with the particle's momentum.

$$|\Delta t_x| = \frac{\alpha}{p - \beta} \tag{3.9}$$

The α and β parameters are also fitted, obtaining $\alpha = 1236.59\ MeV/c$ and $\beta = 311.84\ MeV/c$ as best values [67].

Once the track deflection is computed, it is extrapolated to the muon chambers and a search for hits near the determined trajectory (field of interest, FoI) is applied. The muon chamber that a particle can reach is given by its momentum.

When hits meet the criteria set by the input track's momentum, the track is considered successful in passing the algorithm, provided that the ratio of the chi-square of the fit to the degrees of freedom, involving the hit positions and the magnet's focal plane, is below 20 [67].

Part of the work developed during this thesis involved translating this algorithm from `C++` (CPU) to `CUDA` (an API from NVIDIA for GPU programming [41]). The goal was to include this algorithm in the early stages of the proposed HLT1 trigger, which is fully implemented on GPUs. This implementation was ultimately selected as the HLT1 trigger for the LHCb upgrade, known as Allen [1].

3.4.2 ALLEN

The LHCb trigger strategy depends on more than just signs of high-energy events, like those used in the hardware triggers of high-energy experiments such as ATLAS and CMS. It also focuses on tracking and reconstructing secondary vertices in the event.

Tracking and putting together the points where particles cross or decay, which are key parts of how LHCb builds up and chooses what to look at, use highly-parallelizable methods, making them well-suited for graphics cards (GPUs) [57]. For the first time in high-energy physics, an experiment has set up a stage of its software trigger to run completely on GPUs, Allen.

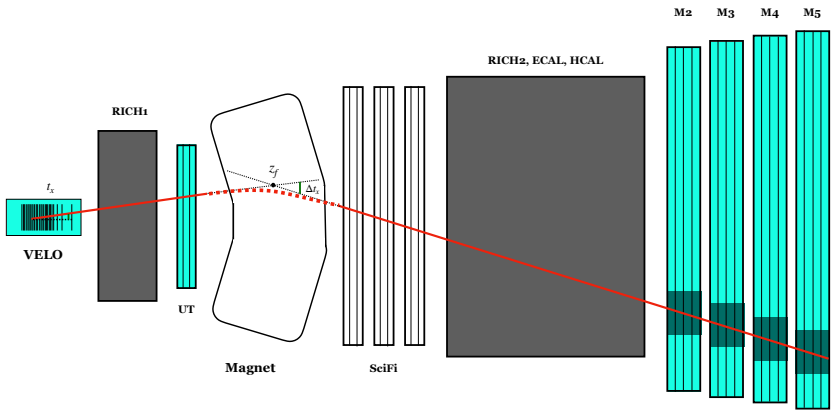

FIGURE 3.3: Simplified side view of the LHCb detector and a graphic representation of the VELO-UT muon matching algorithm. The implied subdetectors are highlighted in blue.

The GPU-based implemented technology of Allen contributed to make possible the removal of the hardware trigger. This hardware trigger, based on selecting only high-energy particles, reduced significantly the strange physics statistics during Run 2.

As a consequence, Allen's flexibility makes possible to develop different strategies to trigger on strange particles. For instance, the HLT now enables triggering based on displacement, which is advantageous for the strange physics program, as particles with lower mass tend to travel further within the detector.

The updated reconstruction sequence delivers remarkable results for the decay products of low-momentum signals, particularly for Kaons and other strange particles. The overall efficiency for Forward-tracking tracks originating from strange particle decays stands at 76.5% for energies above 3 GeV and 81.4% for energies above 5 GeV. This represents an improvement of more than double per track compared to the HLT1 Forward-tracking reconstruction utilized in Run 2. Consequently, there is no longer a requirement for distinct reconstruction processes for low-momentum particles at the HLT1 level. This not only streamlines the reconstruction sequence but also ensures uniformity in the HLT1 Forward-tracking reconstruction [60].

CHAPTER 4

OBJECTIVES AND METHODOLOGY

This thesis has clear goals that aim to help us learn more about lepton flavour universality. The main goal is to add new knowledge to what we already know and to check if what we think we know is really true by carefully looking at the data and what it shows us.

4.1 OBJECTIVES

The primary goal of this thesis is to measure precisely $\mathcal{B}(\Lambda \to p\mu^-\bar{\nu}_\mu)$, surpassing all existing measurements to set a new world record for precision. Since the $\Lambda \to pe^-\bar{\nu}_e$ electron mode has already been measured very precisely ($\mathcal{B}(\Lambda \to pe^-\bar{\nu}_e) = (8.34 \pm 0.14) \times 10^{-4}$ [78]) and the SM gives us a clean prediction for the ratio between the muonic and electron modes, a improved measurement of the $\mathcal{B}(\Lambda \to p\mu^-\bar{\nu}_\mu)$ can directly translates into a search for BSM dynamics that can modify the branching fraction.

As a result, this measurement will imply new constraints in LFU in $s \to u$ quark transitions.

4.2 METHODOLOGY

First of all, it is important to mention that this is not a direct $\mathcal{B}(\Lambda \to p\mu^-\bar{\nu}_\mu)$ measurement. The branching fraction will be measured using $\Lambda \to p\pi^-$ as normalization channel, and incorporating $\mathcal{B}(\Lambda \to p\pi^-)$ as an input.

The underlying principle is to fit the amount of $\Lambda \to p\mu^-\bar{\nu}_\mu$ and $\Lambda \to p\pi^-$ events in the Run 2 LHCb dataset (using TISTISTIS data) and, dividing those extracted yields by the efficiencies computed with our MC, extract the total amount of $\Lambda \to p\mu^-\bar{\nu}_\mu$ and $\Lambda \to p\pi^-$ generated at LHCb during the 2016-2018 period.

Dividing the number of $\Lambda \to p\pi^-$ by the $\mathcal{B}(\Lambda \to p\pi^-)$ we can compute the total amount of Λ particles. Afterwards, we can divide this number by the total $\Lambda \to p\mu^-\bar{\nu}_\mu$ yield to compute $\mathcal{B}(\Lambda \to p\mu^-\bar{\nu}_\mu)$.

The normalization fit will be performed to a double sided crystal ball + an exponential PDF using the M(pπ) variable where $\Lambda \to p\pi^-$ peaks. The crystal ball tail parameters will be extracted by fitting the $\Lambda \to p\pi^-$ MC. Previously some cuts will be introduced to remove the $K^0_S \to \pi^+\pi^-$ component.

The signal yield will be determined through a binned two-dimensional (2D) fit in a plane that reasonably separates $\Lambda \to p\pi^-$ and $\Lambda \to p\mu^-\bar{\nu}_\mu$. This fit will utilize Poisson statistics and employ the MC distributions as templates. The adoption of a 2D fit aids in managing the challenge posed by low background MC statistics.

Various systematic uncertainties will be considered and calculated. Most will pertain to discrepancies between data and Monte Carlo behaviors, with the most significant arising from the choice of binning scheme and modes in the 2D fit.

The $\Lambda \to p\mu^-\bar{\nu}_\mu$ MC utilized is generated with a specific EvtGen model to verify its differential decay rate, and both $\Lambda \to p\mu^-\bar{\nu}_\mu$ and $\Lambda \to p\pi^-$ MC samples are produced using LHCb's full simulation, passing through all the steps of the LHCb data-flow. Minimum Bias (MinBias) MC is employed to determine the efficiency and behavior of $\Lambda \to p\pi^-$ for the normalization channel.

CHAPTER 5

ANALYSIS

The main challenge associated to the $\mathcal{B}(\Lambda \to p\mu^-\bar{\nu}_\mu)$ measurement at LCHb will be discriminating the signal from peaking background, primarily from $\Lambda \to p\pi^-$ decays, but also from $K^0_S \to \pi^+\pi^-$ decays. In addition, removing the combinatorial background can be challenging due to the presence of a neutrino in the $\Lambda \to p\mu^-\bar{\nu}_\mu$ final state, which results in missing momentum that we have to account for.

Only long tracks will be used in this analysis. As we are not dominated by statistical uncertainties, there is no pressing need to include downstream tracks, whose resolution could adversely affect the measurement. This is because our kinematic strategies heavily rely on having a good resolution.

To generate simulated events that reproduce the theoretical kinematic distributions, a new EvtGen [56] model will be necessary. The next step will involve studying the signal properties and comparing them with those of the background. Subsequently, we will develop selection criteria to effectively separate the signal from the background and, ultimately, obtain an estimated value for the expected yield of $\Lambda \to p\mu^-\bar{\nu}_\mu$ decays at LHCb.

The branching ratio can be expressed as the number of Λ decaying to $p\mu^-\bar{\nu}_\mu$ in our dataset over the total amount of Λ particles in our dataset:

$$\mathcal{B}(\Lambda \to p\mu^-\bar{\nu}_\mu) = \frac{N(\Lambda \to p\mu^-\bar{\nu}_\mu)}{N(\Lambda)} \tag{5.1}$$

being

$$N(\Lambda \to p\mu^-\bar{\nu}_\mu) = \frac{N^{\text{reco}}_{p\mu\nu}}{\epsilon_{p\mu\nu}} \tag{5.2}$$

where $N^{\text{reco}}_{p\mu\nu}$ is the number of $\Lambda \to p\mu^-\bar{\nu}_\mu$ events reconstructed and selected as signal and $\epsilon_{p\mu\nu}$ is the efficiency of this process, extracted from Monte Carlo (MC) studies. Applying Eq. 5.1 and Eq. 5.2 to the $\Lambda \to p\pi^-$ case, is easy to obtain

$$\mathcal{B}(\Lambda \to p\pi^-) = \frac{N^{\text{reco}}_{p\pi}}{\epsilon_{p\pi} N(\Lambda)} \tag{5.3}$$

and combining previous equations arrive to:

$$\mathcal{B}(\Lambda \to p\mu^-\overline{\nu}_\mu) = \mathcal{B}(\Lambda \to p\pi^-)\frac{\epsilon_{p\pi}}{\epsilon_{p\mu\nu}}\frac{N^{\text{reco}}_{p\mu\nu}}{N^{\text{reco}}_{p\pi}} \tag{5.4}$$

So, we can define an α parameter that relates the $\Lambda \to p\mu^-\nu$ branching ratio and the number of reconstructed signal events $N^{\text{reco}}_{p\mu\nu}$,

$$\mathcal{B}(\Lambda \to p\mu^-\overline{\nu}_\mu) = \alpha N^{\text{reco}}_{p\mu\nu} \tag{5.5}$$

being

$$\alpha = \frac{\mathcal{B}(\Lambda \to p\pi^-)}{N^{\text{reco}}_{p\pi}}\frac{\epsilon_{p\pi}}{\epsilon_{p\mu\nu}} \tag{5.6}$$

Once we calculate the α parameter, using the PDG value for the $\mathcal{B}(\Lambda \to p\pi^-)$, we will be able to obtain the expected yield.

Two Stripping Lines with aligned cuts have been created, as will be explained in the next section. The first one is for normalization, where we can fit the yield of $\Lambda \to p\pi^-$ decays, while the other one aims to maximize signal purity.

During the Run2, LHCb had 3 trigger levels (L0, HLT1 and HLT2). As clarification, an offline candidate is considered to be TIS with respect to a trigger selection if removing it from the event would still cause the trigger selection to accept the event. TISTISTIS means that the event is TIS for the L0, the HLT1 and the HLT2 Trigger.

Both fits will be performed to TISTISTIS Data, to reduce systematic uncertainties to the minimum.

5.1 ANALYSIS STRATEGY

The $\Lambda \to p\mu^-\bar{\nu}_\mu$ branching ratio will be obtained using as input the $\mathcal{B}(\Lambda \to p\pi^-)$. Two Stripping Lines have been written with this purpose, the normalization one (NormLine) to select $\Lambda \to p\pi^-$ and measure its yield and the signal one (SignalLine) to select $\Lambda \to p\mu^-\bar{\nu}_\mu$ and measure its yield. Cuts in both lines are aligned to reduce systematic errors, being the particle ID cuts and the mass window the only difference between them.

In addition, we have a MinBias MC Sample for 2018 MD and 2018 MU, and a Stripping Filtered Production for both $\Lambda \to p\pi^-$ and $\Lambda \to p\mu^-\bar{\nu}_\mu$ channels passing SignalLine for 2016, 2017 and 2018 with Magnet Up and Magnet Down configurations.

Taking that into account, the analysis strategy can be summarized in the following steps:

1. Add Common Cuts to MC and Data passing NormLine. The idea is to remove the $K^0_S \to \pi^+\pi^-$ component.

2. Fit $\Lambda \to p\pi^-$ from MinBias MC passing NormLine, selected with the TRUE ID [1], to obtain the tail parameters of the Lppi peak.
3. Fit TISTISTIS Data passing NormLine for each year and polarity, setting the tail parameters obtained in the TRUE ID MinBiasMC Fit. By doing this, we obtain the amount of $\Lambda \to p\pi^-$ in Data passing the Normalization StrippingLine ($N^{\text{NormLine}}_{\Lambda\to p\pi^-}$).
4. Obtain the efficiency for the $\Lambda \to p\pi^-$ passing NormLine ($\epsilon^{\text{NormLine}}_{\Lambda\to p\pi^-}$). This will be obtained by fitting the MinBiasMC passing NormLine setting the tail parameters extracted in point 2 to obtain the amount of $\Lambda \to p\pi^-$ in that sample and dividing this number by the total amount of $\Lambda \to p\pi^-$ in the MinBiasMC sample (before the reconstruction and the stripping).
5. The amount of $\Lambda \to p\pi^-$ in Data before the stripping ($N_{\Lambda\to p\pi^-}$) will be obtained dividing the output of step number 3, $N^{\text{NormLine}}_{\Lambda\to p\pi^-}$, by the output of step 4, $\epsilon^{\text{NormLine}}_{\Lambda\to p\pi^-}$.

$$N_{\Lambda\to p\pi^-} = \frac{N^{\text{NormLine}}_{\Lambda\to p\pi^-}}{\epsilon^{\text{NormLine}}_{\Lambda\to p\pi^-}} \tag{5.7}$$

6. Next step will be to perform a fit to measure the amount of Signal in TISTISTIS Data passing the SignalLine, $N^{\text{SignalLineSel}}_{\Lambda\to p\mu^-\bar{\nu}_\mu}$.
7. Using the $\Lambda \to p\mu^-\bar{\nu}_\mu$ stripping filtered MC production we can obtain the selection efficiency for signal, $\epsilon^{Sel}_{\Lambda\to p\mu^-\bar{\nu}_\mu}$. From the production logs we can also obtain the efficiency for the signal passing the SignalLine, $\epsilon^{\text{SignalLine}}_{\Lambda\to p\mu^-\bar{\nu}_\mu}$. The product of both efficiencies is $\epsilon^{\text{SignalLineSel}}_{\Lambda\to p\mu^-\bar{\nu}_\mu}$.
8. The efficiencies $\epsilon^{\text{SignalLine}}_{\Lambda\to p\mu^-\bar{\nu}_\mu}$ and $\epsilon^{\text{NormLine}}_{\Lambda\to p\pi^-}$ are corrected using PidCalib2 and TrackCalib2.
9. The final step, will be to obtain the $\mathcal{B}(\Lambda \to p\mu^-\bar{\nu}_\mu)$ appliyng the equation

$$\mathcal{B}(\Lambda \to p\mu^-\bar{\nu}_\mu) = N^{\text{SignalLineSel}}_{\Lambda\to p\mu^-\bar{\nu}_\mu} \frac{\mathcal{B}(\Lambda \to p\pi^-)}{N^{\text{NormLine}}_{\Lambda\to p\pi^-}} \frac{\epsilon^{\text{NormLine}}_{\Lambda\to p\pi^-}}{\epsilon^{\text{SignalLineSel}}_{\Lambda\to p\mu^-\bar{\nu}_\mu}} \tag{5.8}$$

Obviously, in the previous analysis description we will be taking into consideration also the charge conjugated modes.

Obviously, following the footnote 1 prescription, in the previous analysis description we will be taking into consideration also the charge conjugated modes.

A diagram of the Analysis workflow can be found in Fig. 5.1.

[1] The `TRUE ID` variable provides the ID of the particle responsible for producing a track, with the ID numbering following the PDG Monte Carlo numbering scheme [63]. This variable is exclusively defined in MC samples, where the true information of the event is accessible.

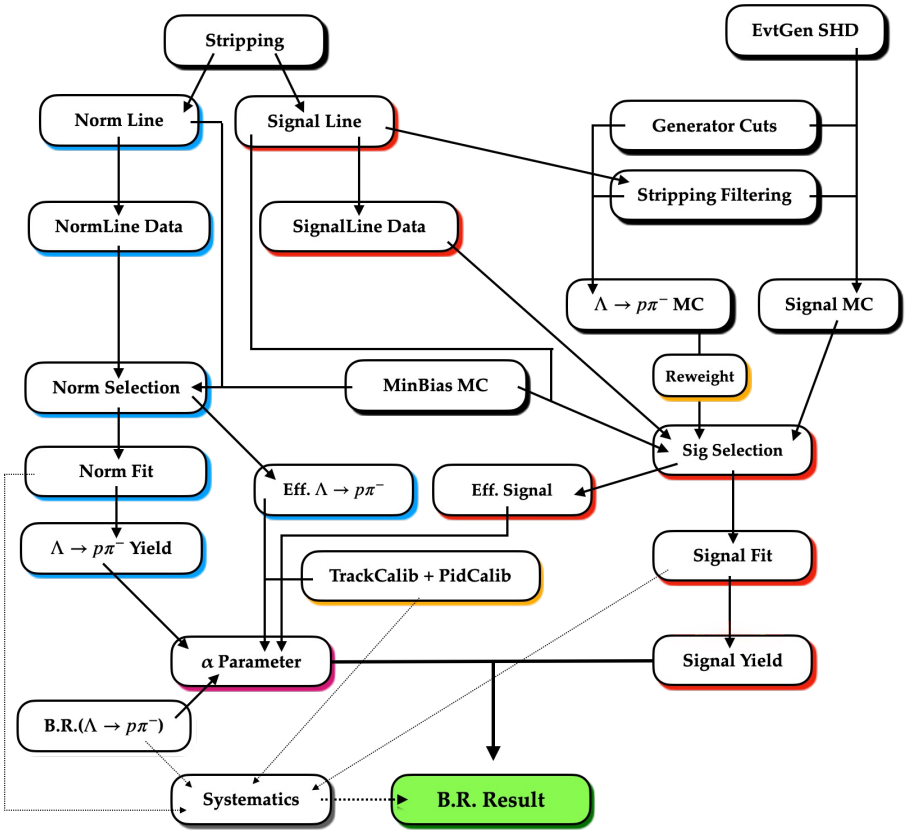

FIGURE 5.1: Analysis workflow. Blue color indicates processes related to normalisation and red ones to the signal measurement. Black color is associated to MC and yellow to MC corrections. Dotted lines show the systematic uncertainty sources.

5.2 STRIPPING LINES

Eventhough in LHCb an event is only recorded if it passes a Trigger Line, we have a huge amount of events in LHCb Data. As a consequence, specific stripping lines (offline selection) are written to reduce the amount of events, selecting only those that verify some cuts.

In general, a Stripping Line is designed to select a certain decay channel. In our case we designed two Stripping Lines, one to select the Signal ($\Lambda \rightarrow p\mu^-\bar{\nu}_\mu$) and the other to select the normalization channel ($\Lambda \rightarrow p\pi^-$).

From now on we will call the Stripping Line written aiming to select $\Lambda \rightarrow p\mu^-\bar{\nu}_\mu$ **SignalLine** and the Stripping Line written to select $\Lambda \rightarrow p\pi^-$ **NormLine**.

Both Trigger Line Cuts (see Tab. 5.1) are aligned to reduce the systematic errors associated to the $\Lambda \rightarrow p\mu^-\bar{\nu}_\mu$ branching fraction measurement as much as possible.

Notice the accidentally missing cut in the pion Impact Parameter. This cut will be added in NormLine Data after the stripping process to align both Stripping Lines.

TABLE 5.1: This table compares the cuts applied in the SignalLine and NormLine side-by-side for each category. Note that for the Daughter Cuts (Muon/Pion), the cuts are compared between the muon in the SignalLine and the pion in the NormLine.

Category	Variable	SignalLine Cut	NormLine Cut
Combination Cuts	DOCA [1] [mm]	< 0.3	< 0.3
	Mother Mass $[MeV/c^2]$	< 1141	< 1141
Mother Cuts	τ [ps]	> 9	> 9
	Mother Mass $[MeV/c^2]$	< 1141	< 1141
	V_{χ^2} [2]	< 9	< 9
	χ^2 distance to PV	> 50	> 50
	IP [3] [mm]	> 0.2	> 0.2
Proton Cuts	Proton ProbNN	> 0.3	> 0.3
	Muon ProbNN	< 0.7	< 0.7
	Kaon ProbNN	< 0.7	< 0.7
	Ghost ProbNN	< 0.2	< 0.2
	IP_{χ^2}	> 16	> 16
	Track χ^2/d.o.f.	< 3	< 3
Muon/Pion Cuts	Pion ProbNN	< 0.7	> 0.4
	Muon ProbNN	> 0.3	< 0.7
	Kaon ProbNN	< 0.7	< 0.7
	Ghost ProbNN	< 0.2	< 0.2
	ISMUON	TRUE	FALSE
	IP	> 1	$\times$ Missing
	IP_{χ^2}	> 60	> 60
	Track χ^2/d.o.f.	< 3	< 3

5.2.1 DEFINITION OF STRIPPING VARIABLES

5.2.1.1 PROBNN

This variables, used for particle identification, are derived from Neural Networks (NNs). To obtain these variables, data from various subdetectors are utilized, taking their correlations into account. The objective is to determine a value that correlates with the probability of each track being produced by a specific type of particle.

5.2.2 ISMUON

The process to spot muons begins by linking the hits in the muon detectors with each track. This involves extending the tracks in a straight line towards the detectors. An area called the Field of Interest (FoI) is then established around the projected spot. The size of this area varies based on the track's momentum, the specific muon chamber, and its location. Within these FoIs, the search for detections occurs, with the number of detectors involved depending on the track's momentum.

The nearest hits are selected for further consideration, and only tracks with these confirmed hits go on to the subsequent steps in the identification process. The initial outcome of this method is a simple yes-or-no indicator, known in the LHCb community as IsMuon which signifies the most elementary level of identifying a muon.

5.2.2.1 DOCA

The Distance Of Closest Approach (DOCA) of the two daughters. This represents the minimal length that separates two tracks.

5.2.2.2 IP

The impact parameter is the perpendicular distance between the trajectory of a particle and the vertex from which it originates or at which it decays.

5.2.2.3 IP$_{\chi^2}$

The impact parameter significance in units of χ^2.

5.2.2.4 χ^2 DISTANCE TO PV

This variable is related to the mother particle distance of flight, since includes the difference between the primary and secondary vertices.

[1] Distance Of Closest Approach.
[2] Vertex χ^2/d.o.f.
[3] Impact Parameter.

5.2.2.5 τ

Measured lifetime of the mother particle.

5.2.2.6 V_{χ^2}

The vertex χ^2 reflects the quality of fit for the estimated position of the decay vertex.

5.3 MC SAMPLES

To obtain the $\Lambda \to p\pi^-$ Monte Carlo (MC) sample passing the NormLine, which is necessary to fit the $\Lambda \to p\pi^-$ yield and compute $\epsilon^{\text{NormLine}}_{\Lambda\to p\pi^-}$, we utilize a **MinBias MC sample** for 2018 MU and MD conditions. The specific Stripping and DaVinci versions, along with tags and location details, can be found in the appendices (A.8.10).

Aiming for the signal yield fit, the first step involves generating a MC simulation to design the selection cuts, by comparing the properties of the signal MC with those of the background samples. Additionally, the MC simulation is necessary to determine the efficiency $\epsilon^{\text{SignalLine}}_{\Lambda\to p\mu^-\bar{\nu}_\mu}$.

The LHCb simulation consists of several steps. In our case, we are using Pythia 8 to generate the collision events and the DecFiles version v30r57, with a 33512008 EventType for Signal ($\Lambda \to p\mu^-\bar{\nu}_\mu$) and 33102103 for Background ($\Lambda \to p\pi^-$). This DecFile set some conditions for the generated particles, including a specific EvtGen model for the signal. Then, the analysis software used in each year for the MC processing was DaVinci v44r10p2 for 2018, v42r9p2 for 2017 and v44r10p5 for 2016.

Both for Signal, and Background the simulation production was a Stripping Filtered one. This means that in each event is generated at least one decay that passes the Signal Stripping Line. This is accomplished with a filtering script that ensures only events passing the SignalLine are saved to disk.

5.3.1 SIGNAL SIMULATION

5.3.1.1 SHD EVTGEN MODEL

A new EvtGen Model, that imposes the decay's theoretical kinematic distributions, is needed for this process.

The differential decay rate for Semileptonic Hyperon Decays (SHD) is given by

$$\frac{d\Gamma}{dq^2 d(cos\theta)} = \frac{G_F^2 f_1(0)^2 |V_{us}^2|}{(2\pi)^3}(q^2 - m_l^2)^2 \frac{q_3 \Delta^2}{16q^2}[I_1(q^2) + I_2(q^2)cos(\theta) + I_3(q^2)cos^2(\theta))] \tag{5.9}$$

where q^2 is the invariant mass squared of the dilepton pair, $f_1(0)$ the vector coupling, θ the angle between the neutrino 3-momentum and the recoiling baryon direction of fly (in the dilepton rest-frame), $\Delta = M_1 - M_2$, with $M_1(M_2)$ the parent (daughter) baryon mass, $\delta = \frac{M_1 - M_2}{M_1}$ and the angular coefficients of the 3-body decay being

$$I_1 e = \frac{4(1-\delta)}{q^2}((1 - \frac{q^2}{\Delta^2}) + (1 + \frac{q^2}{\Delta^2})(\frac{g_1(0)}{f_1(0)})^2), \quad I_1\mu = \frac{4m_l^2}{q^4}(1-\delta)(1 + (\frac{g_1(0)}{f_1(0)})^2) \tag{5.10}$$

$$I_2 e = \frac{8\delta}{\Delta^2}\sqrt{1 - \frac{q^2}{\Delta^2}}(1 + 2\frac{f_2(0)}{f_1(0))})\frac{g_1(0)}{f_1(0)}, \quad I_2\mu = -\frac{8m_l^2}{q^4}\sqrt{1 - \frac{q^2}{\Delta^2}}(1-\delta)(1 + (\frac{g_1(0)}{f_1(0)})^2) \tag{5.11}$$

$$I_3 e = -\frac{4(1-\delta)}{q^2}(1-\frac{q^2}{\Delta^2})(1+\frac{g_1(0)}{f_1(0)})^2), \quad I_3\mu = \frac{4m_l^2}{q^4}(1-\frac{q^2}{\Delta^2})(1-\delta)(1+(\frac{g_1(0)}{f_1(0)})^2) \tag{5.12}$$

where $g_1(0)$ and $f_2(0)$ are the axial-vector and weak-magnetic couplings, respectively. Hence, $I_i = I_i e + I_i \mu$ (with i=1,2,3). Finally, q_3 can be calculated by

$$q_3(M_1, M_2) = \frac{1}{2M_1}\sqrt{M_1^4 + M_2^4 + q^4 - 2(M_1^2 M_2^2 + q^2 M_1^2 + q^2 M_2^2)} \tag{5.13}$$

The inputs are obtained from data or systematically in a SU(3)-breaking expansion. More precisely: $f_1(0)$ is connected by SU(3) to the charges of proton and neutron and is protected from leading corrections by the Ademollo-Gatto theorem. $\frac{g_1(0)}{f_1(0)}$ is measured from the energy spectrum in the electronic modes and $f_2(0)$ is related by SU(3) with magnetic moments of proton and neutron (corrections enter at Δ^2 in the rate). The parameters values are extracted from [26] and can be found in Tab. 5.2:

TABLE 5.2: Coefficients values for the $\Lambda \to p\mu^- \bar{\nu}_\mu$ case. The form factors are valid independently of the lepton flavour on the final state.

Channel	$f_1(0)$	$\frac{g_1(0)}{f_1(0)}$	$\frac{f_2(0)}{f_1(0)}$
$\Lambda \to p$	$-\sqrt{\frac{3}{2}}$	0.718	1.066

We used a Decay Model Class called EvtGenProb that allows you to calculate a probability for the decay. This probability is then used in an accept-reject method [28].

The resulting EvtGen model is called **SHD** and it is written to be compatible with any Semileptonic Hyperon Decay. It takes as an input the maximum value of the differential rate, $g_1(0)/f_1(0)$ and $f_2(0)/f_1(0)$.

SHD model was tested, showing a good agreement between the output and the theoretical functions, as can be seen in Fig. 5.2.

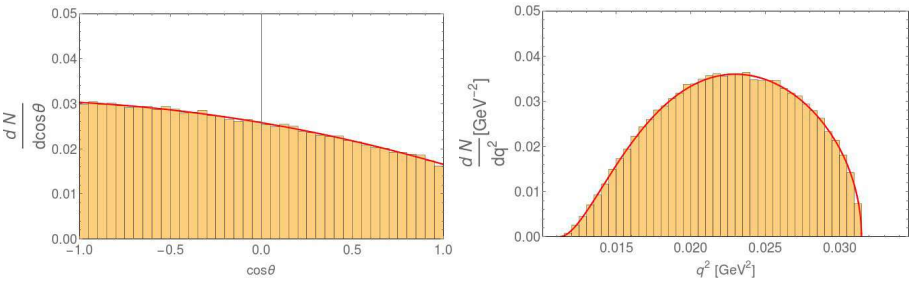

FIGURE 5.2: Some properties (q^2 and $cos(\theta)$ distributions) of the MC generated signal, showing an excellent agreement with the theoretical distributions (in red).

5.3.1.2 GENERATION

Events are generated with tight cuts at generator level applied on the decay vertex to force the Λ to decay inside the sensitive region of the LHCb Vertex Locator and also on the daughters tracks to be sure that both are within the LHCb acceptance.

Specifically, the Λ is forced to decay with a V_Z in the range of -1 to 0.8 meters and with $V_X^2 + V_Y^2 < 38\ mm^2$, being V the decay vertex. On the other hand, the daughters are forced to decay in the detector acceptance by imposing $-1.95 < \eta < 5.050$. Then we decay our Λ using the developed SHD model.

With an initial private simulation, that will be used later to correct the PID and tracking efficiencies, with 400K signal events generated, we obtained a generation efficiency of:

$$\epsilon^{GenPrivate}_{\Lambda\to p\mu^-\bar{\nu}_\mu} = 0.0808 \pm 0.0011$$

This efficiency was also obtained from the central LHCb production logs for each year and polarity (Tab. 5.3):

TABLE 5.3: $\epsilon^{\text{GenLHCb}}_{\Lambda\to p\mu^-\bar{\nu}_\mu}$ obtained from the central LHCb production for each year and polarity.

	Magnet Down	Magnet Up
$\epsilon^{\text{GenLHCb}}_{\Lambda\to p\mu^-\bar{\nu}_\mu}$ 2018	0.08151 ± 0.00017	0.08158 ± 0.00017
$\epsilon^{\text{GenLHCb}}_{\Lambda\to p\mu^-\bar{\nu}_\mu}$ 2017	0.08143 ± 0.00018	0.08141 ± 0.00017
$\epsilon^{\text{GenLHCb}}_{\Lambda\to p\mu^-\bar{\nu}_\mu}$ 2016	0.08144 ± 0.00018	0.08160 ± 0.00018

5.3.1.3 RECONSTRUCTION

In the private simulation case, the signal was reconstructed stopping at Brunel by using the following software versions: Boole/v30r3, Moore/v25r4 and Brunel/v50r4. A specific Leptonic trigger line was written for the signal, StrippingStrangeSLL02PMuNuLine (see previous section). Tags and locations can be found in the appendices (A.8).

Then, last step is to run the stripping line to the generated signal and use it as our DaVinci DecayTreeTuple input. The Stripping+Reco efficiency obtained is

$$\epsilon^{\text{RecStrPrivate}}_{\Lambda\to p\mu^-\bar{\nu}_\mu} = 0.004157 \pm 0.00011$$

On the other hand, we also have this same efficiency for each year and polarity obtained from the LHCb production. The results are shown in Tab. 5.4 and the methodology to obtain it is explained in the appendices (A.1.1).

TABLE 5.4: $\epsilon^{\text{RecStrLHCb}}_{\Lambda\to p\mu^-\bar{\nu}_\mu}$ obtained from the central LHCb production for each year and polarity.

	Magnet Down	Magnet Up
$\epsilon^{\text{RecStrLHCb}}_{\Lambda\to p\mu^-\bar{\nu}_\mu}$ 2018	0.004102 ± 0.000013	0.004108 ± 0.000013
$\epsilon^{\text{RecStrLHCb}}_{\Lambda\to p\mu^-\bar{\nu}_\mu}$ 2017	0.004129 ± 0.000013	0.004166 ± 0.000013
$\epsilon^{\text{RecStrLHCb}}_{\Lambda\to p\mu^-\bar{\nu}_\mu}$ 2016	0.004153 ± 0.000013	0.004131 ± 0.000013

The total signal efficiency for being reconstructed and passing the SignalLine will be the product of the Generation efficiency and the Stripping+Reconstruction Efficiency

$$\epsilon^{\text{SignalLine}}_{\Lambda\to p\mu^-\bar{\nu}_\mu} = \epsilon^{\text{GenLHCb}}_{\Lambda\to p\mu^-\bar{\nu}_\mu} \times \epsilon^{\text{RecStrLHCb}}_{\Lambda\to p\mu^-\bar{\nu}_\mu} \tag{5.14}$$

The final Signal efficiency results ($\epsilon^{\text{SignalLine}}_{\Lambda\to p\mu^-\bar{\nu}_\mu}$) are shown in Tab. 5.5.

TABLE 5.5: $\epsilon^{\text{SignalLine}}_{\Lambda\to p\mu^-\bar{\nu}_\mu}$ obtained from the central LHCb production for each year and polarity.

	Magnet Down	Magnet Up
$\epsilon^{\text{SignalLine}}_{\Lambda\to p\mu^-\bar{\nu}_\mu}$ 2018	$(3.343 \pm 0.013) \times 10^{-4}$	$(3.351 \pm 0.013) \times 10^{-4}$
$\epsilon^{\text{SignalLine}}_{\Lambda\to p\mu^-\bar{\nu}_\mu}$ 2017	$(3.362 \pm 0.013) \times 10^{-4}$	$(3.392 \pm 0.013) \times 10^{-4}$
$\epsilon^{\text{SignalLine}}_{\Lambda\to p\mu^-\bar{\nu}_\mu}$ 2016	$(3.382 \pm 0.013) \times 10^{-4}$	$(3.371 \pm 0.013) \times 10^{-4}$

5.3.2 BACKGROUND SIMULATION

We will also need a Background MC in order to understand the background behaviour and to design selection cuts.

The main background will be $\Lambda \to p\pi^-$ and a specific DecFile (33102103) was created to set some kinematic properties aiming to increase its very low SignalLine retention rate. In this case the used EvtGen model was the default, PHSP (Phase Space). Tags and locations can be found in the appendices (A.8).

5.3.2.1 GENERATION

The Λ is forced to decay with a V_Z in the range of -1 to 0.8 meters and with $V_X^2+V_Y^2 < 38$ mm^2, being V the decay vertex. On the other hand, the daughters are forced to decay in the detector acceptance by imposing $-1.95 < \eta < 5.050$.

In addition we impose some momentum requirements for the proton and the pion. For the pion $P_Z > 0$, $P_T > 100$ MeV/c and $P > 3$ GeV/c and for the proton $P_T > 275$ MeV/c and $P > 12.25$ GeV/c.

These kinematic requirementes were designed after studyng the momentum distribution of the MinBias MC $\Lambda \rightarrow p\pi^-$ decays that pass the Signal Stripping Line and should not bias the generated Background MC, since all those MinBias events satisfy the momentum cuts imposed by the DecFile.

The $\Lambda \rightarrow p\pi^-$ Stripping Filtered Production Generation Efficiency for each year and polarity can be found in Tab. 5.6.

TABLE 5.6: $\epsilon^{\text{GenLHCb}}_{\Lambda\rightarrow p\pi^-}$ obtained from the central LHCb production for each year and polarity.

	Magnet Down	Magnet Up
$\epsilon^{\text{GenLHCb}}_{\Lambda\rightarrow p\pi^-}$ 2018	$(9.204 \pm 0.021) \times 10^{-3}$	$(9.200 \pm 0.021) \times 10^{-3}$
$\epsilon^{\text{GenLHCb}}_{\Lambda\rightarrow p\pi^-}$ 2017	$(9.223 \pm 0.021) \times 10^{-3}$	$(9.209 \pm 0.021) \times 10^{-3}$
$\epsilon^{\text{GenLHCb}}_{\Lambda\rightarrow p\pi^-}$ 2016	$(9.253 \pm 0.021) \times 10^{-3}$	$(9.199 \pm 0.021) \times 10^{-3}$

5.3.2.2 RECONSTRUCTION

The $\Lambda \rightarrow p\pi^-$ Stripping Filtered Production Reconstruction Efficiency for each year and polarity can be found in Tab. 5.7 and the methodology to obtain it is explained in the appendices (A.1.2).

Using Eq. 5.14, multiplying numbers of Tab. 5.6 and Tab. 5.7, we can obtain the total efficiency for $\Lambda \rightarrow p\pi^-$ passing the Signal Line Stripping Line. This efficiency can be used to know the amount of $\Lambda \rightarrow p\pi^-$ in the Data passing SignalLine, once we measure the amount of $\Lambda \rightarrow p\pi^-$ in Data in the NormLine and, consequently, the amount of $\Lambda \rightarrow p\pi^-$ before the Stripping process.

The efficiencies can be compared with the efficiency obtained from the MinBias sample.

TABLE 5.7: $\epsilon^{\text{RecStrLHCb}}_{\Lambda\to p\pi^-}$ obtained from the central LHCb production for each year and polarity.

	Magnet Down	Magnet Up
$\epsilon^{\text{RecStrLHCb}}_{\Lambda\to p\pi^-}$ 2018	$(1.489 \pm 0.043) \times 10^{-4}$	$(1.431 \pm 0.042) \times 10^{-4}$
$\epsilon^{\text{RecStrLHCb}}_{\Lambda\to p\pi^-}$ 2017	$(1.562 \pm 0.044) \times 10^{-4}$	$(1.449 \pm 0.042) \times 10^{-4}$
$\epsilon^{\text{RecStrLHCb}}_{\Lambda\to p\pi^-}$ 2016	$(1.466 \pm 0.031) \times 10^{-4}$	$(1.499 \pm 0.032) \times 10^{-4}$

TABLE 5.8: $\epsilon^{\text{SignalLine}}_{\Lambda\to p\pi^-}$ obtained from the central LHCb production for each year and polarity.

	Magnet Down	Magnet Up
$\epsilon^{\text{SignalLine}}_{\Lambda\to p\pi^-}$ 2018	$(9.30 \pm 0.33) \times 10^{-7}$	$(8.66 \pm 0.32) \times 10^{-7}$
$\epsilon^{\text{SignalLine}}_{\Lambda\to p\pi^-}$ 2017	$(9.53 \pm 0.33) \times 10^{-7}$	$(8.86 \pm 0.32) \times 10^{-7}$
$\epsilon^{\text{SignalLine}}_{\Lambda\to p\pi^-}$ 2016	$(8.88 \pm 0.23) \times 10^{-7}$	$(9.00 \pm 0.23) \times 10^{-7}$

5.4 BACKGROUND SOURCES

Having the MinBias MC passing the SignalLine sample provides us with an overview of what we can expect to observe in the Data.

Although the average contribution of each decay in the MC may not be entirely reliable, studying it serves as a helpful exercise and can provide a rough estimate. For instance, it is crucial to note that even having a SignalLine with tight cuts designed to select $\Lambda \longrightarrow p\mu^-\bar{\nu}_\mu$, the signal purity in this MinBias MC sample is only 3.48 %.

Therefore, it is necessary to analyze the composition of the MinBias MC sample that passes the SignalLine. This analysis was conducted by applying the correspondent truth-matching conditions for each channel, that are detailed in the appendices A.3. Results can be found in Tab 5.9. An additional check was performed to ensure the absence of peaking backgrounds by replacing the mass hypothesis for the combinatorial background events (see Appendix A.6)

TABLE 5.9: Average contribution of each decay channel to the MinBias MC sample after the Stripping process in SignalLine. In the non-obvious cases, reconstructed particles are written in bold symbols. A study of the average contribution after applying tighter PID cuts was performed, and the results can be seen in Appendix A.5.

Decay	Contribution
$\Lambda \longrightarrow p\pi^-$	(42.7 ± 1.5) %
Combinatorial Background and Others	(35.4 ± 1.4) %
$\Lambda \longrightarrow p(\pi^- \longrightarrow \mu^-\bar{\nu}_\mu)$	(14.7 ± 1.1) %
$\Lambda \longrightarrow p\mu^-\bar{\nu}_\mu$	(3.48 ± 0.56) %
$K^0_S \longrightarrow \pi^+\pi^-$	(2.20 ± 0.44) %
$\Xi^- \longrightarrow (\Lambda \longrightarrow \boldsymbol{p}\pi^-)\boldsymbol{\pi^+}$	(1.28 ± 0.34) %
$\Xi^- \longrightarrow (\Lambda \longrightarrow \boldsymbol{p}\pi^-)(\pi^+ \longrightarrow \boldsymbol{\mu}\bar{\nu}_\mu)$	(0.275 ± 0.16) %

Taking this results into account is obvious that Misidentified $\Lambda \longrightarrow p\pi^-$ and early Decays In Flight (eDIF) are the main backgrounds in this analysis, with a total expected contribution close to 60 % of the SignalLine sample.

The early decays in flight (Fig. 5.3), with the pion decaying early to a muon and a neutrino, may be really hard to separate from signal, since we have the same final state in both channels with almost indistinguishable kinematic properties.

The good news is that we have a dedicated LHCb production to simulate $\Lambda \longrightarrow p\pi^-$ passing SignalLine, which will be crucial to understand how to select the signal and how to discriminate these background sources.

On the other hand, $K^0_S \longrightarrow \pi^+\pi^-$ is an easier background to kill, since we can design a specific cut in the Armenteros-Podolanski plot to kill most of the $K^0_S \longrightarrow \pi^+\pi^-$ preserving almost all the signal.

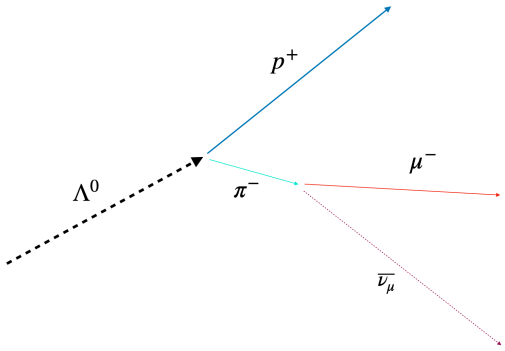

FIGURE 5.3: A representation of an early decay in flight (eDIF).

5.4.1 MISIDENTIFIED $\Lambda \longrightarrow p\pi^-$

This decay, with a pion misidentified as muon, is the main background contribution to the MinBias MC SignalLine sample. Even though having created the SignalLine stripping line specifically to reduce this contribution, the difference in the branching ratios of $\Lambda \longrightarrow p\pi^-$ and $\Lambda \longrightarrow p\mu^-\bar{\nu}_\mu$ is so large that we still are dominated by $\Lambda \longrightarrow p\pi^-$.

Despite that, it should be relatevely easy to design some selection cuts to remove most of MisID $\Lambda \longrightarrow p\pi^-$. The Armenteros-Podolanski plot [66] should also be a good plane to impose selection requirements [42].

The Armenteros-Podolanski plot has as Y-axis the QPT variable, the transverse momentum of any of the daughters with respect to the mother direction of flight (in a 2-body decay both must be equal) and as X-axis the longitudinal momentum asymmetry,

$$\alpha = \frac{p_L^+ - p_L^-}{p_L^+ + p_L^-} \tag{5.15}$$

where p_L^+ and p_L^- are $p^+cos(\theta_1)$ and $p^-cos(\theta_2)$ respectively, supposing that the particle 1 is the positive in Fig. 5.4. The mother direction of flight can be obtained from the primary and second vertex positions.

Signal and $\Lambda \longrightarrow p\pi^-$ MC behaviour in the Armenteros-Podolanski plot can be found in Fig. 5.5.

In *Prospects for measurements with strange hadrons at LHCb* [10] another two dimensional plane was suggested to separate $\Lambda \longrightarrow p\pi^-$ and $\Lambda \longrightarrow p\mu^-\bar{\nu}_\mu$. This two dimensional plane has as x-axis the missing transverse momentum in the plane that is perpendicular to the the mother particle direction of fly ($\not{p}_T$ [2]), and as y-axis the $M(p\mu)$ (reconstructed mass with the proton-muon hypothesis). Fig. 5.6 shows the full-simulated behaviour in the plane.

[2]This variable represents the missing transverse momentum in the plane that is perpendicular to the the mother particle direction of fly, calculated using reconstructed information. For a more detailed explanation, see subsection 5.5.1.1.

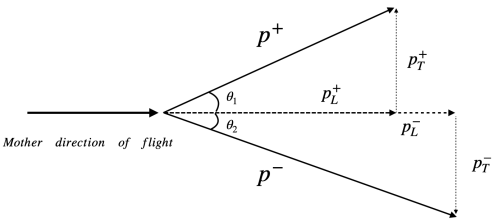

FIGURE 5.4: 2-Body decay scheme in the laboratory frame of reference.

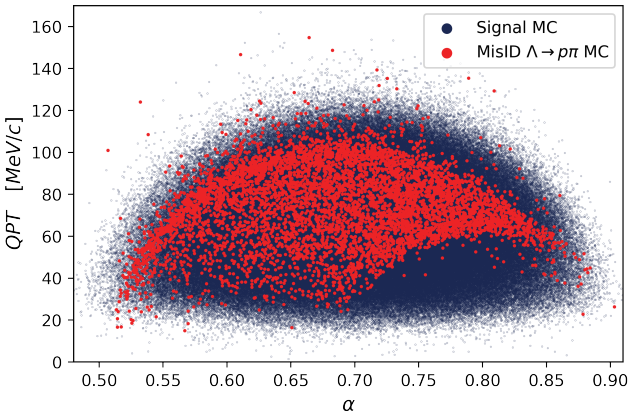

FIGURE 5.5: Armenteros-Podolanski plot for SignalMC and $\Lambda \rightarrow p\pi^-$ MC passing SignalLine.

Some conclusions can be extracted from Fig. 5.5 and Fig. 5.6. For example, if we compare the $\Lambda \rightarrow p\pi^-$ MC passing the SignalLine behaviour in the Armenteros-Podolanki plot with a typical $\Lambda \rightarrow p\pi^-$ dominated Armenteros-Podolanki plot, as the one in Fig. 5.7, we find relevant differences.

For example, in Fig. 5.5, even having the usual $\Lambda \rightarrow p\pi^-$ ellipse visible, the misidentified $\Lambda \rightarrow p\pi^-$ passing NormLine presents a highly populated region under the ellipse. This is because if the pion decays to a muon and a neutrino far enough from the primary vertex it will be reconstructed as pion, but the reconstructed particle will have less momentum than the original pion, since the missing momentum is carried by the neutrino.

On another hand, it draws attention an empty space under an ellipse centered in $\alpha \approx 0.82$ with its maximum QPT value in QPT $\approx 60\ MeV/c$. An ellipse in the Armenteros-Podolanksi plot is equivalent to a specific mother mass. Taking this into account, the fact of not having misidentified $\Lambda \rightarrow p\pi^-$ decays falling below this

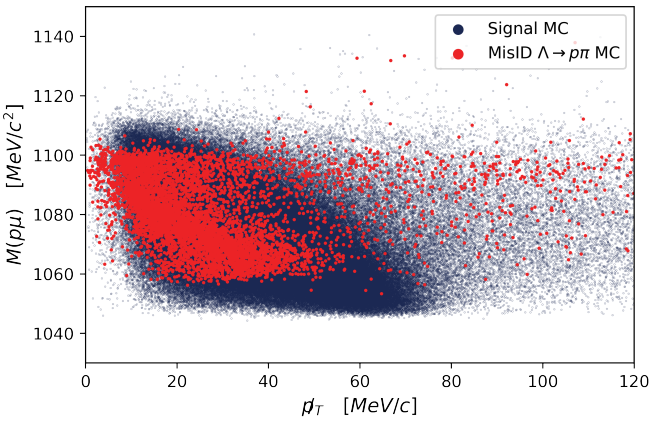

FIGURE 5.6: Missing momentum in the plane transverse to the Λ flight direction ($\not{p}_T$) vs. reconstructed mass M($p\mu$) for $\Lambda \longrightarrow p\mu^- \bar{\nu}_\mu$ in blue and misidentified $\Lambda \longrightarrow p\pi^-$ in red.

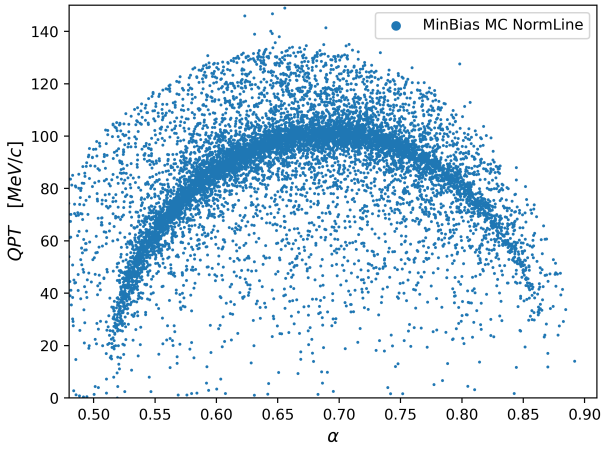

FIGURE 5.7: Armenteros-Podolanski plot of a 10000 entries subsample of the MinBiasMC passing NormLine, where the $\Lambda \longrightarrow p\pi^-$ ellipse is remarkable.

elipse indicates that there is a minimum mass that can be reconstructed with a proton and muon, where the muon comes from an original pion from the $\Lambda \longrightarrow p\pi^-$ decay. It is also remarkable that this does not happen in the $\Lambda \longrightarrow p\mu^- \bar{\nu}_\mu$ case.

If this explanation is true, we should see the effect in the M(pμ) distribution of the $\Lambda \longrightarrow p\pi^-$ passing SignalLine. The resultant normalised histograms are in Fig. 5.8, verifying our deduction.

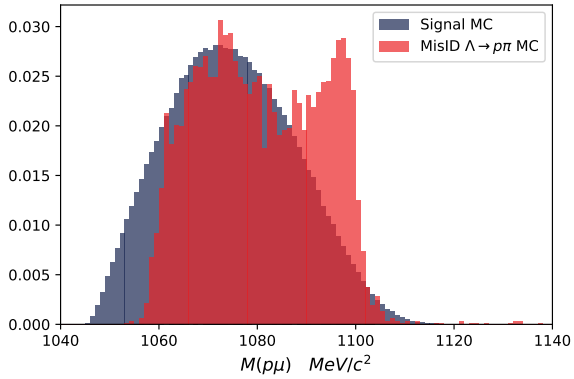

FIGURE 5.8: Norm. M(pμ) distribution of $\Lambda \longrightarrow p\mu^- \bar{\nu}_\mu$ in blue and MisID $\Lambda \longrightarrow p\pi^-$ in red.

As a cross-check, Fig. 5.9 displays those events with low $M(p, \mu)$, serving as a repetition of Fig. 5.5 and confirming the interpretation.

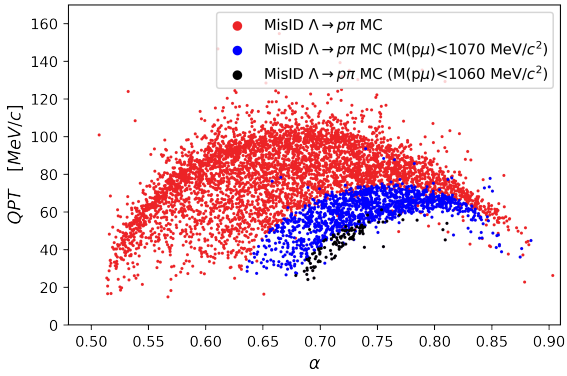

FIGURE 5.9: Armenteros-Podolanski plot for $\Lambda \longrightarrow p\pi^-$ MC passing SignalLine, showing in blue those events with $M(p, \mu) < 1070$ Mev/c^2 and in black those with $M(p, \mu) < 1060$ Mev/c^2.

Concerning the $\not{p}_T$ vs. M($p\mu$) plane (Fig. 5.5), we can also extract some conclusions from the 2-dimensional distributions. For example the higher minimum mass in the $\Lambda \longrightarrow p\pi^-$ is evident here. But there is also a different correlation between the $\not{p}_T$ and the M($p\mu$) in both cases. This would allow for a possible selection cut in this plane to select a region with high signal purity.

5.4.2 EARLY DECAYS IN FLIGHT ($\Lambda \longrightarrow p(\pi^- \longrightarrow \mu^- \bar{\nu}_\mu)$)

If in a $\Lambda \longrightarrow p\pi^-$ decay the pion decays to a muon and a neutrino close enough to the secondary vertex, more than the 70 % of the track hits will be from the muon, and the track will be correctly matched to a muon. This category present some characteristic features, making it harder to distinguish from the signal.

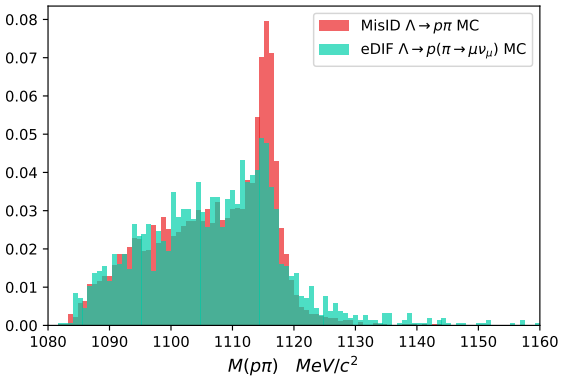

FIGURE 5.10: Normalised M(pπ) distribution of eDIF in green and MisID $\Lambda \longrightarrow p\pi^-$ in red.

For instance, the eDIF category M(pπ) distribution does not peak clearly in the Λ mass, whereas the MisID $\Lambda \longrightarrow p\pi^-$ presents a narrow peak centered in the Λ mass (see Fig. 5.10).

As we can see in Fig. 5.11, the z-component of the muon origin vertex has a maximum value around 650 mm in the MisID $\Lambda \longrightarrow p\pi^-$, whereas the eDIF category presents higher z-values for the muon origin vertices. So if the pion decays to a muon after this maximum value, which implies few VELO hits, it will never be reconstructed as a pion.

Being the$\Lambda \longrightarrow p(\pi^- \longrightarrow \mu^- \bar{\nu}_\mu)$ decays the hardest to separate from signal, having the same final state and similar kinematic properties, we have designed some variables that will help in this task. Those variables are presented in Section 5.5.1.

5.4.3 $K_S^0 \longrightarrow \pi^+\pi^-$

Another problematic background source is $K_S^0 \longrightarrow \pi^+\pi^-$ with one pion misidentified as a proton an the other as muon or decaying in flight to a muon and a neutrino. This is the only peaking background anticipated to contribute to SignalLine events, excluding $\Lambda \longrightarrow p\pi^-$. Having multiple peaking modes complicates the fitting of the signal yield. Hence, it's crucial to eliminate it. Additionally, this decay channel also contaminates the Normalization sample.

Even being a channel very different from signal, the $K_S^0 \longrightarrow \pi^+\pi^-$ production yield is so high in LHCb that its contribution to the SignalLine is relevant (see Tab. 5.9).

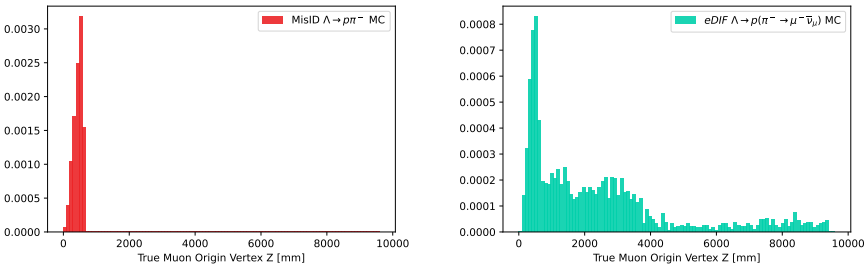

FIGURE 5.11: Normalised distribution of the true origin vertex z-component for the particle reconstructed as a muon for MisID $\Lambda \rightarrow p\pi^-$ (left) and for eDIF (right). Notice that the Origin Vertex Z refers to a different vertex for each channel. In the MisID $\Lambda \rightarrow p\pi^-$ case, where the particle reconstructed as a muon is actually a pion, its true origin vertex is the Λ decay vertex, whereas in the eDIF case, the true muon origin vertex is the pion decay vertex.

The good news are that the $K^0_S \rightarrow \pi^+\pi^-$ falls inside a specific region in the Armenteros-Podolanksi plot. In general, $K^0_S \rightarrow \pi^+\pi^-$ decays should correspond to a narrow elipse in this plane. See for example Fig. 5.12, where we are selecting $K^0_S \rightarrow \pi^+\pi^-$ from the MinBias MC sample passing NormLine and the $K^0_S \rightarrow \pi^+\pi^-$ ellipse is clearly visible.

On the other hand, the $K^0_S \rightarrow \pi^+\pi^-$ MC in the SignalLine is also, as it happens with the $\Lambda \rightarrow p\pi^-$ channel, blurred around the usual $K^0_S \rightarrow \pi^+\pi^-$ ellipse, because of the missing momentum when the pion decays to a muon and a neutrino. The correspondent Armenteros-Podolanksi plot is depicted in Fig. 5.13.

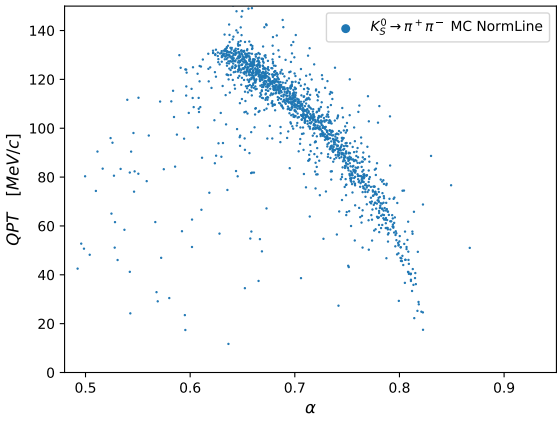

FIGURE 5.12: Armenteros-Podolanski plot for $K^0_S \rightarrow \pi^+\pi^-$ from the MinBias MC sample passing NormLine, where the typical $K^0_S \rightarrow \pi^+\pi^-$ ellipse is remarkable.

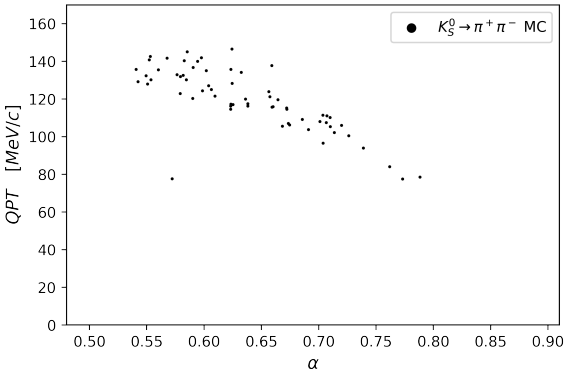

FIGURE 5.13: Armenteros-Podolanski plot for $K^0_S \to \pi^+\pi^-$ MC passing SignalLine.

Even being less concentrated around the usual $K^0_S \to \pi^+\pi^-$ ellipse, it is easy to create a selection cut to remove this background. This will be explained in detail in the Selection section 5.5.

5.5 SELECTION AND NEW VARIABLES

5.5.1 VARIABLES

Having background sources almost identical to our signal, the development of new variables was mandatory to be able to separate both. The idea is to use the kinematic properties of each decay channel to design specific variables that allow us to distinguish that channel. Being the $\Lambda \rightarrow p\mu^-\bar{\nu}_\mu$ case the most problematic for us, we started by separating those decays into two categories. If the pion decays early enough, we will have a muon in the vertex locator. If the pion decays into a muon and a neutrino after passing the VELO, then we will observe a pion at the VELO level. Those two categories and the strategies to recover the missing information are detailed in Fig. 5.14. It is important to note that these new variables are only computed for the SignalLine events, as they are not required for the normalization process.

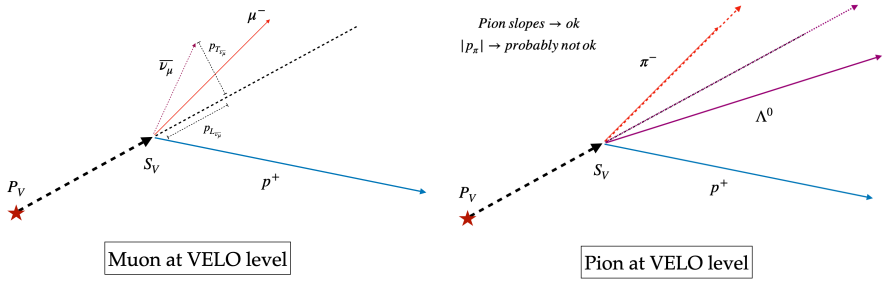

FIGURE 5.14: In the muon at VELO level case, the neutrino P_T can be obtained from proton and muon momentum components and the neutrino P_L by impossing Λ mass. In the pion at VELO level case, if the measured $|\vec{p}_\pi|$ is not the correct one, Λ will not point to the primary vertex. Imposing Λ to point to PV allows to solve for $|\vec{p}_\pi|$.

5.5.1.1 MISSING PERPENDICULAR MOMENTUM ($\not{p}_T$)

In the muon at VELO level, when the pion decays to a muon and a neutrino within the Vertex Locator, the neutrino P_T can be obtained from proton and muon momentum components.

This can be done using the Λ flight direction $\overrightarrow{(SV - PV)}$ and using the Gram-Schmidt idea [70] to find two orthogonal vectors to that flight direction. First we should obtain the flight direction vector $(\vec{f})$ using the Primary Vertex and the Λ Decay Vertex, and then compute the correspondent unit vector, dividing each component by $|\vec{f}|$.

If the mother flight direction unit vector is called $\hat{f}$, the first perpendicular unit vector will be obtained by constructing a vector $x_u = (-\hat{f}_y, -\hat{f}_x, 0)$ and then obtaining a correspondent unit vector $\hat{x_u}$. Finally, the second unit perpendicular momentum will be the cross product $\hat{y_u} = \hat{f} \times \hat{x_u}$.

Having this orthogonal base allows us for obtain the missing perpendicular momentum in the mother flight direction. For example, we can add the two daughters momentum to obtain the $\overrightarrow{p_{p\mu}}$ and then project its components to the new base:

$$\overrightarrow{p_{p\mu}}' = (\overrightarrow{p_{p\mu}}.\hat{x_u}, \overrightarrow{p_{p\mu}}.\hat{y_u}, \overrightarrow{p_{p\mu}}.\hat{f}) = (p'_{p\mu_x}, p'_{p\mu_y}, p'_{p\mu_z}) \tag{5.16}$$

Taking this into account, the missing perpendicular momentum in the mother flight direction will be

$$\not{p}_T = \sqrt{p'^2_{p\mu_x} + p'^2_{p\mu_y}} \tag{5.17}$$

5.5.1.2 LONGITUDINAL NEUTRINO MOMENTUM ($\not{p}_T$)

In the muon at VELO level case, the neutrino P_T can be obtained from proton and muon momentum components and the neutrino P_L by impossing Λ mass.

We can start by obtaining the perpendicular components of the neutrino momentum as it was explained in previous subsection. After that there will be only one piece missing, the longitudinal component of the neutrino momentum, that can be obtained imposing the Λ mass.

$$M^2_\Lambda = (E_{p\mu} + E_\nu)^2 - |\overrightarrow{p_{p\mu}} + \overrightarrow{p_\nu}|^2 = M^2_{p\mu} + 0 + 2.(E_{p\mu}.E_\nu - \overrightarrow{p_{p\mu}}.\overrightarrow{p_\nu}) \tag{5.18}$$

where

$$E_{p\mu} = \sqrt{M^2_{p\mu} + |\overrightarrow{p_{p\mu}}'|^2} \tag{5.19}$$

and

$$E_\nu = \sqrt{\not{p}^2_T + p_L(\nu_\mu)^2} \tag{5.20}$$

Taking into account that

$$\overrightarrow{p_{p\mu}}.\overrightarrow{p_\nu} = -\not{p}^2_T + p'_{p\mu_z}.p_L(\nu_\mu) \tag{5.21}$$

we finally obtain the expression to compute the $p_L(\nu_\mu)$:

$$p_L(\nu_\mu) = \frac{E_{p\mu}.\sqrt{A^2 - 2A.\not{p}^2_T + \not{p}^2_T.p'^2_{p\mu_z} + \not{p}^4_T - \not{p}^2_T.E^2_{p\mu}} - A.p'_{p\mu_z} + p'_{p\mu_z}.\not{p}^2_T}{(p'_{p\mu_z})^2 - E^2_{p\mu}} \tag{5.22}$$

where

$$A = \frac{M^2_\Lambda - M^2_{p\mu}}{2} \tag{5.23}$$

5.5.1.3 MCORR($p\pi$)

In the pion at VELO level, when the pion decays to a muon and a neutrino after the Vertex Locator (or after having enough hits on it), if the measured $|p_\pi|$ is not the correct one, Λ will not point to the primary vertex. Imposing Λ to point to PV allows to solve for $|p_\pi|$. If it is a $\Lambda \rightarrow p\mu^-\bar{\nu}_\mu$ decay, the recomputed M(p,π) using the obtained value of $|p_\pi|$ will peak at PDG mass. This new variable will be called from now on **MCorr(pπ)**.

The procedure to compute it unfolds as follows. Initially, we define a function based on a correction parameter that multiplies the pion momentum. Subsequently, the Λ momentum is derived by summing the corrected pion momentum with the proton's momentum and its unit vector, $\hat{p}_\Lambda$, is determined. The function returns 1 - $\hat{p}_\Lambda.\hat{f}$, where $\hat{f}$ represents the unit vector of the mother particle's flight direction, as described earlier. We employ Minuit to minimize the function's output, which determines of the optimal correction value. This value subsequently corrects the pion momentum, and **MCorr(pπ)** is computed using it and the proton one, with the proton-pion mass hypothesis. The code can be found in the appendices, Sec. A.7.

This strategy was designed to correct the pion momentum in the "pion at Velo" scenario (see Fig. 5.14). However, it's crucial to recognize that we cannot ascertain whether we have a muon or a pion at the vertex locator level in our Data. Regardless, this strategy can be applied to every event in the SignalLine sample, resulting varied results. For instance, for our signal, a significant proportion of events require no correction **MCorr(pπ)** = **M(pπ)**, and $\Lambda \rightarrow p\mu^-\bar{\nu}_\mu$ events should peak at the Λ mass for this variable. This is, in fact, the case for a large amount of data events (see Fig. 5.15).

We can also attempt to compute the longitudinal neutrino momentum for events with a pion at the VELO, utilizing Eq. 5.22. It is worth noting, however, that for the $\Lambda \rightarrow p\pi^-$ channels, there isn't a neutrino present. Moreover, when we have access to the TRUE information, we invariably find $p_L(\nu_\mu) = 0$. A more detailed explanation is provided in subsection 5.5.2.

However, as previously mentioned, we lack prior knowledge about which particle is present at the vertex locator level in our data. Consequently, both strategies are applied to the entire SignalLine sample.

In addition, two other variables were designed for applying checks, even though they are not used in the selection:

5.5.1.4 MCORR(π)

In the muon at VELO level, when the pion decays to a muon and a neutrino within the Vertex Locator, the neutrino P_T can be obtained from proton and muon momentum components and the neutrino P_L by impossing Λ mass. So we can recover the neutrino momentum components and recompute the invariant pion mass before the decay in flight. If it peaks at the right pion mass we will recognize this category. This new variable will be called from now on **MCorr(π)**.

5.5.1.5 PLANARITY (APLA)

The planarity measures how close are two reconstructed particles to live in the same plane than its mother particle and it is calculated using

$$APLA = \overrightarrow{(SV - PV)}.(\vec{p}_{\text{daughter1}} \times \vec{p}_{\text{daughter2}}) \tag{5.24}$$

5.5.2 SIGNAL SELECTION

This subsection is based on the analysis of the MC and data passing through the SignalLine stripping line. As explained in the Simulation section, we generated two stripping filtered MC samples. In the first one we generate $\Lambda \rightarrow p\mu^-\bar{\nu}_\mu$ and in the other $\Lambda \rightarrow p\pi^-$. We also have available a MinBias MC sample with enough statistics passing SignalLine, that we can use to extract Combinatorial Background properties, among others.

5.5.2.1 SELECTING $p_L(\nu_\mu) > 0$

One of the variables explained in the previous subsection is $p_L(\nu_\mu)$. We can compute this variable for $\Lambda \rightarrow p\mu^-\bar{\nu}_\mu$ and $\Lambda \rightarrow p\pi^-$ MC, but we have to take into account that this variable contains a square root in its definitions. If we use true information, the values inside the square root argument in Eq. 5.22 will always be positive for $\Lambda \rightarrow p\mu^-\bar{\nu}_\mu$ MC. However, when using reconstructed momentum and vertex values, it is possible to have negative values inside the square root.

We will assign $p_L(\nu_\mu)$ = -999 when the root argument is negative. Applying a cut that selects only events with a positive value in the root argument is really tight and results in the removal of a significant amount of Combinatorial Background. This effect can be observed in the figures Fig. 5.15 and Fig. 5.16.

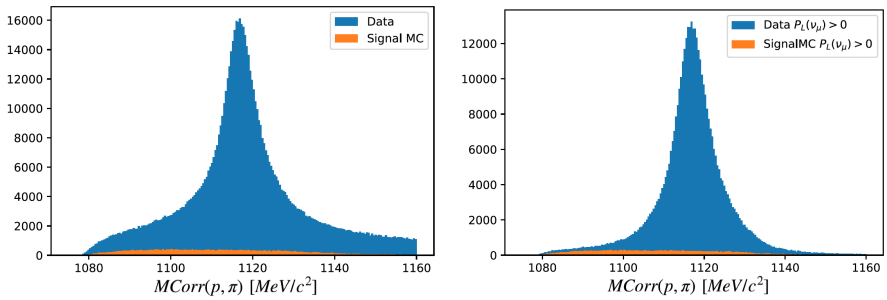

FIGURE 5.15: MCorr(pπ) behaviour of Data and expected signal contribution (left) and MCorr(pπ) behaviour of Data and expected signal after applying the $p_L(\nu_\mu) > 0$ requirement (right). After this selection we see that the signal purity increases sensitively and data is basically composed by a background clean peak and our signal.

The $MCorr(p\pi)$ vs $M(p\pi)$ plane is highly useful for distinguishing different component contributions to the data. The horizontal band corresponding to the Λ mass

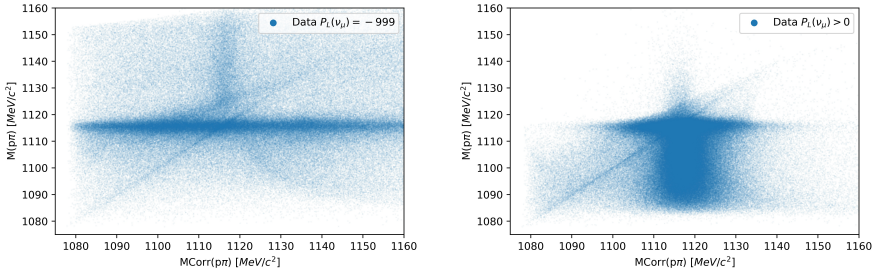

FIGURE 5.16: $MCorr(p\pi)$ vs $M(p\pi)$ scatter plot for Data with negative $P_L(\nu_\mu)$ root argument (left) and positive root argument (right.)

value will primarily consist of $\Lambda \rightarrow p\pi^-$ decays, while the vertical band matching the Λ mass value will mainly be populated by early decays in flight ($\Lambda \rightarrow p(\pi^- \rightarrow \mu^- \bar{\nu}_\mu)$).

Regarding the Signal, it will primarily be distributed in the Fig. 5.16 plane below the mentioned horizontal line (populated mainly by $\Lambda \rightarrow p\pi^-$) and to the left of the vertical line (where early decays in flight are concentrated). It is also worth noting that some of the signal events fall on the diagonal line $MCorr(p\pi) = M(p\pi)$, as illustrated in Figure 5.17.

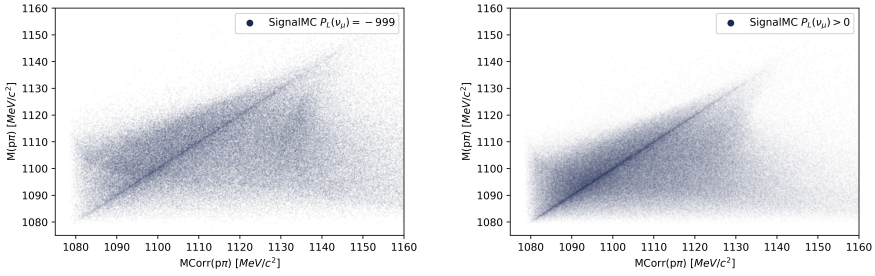

FIGURE 5.17: $MCorr(p\pi)$ vs $M(p\pi)$ scatter plot for Signal MC with negative $P_L(\nu_\mu)$ root argument (left) and positive root argument (right.)

Something great about applying a $P_L(\nu_\mu) > 0$ cut is that it cleans most of the combinatorial background. For example, we can check the $M(p\mu)$ variable after and before applying the cut. The result can be found in Figure 5.18.

If we explore further into the physical significance of selecting only events with a positive value inside the root in the expression for $P_L(\nu_\mu)$, it implies a requirement in the $\not{p}_T$ vs $M(p\mu)$ plane (Figure 5.19). As mentioned earlier, all Signal MC events should have $P_L(\nu_\mu) > 0$ at truth level, but reconstruction effects can cause cause a fraction of the Signal MC events to not meet the $P_L(\nu_\mu) > 0$ selection requirement (see Tab. 5.10).

This simple selection cut also effectively eliminates material interactions. By examining Figure 5.20, we can observe that in the left plot, material interactions

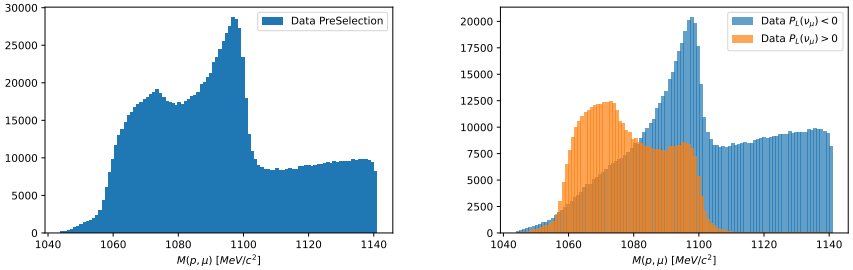

FIGURE 5.18: $M(p\mu)$ data distribution before any selection (left) and $M(p\mu)$ data distribution for negative and positive $P_L(\nu_\mu)$. In the right plot, the disappearance of combinatorial background is evident.

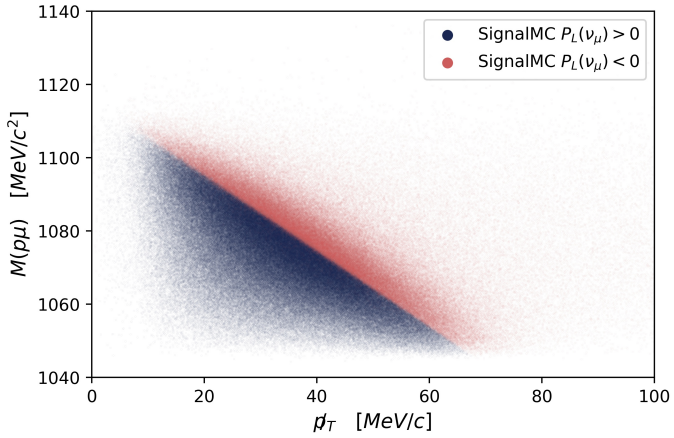

FIGURE 5.19: Signal MC distribution behaviour in the $\not{p}_T$ vs $M(p\mu)$ plane for both $P_L(\nu_\mu)$ signs.

are one of the primary background sources in Data. However, this background is eliminated when applying the $P_L(\nu_\mu) > 0$ selection, as shown in the right plot.

One of the parameters that enters in the differential decay rate for the SHD is $\Delta = M_1 - M_2$, with $M_1(M_2)$ the parent (daughter) baryon mass. The Δ value is directly related with the available momentum fo the neutrino. In the $\Lambda \longrightarrow p$ case, $\Delta \approx 177\ MeV/c^2$ and there is limited momentum available for the neutrino. For comparison, in the $\Xi \longrightarrow \Lambda$ case, $\Delta \approx 206\ MeV/c^2$.

As a consequence, the longitudinal neutrino momentum distribution for the signal closely resembles the reconstructed $\Lambda \longrightarrow p\pi^-$ longitudinal neutrino momentum. As discussed previously, for the $\Lambda \longrightarrow p\pi^-$ channels, there is not a neutrino present. As a consequence, if we compute $P_L(\nu_\mu)$ using TRUE information, we will invariably find $P_L(\nu_\mu) = 0$. However, due to the LHCb momentum resolution, when computing

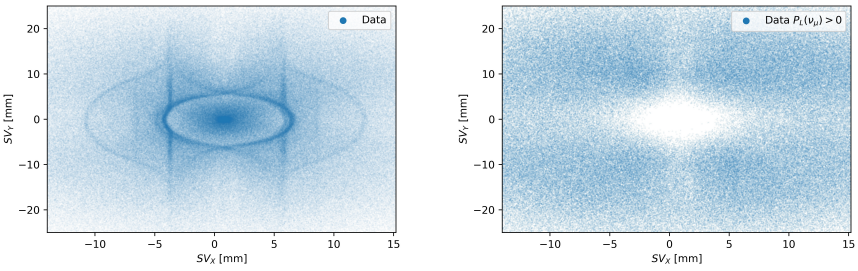

FIGURE 5.20: SV_X vs SV_Y plane for data before any selection (left) and for data with positive $P_L(\nu_\mu)$. In the right plot we can see the disappearance of material interactions.

$P_L(\nu_\mu)$ for $\Lambda \rightarrow p\pi^-$ events, we observe a distribution.

To illustrate this, Figure 5.21 displays the distributions of Signal MC Reco, Lppi MC Reco, and Lppi MC True $P_L(\nu_\mu)$. While the Lppi MC True $P_L(\nu_\mu)$ is consistently 0, the reconstructed value spectrum exhibits significant overlap with the Signal distribution.

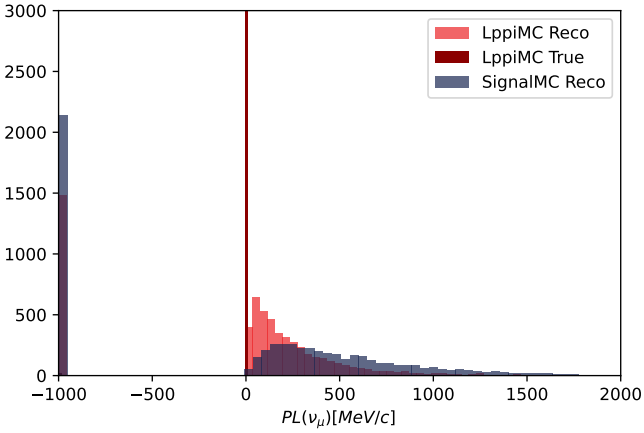

FIGURE 5.21: Signal MC Reco, Lppi MC Reco and LppiMC True $P_L(\nu_\mu)$ distributions.

One of the main challenges for this analysis is the limited statistics of Background (Lppi, eDIF) MC samples, primarily due to the low efficiency of the Signal stripping line. The efficiency of the $P_L(\nu_\mu) > 0$ cut is slightly lower for Signal compared to Lppi and eDIF (see Tab. 5.10). However, this is not a significant issue since it effectively removes most of the problematic background sources while still retaining sufficient statistics of Lppi and eDIF for a reliable fit. Therefore, our strategy aims not only to enhance the signal purity in the selected data, mainly by killing combinatorial background, but also to maintain an adequate background template with significant statistics.

TABLE 5.10: $P_L(\nu_\mu) > 0$ efficiencies for Signal, Lppi and eDIF MC.

	$P_L(\nu_\mu) > 0$ **Efficiency**
Signal MC $\epsilon^{P_L(\nu_\mu)>0}_{\Lambda\to p\mu^-\bar{\nu}_\mu}$	0.63656 ± 0.00063
Lppi MC $\epsilon^{P_L(\nu_\mu)>0}_{\Lambda\to p\pi^-}$	0.7547 ± 0.0055
eDIF MC $\epsilon^{P_L(\nu_\mu)>0}_{\Lambda\to p(\pi^-\to\mu^-\bar{\nu}_\mu)}$	0.672 ± 0.011

5.5.2.2 SELECTION 1 ($\not{p}_T$ VS $M(p\mu)$ PLANE)

Considering all the information provided, an alternative approach is to select a specific region in the $\not{p}_T$ vs $M(p\mu)$ plane. This will enable us to maximize the efficiency of signal selection as much as possible, preserving the combinatorial background rejection.

This selection will be named **Sel1** and it is described by the following cuts, Sel1=$(\not{p}_T > 16)$ & $(M(p\mu) < (1116.3 - 1.03\not{p}_T))$ & $(M(p\mu) > (1122.683 - 2\not{p}_T))$. The graphical representation of the selection cuts can be observed in Figure 5.22.

This cut significantly increases the signal purity. However, it also has a drawback: it reduces the available Background MC statistics for performing the fit.

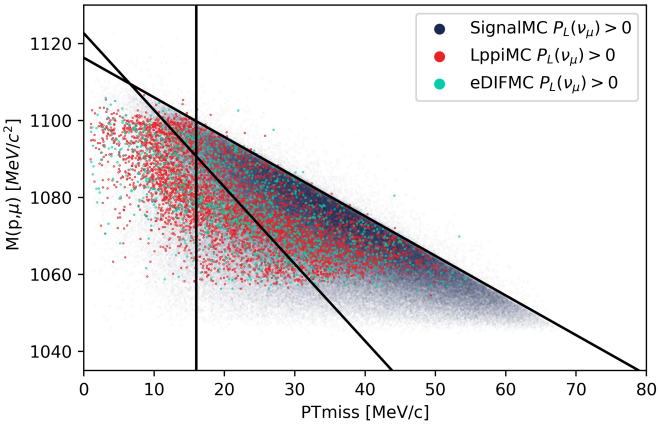

FIGURE 5.22: Graphical representation of the Sel1 selection cuts in the $\not{p}_T$ vs $M(p\mu)$ plane. Sel1=$(\not{p}_T > 16)$ & $(M(p\mu) < (1116.3 - 1.03\not{p}_T))$ & $(M(p\mu) > (1122.683 - 2\not{p}_T))$

TABLE 5.11: Sel1 efficiencies for Signal, Lppi and eDIF MC.

	Sel1 Efficiency
Signal MC $\epsilon^{\text{Sel1}}_{\Lambda\to p\mu^-\bar{\nu}_\mu}$	0.63656 ± 0.00065
Lppi MC $\epsilon^{\text{Sel1}}_{\Lambda\to p\pi^-}$	0.3175 ± 0.0060
eDIF MC $\epsilon^{\text{Sel1}}_{\Lambda\to p(\pi^-\to\mu^-\bar{\nu}_\mu)}$	0.325 ± 0.011

5.5.2.3 SELECTION 2 (ARMENTEROS-PODOLANSKI PLOT)

As mentioned earlier, the Armenteros-Podolanski plot can be useful in enhancing signal purity. In Fig. 5.23, possible selection cuts in this plane are shown. The central ellipse represents the region with higher signal density, while the region below the ellipse on the right corresponds to the area with higher expected signal purity in the data.

Both cuts can be applied together or separately. However, selecting only events under the ellipse on the right poses a challenge as we would have insufficient background Monte Carlo (MC) statistics passing this cut. On the other hand, choosing to select only events inside the central ellipse would result in a loss of some signal without a substantial justification.

Therefore, it appears more favorable to select events inside the yellow ellipse or below the green curve in Fig. 5.23. This cut will be named Sel2.

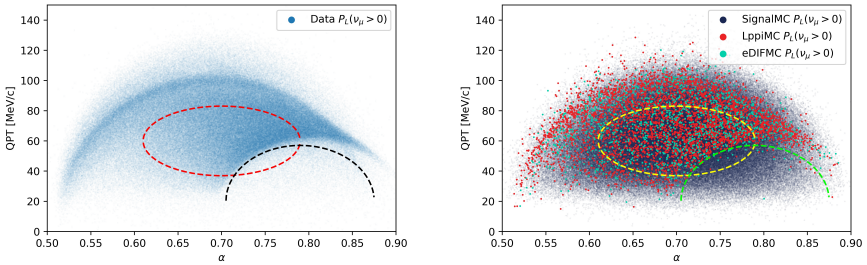

FIGURE 5.23: Armenteros-Podolanski plane for Data (left) and MC (right) with positive $P_L(\nu_\mu)$. Dashed lines represent possible selection cuts.

It is also remarkable that the requirement of a positive $P_L(\nu_\mu)$ is an exceptionally effective cut for removing $K^0_S \to \pi^+\pi^-$ background. Initially, our approach involved applying a cut in the Armenteros-Podolanski plot to eliminate this background contribution. However, we found that the removal power of both selections was comparable, with the positive longitudinal neutrino momentum requirement offering the advantage of preserving a larger number of signal, Lppi, and eDIF decays. Both strategies

TABLE 5.12: Sel2 efficiencies for Signal, Lppi and eDIF MC.

	Sel2 Efficiency
Signal MC $\epsilon^{\text{Sel2}}_{\Lambda\to p\mu^-\bar{\nu}_\mu}$	0.54024 ± 0.00065
Lppi MC $\epsilon^{\text{Sel2}}_{\Lambda\to p\pi^-}$	0.3537 ± 0.0061
eDIF MC $\epsilon^{\text{Sel2}}_{\Lambda\to p(\pi^-\to\mu^-\bar{\nu}_\mu)}$	0.3713 ± 0.011

are represented in Fig. 5.24. So, in summary, we are applying the Sel1 + Sel2 selection, and there is no need for any additional cut in the Armenteros-Podolanski plot.

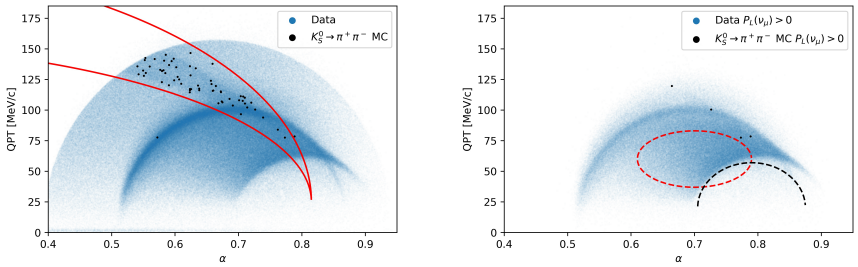

FIGURE 5.24: Armenteros-Podolanski plane for Data and $K^0_S\to\pi^+\pi^-$ MC previously to any selection (left) and requiring positive $P_L(\nu_\mu)$ (right). Solid and dashed lines represent possible selection cuts.

5.5.2.4 SIGNAL SELECTION SUMMARY

In summary, our selection strategy focused on removing combinatorial background and $K^0_S\to\pi^+\pi^-$ while preserving a substantial number of $\Lambda\to p\pi^-$ decays and early decays in flight for the purpose of performing a fit.

The requirement of $P_L(\nu_\mu)>0$, implicit in Sel1, effectively addressed most of our concerns. Both Sel1 and Sel2 cuts proved to be useful in enhancing signal purity and preventing any potentially harmful background from entering the selection.

An additional requirement of $MCorr(p\pi)<1160$ and $M(p\pi)<1120$ was applied.

Taking into account that:

$$\text{Sel1} = \left(\not{p}_T > 16\right) \,\&\, \left(M(p,\mu) < (1116.3 - 1.03\not{p}_T)\right) \,\&\, \left(M(p,\mu) > (1122.683 - 2\not{p}_T)\right)$$

$$\text{Sel2A} = \left(\left(QPT < (\sqrt{0.18^2 - \left(\frac{\alpha - 0.7}{0.5}\right)^2} \times 128 + 60)\right) \,\&\, \left(QPT > (-\sqrt{0.18^2 - \left(\frac{\alpha - 0.7}{0.5}\right)^2} \times 128 + 60)\right)\right)$$

$$\text{Sel2B} = (QPT < ((40 + \sqrt{50^2 - 4 \times (25^2 - 37^2 \times (1 - (\frac{\alpha - 0.79)^2}{0.085^2}))})/2))$$

Sel2 = (Sel2A | Sel2B)

The final selection applied is as follows:

$$\text{Sel} = \text{Sel1} \;\&\; \text{Sel2} \;\&\; MCorr(p,\pi) < 1160 \;\&\; M(p,\pi) < 1120$$

The Selection Efficiency for Signal for each year and polarity can be found in Tab. 5.13.

TABLE 5.13: $\epsilon^{\text{Selection}}_{\Lambda\to p\mu^-\overline{\nu}_\mu}$ for each year and polarity.

	Magnet Down	Magnet Up
$\epsilon^{\text{Selection}}_{\Lambda\to p\mu^-\overline{\nu}_\mu}$ 2018	0.3011 ± 0.0015	0.3011 ± 0.0015
$\epsilon^{\text{Selection}}_{\Lambda\to p\mu^-\overline{\nu}_\mu}$ 2017	0.3004 ± 0.0015	0.3016 ± 0.0015
$\epsilon^{\text{Selection}}_{\Lambda\to p\mu^-\overline{\nu}_\mu}$ 2016	0.3033 ± 0.0015	0.2989 ± 0.0015

With this selection the signal purity in the MinBias MC passing SignalLine increases from 3.48 % to 9.82 %, with the additional advantage of the strong combinatorial background suppression.

5.5.3 NORMALISATION SELECTION

The initial idea was to have two stripping lines with aligned cuts, excluding particle identification ones. But one of the cuts, the muon impact parameter required in the SignalLine, was not included in the NormLine, so the first cut to add was to require an impact parameter for the pion greater than one ($\pi_{IP} > 1$ mm).

Besides that, another cut was designed to remove the $K^0_S \to \pi^+\pi^-$ component that pollutes the NormLine Data sample. This can easily be observed in the Armenteros-Podolanski plot (Fig. 5.25).

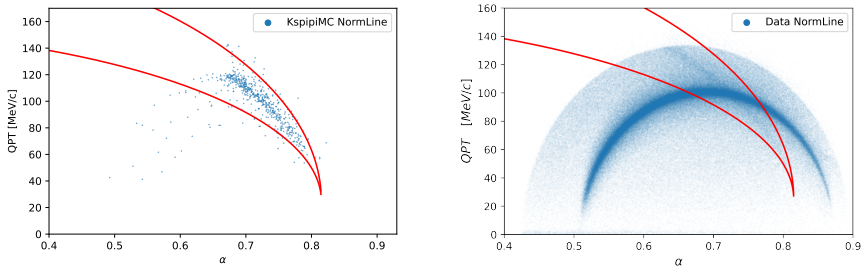

FIGURE 5.25: Armenteros-Podolanski plot for $K^0_S \to \pi^+\pi^-$ MC passing NormLine (left) and Data passing NormLine (right).

The cut is excluding events falling inside the region bounded by the red lines and can be applied imposing (Cut 1 | Cut 2), where these cuts are:

$$\text{Cut 1} : QPT > \left(25.2 + \sqrt{(25.2)^2 - 4.\left(25^2 - 200^2.\left(1 - \frac{\alpha^2}{0.815^2}\right)\right)}\right)/2 \tag{5.25}$$

$$\text{Cut 2} : QPT < \left(25.2 + \sqrt{(25.2)^2 - 4.\left(25^2 - 130^2.\left(1 - \frac{\alpha^2}{0.815^2}\right)\right)}\right)/2 \tag{5.26}$$

The cut to kill the $K^0_S \to \pi^+\pi^-$ component was designed by studying different simulation samples passing the NormLine.

This $K^0_S \to \pi^+\pi^-$ behaviour can be observed in Fig. 5.25.

5.6 NORMALISATION

5.6.1 FIT MINBIAS MC $\Lambda \longrightarrow p\pi^-$ PEAK

Our first step to fit the NormLine $M(p\pi)$ is to obtain the tail parameters of the $\Lambda \longrightarrow p\pi^-$ peak.

To obtain these parameters, we should fit a pure sample of $\Lambda \longrightarrow p\pi^-$ MC passing the NormLine. The sample is selected by applying to the MinBias MC that passes the NormLine truth-matching conditions, which are equivalent to those used for selecting $\Lambda \longrightarrow p\pi^-$ MC passing the SignalLine. The explicit requirements can be found in the appendices, A.4.

The $M(p\pi)$ distribution was fitted to a double sided Crystal Ball pdf, as can be seen in Fig. 5.26.

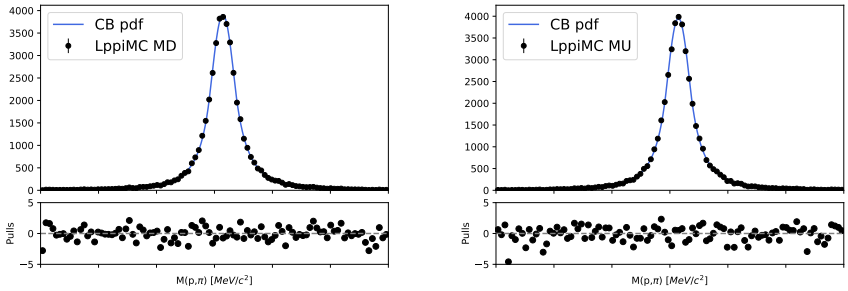

FIGURE 5.26: $M(p\pi)$ fit of the pure $\Lambda \longrightarrow p\pi^-$ MC passing NormLine. Magnet Down (MD) is depicted on the left and Magnet Up (MU) on the right. χ^2/ndof is 1.52 for MU and 1.16 for MD.

The double sided Crystal Ball tail parameters extracted from the fit are in table 5.14. These two fits were performed using zfit.

TABLE 5.14: Tail parameters of the double sided crystal ball that fits the $M(p\pi)$ of the pure $\Lambda \longrightarrow p\pi^-$ MC passing NormLine. $\Lambda \longrightarrow p\pi^-$ decays were selected from a MinBias MC LHCb production for 2018MU and 2018MD.

	α_L	α_R	n_L	n_R
2018MU	1.046 ± 0.027	1.025 ± 0.026	3.43 ± 0.14	3.30 ± 0.13
2018MD	1.085 ± 0.026	1.012 ± 0.024	3.21 ± 0.12	3.39 ± 0.13

5.6.2 FIT DATA NORMLINE

Having the tail parameters, we can perform a fit to the Data in NormLine. The combinatorial background can be parameterized with an exponential function and the $\Lambda \rightarrow p\pi^-$ component with a double sided crystal ball, where we set the tail parameters obtained by fitting the pure $\Lambda \rightarrow p\pi^-$ MC NormLine sample in previous subsection.

This process should be repeated for all years and polarities to measure the total amount of $\Lambda \rightarrow p\pi^-$ in NormLine ($N^{\text{NormLine}}_{\Lambda\rightarrow p\pi^-}$).

Fig. 5.27 shows the fit result for 2018MU and 2018MD, applying Common Cuts to NormLine Data. Only α_L, α_R, n_L and n_R were set, whereas we let the width and the center of the double sided Crystal Ball and the exponential parameter to float.

The fit process was repeated for all years and polarities, and the number of $\Lambda \rightarrow p\pi^-$ decays measured in each case are shown in Tab. 5.15.

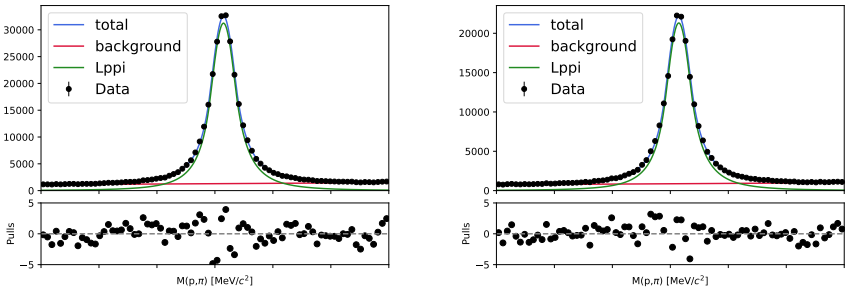

FIGURE 5.27: $M(p\pi)$ fit of the $\Lambda \rightarrow p\pi^-$ yield in Data passing NormLine. Magnet Up is depicted on the left and Magnet Down on the right. χ^2/ndof is 2.54 for MU and 2.33 for MD.

TABLE 5.15: Number of $\Lambda \rightarrow p\pi^-$ decays in NormLine Data for each year and polarity. $N^{\text{NormLine}}_{\Lambda\rightarrow p\pi^-}$ was extracted from the fit of NormLine $M(p\pi)$ with common cuts to an exponential + a double sided Crystal Ball where the tail parameters have been set to match the TRUE ID ones.

	Magnet Down	MagnetUp
2018	16080300 ± 4900	17254500 ± 5100
2017	14454500 ± 4700	13933100 ± 4600
2016	16527000 ± 4900	14902400 ± 4700

5.6.3 $\Lambda \to p\pi^-$ EFFICIENCY PASSING NORMLINE

Our next goal is to know how many $\Lambda \to p\pi^-$ decays we have before the stripping process. This can be computed once we obtain the average of the $\Lambda \to p\pi^-$ events that are reconstructed and pass the NormLine ($\epsilon^{\text{NormLine}}_{\Lambda\to p\pi^-}$).

The efficiency can be computed performing a fit to the MinBias MC sample that passes the NormLine to a double sided Crystal Ball + a exponential, where we also set the tail parameters obtained in the Fig. 5.14. Dividing the number of $\Lambda \to p\pi^-$ events measured with the fit in the MinBias MC NormLine sample by the original amount of $\Lambda \to p\pi^-$ in the sample before any reconstruction or stripping.

The original amount of $\Lambda \to p\pi^-$ in the sample before any reconstruction or stripping for each year and polarity can be found in Tab. 5.16. These values are the number of entries in the MCDecayTree, generated in the same tuple processing that created the MinBias MC NormLine samples to ensure that we are always comparing the same original sample.

The fit results for the MinBias MC sample passing NormLine can be found in Fig. 5.28 and Tab. 5.17.

TABLE 5.16: Number of $\Lambda \to p\pi^-$ decays before the reconstruction and stripping process for each year and polarity in the MinBias MC sample.

	Magnet Down	MagnetUp
2018	294,890752 M	295,092897 M

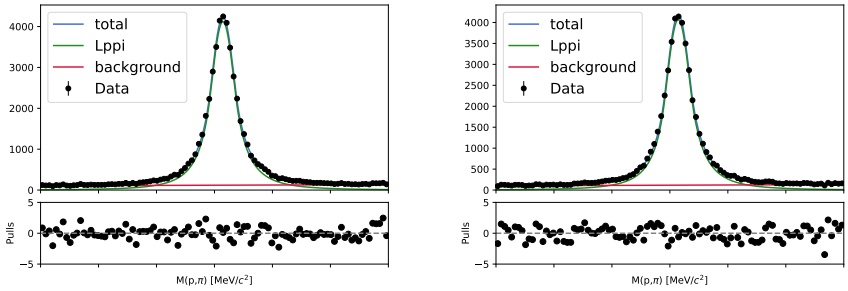

FIGURE 5.28: $M(p\pi)$ fit of MinBias MC passing NormLine to an exponential + a double sided Crystal Ball, were the tail parameters were set to match the TRUE ID fit ones. Magnet Up is depicted on the left and Magnet Down on the right. χ^2/ndof is 1.20 for MU and 1.17 for MD.

Dividing the Tab. 5.17 results by the Tab. 5.16 ones, we obtain the $\epsilon^{\text{NormLine}}_{\Lambda\to p\pi^-}$ (Tab. 5.18).

TABLE 5.17: Number of $\Lambda \to p\pi^-$ decays in NormLine MinBias MC for each year and polarity. Numbers were extracted from the zfit of NormLine $M(p\pi)$ with common cuts to an exponential + a double sided Crystal Ball where tail parameters have been set to match the TRUE ID ones.

	Magnet Down	MagnetUp
2018	46590 ± 250	46620 ± 250

TABLE 5.18: Computed NormLine $\Lambda \to p\pi^-$ efficiencies for Magnet Down and Magnet Up.

	Magnet Down	MagnetUp
$\epsilon^{\text{NormLine}}_{\Lambda\to p\pi^-}$	$(1.5799 \pm 0.0085) \times 10^{-4}$	$(1.5798 \pm 0.0085) \times 10^{-4}$

5.6.4 NUMBER OF $\Lambda \to p\pi^-$ BEFORE STRIPPING

Having the amount of $\Lambda \to p\pi^-$ in NormLine and the efficiency $\epsilon^{\text{NormLine}}_{\Lambda\to p\pi^-}$ we can compute the amount of $\Lambda \to p\pi^-$ before Stripping using Eq. 5.7.

TABLE 5.19: Number of $\Lambda \to p\pi^-$ decays before the stripping for each year and polarity.

	Magnet Down	MagnetUp
2018	(101780 ± 550) M	(109220 ± 590) M
2017	(91490 ± 490) M	(88200 ± 480) M
2016	(104610 ± 560) M	(94330 ± 510) M

5.6.5 NUMBER OF Λ PARTICLES BEFORE STRIPPING

Dividing $N_{\Lambda\to p\pi^-}$ by the branching ratio ratio $\mathcal{B}(\Lambda \to p\pi^-)$ we will obtain the number of Λs before the stripping, N_Λ.

$$N_\Lambda = \frac{N_{\Lambda\to p\pi^-}}{\mathcal{B}(\Lambda \to p\pi^-)} \tag{5.27}$$

Introducing the PDG $\mathcal{B}(\Lambda \to p\pi^-)$ in Eq. 5.27 we obtain the number of Λ particles before Stripping (Tab. 5.20).

TABLE 5.20: Number of Λ particles before the stripping for each year and polarity.

	Magnet Down	MagnetUp
2018	(159300 ± 1500) M	(170900 ± 1600) M
2017	(143200 ± 1400) M	(138000 ± 1300) M
2016	(163700 ± 1600) M	(147600 ± 1400) M

5.6.6 NORMALISATION

As usual, we can define an α parameter, being:

$$\mathcal{B}(\Lambda \to p\mu^-\bar{\nu}_\mu) = \alpha N^{\text{SignalLine}}_{\Lambda\to p\mu^-\bar{\nu}_\mu} \tag{5.28}$$

where we have included all the efficiencies in the α parameter:

$$\alpha = \frac{\mathcal{B}(\Lambda \to p\pi^-)}{N^{\text{NormLine}}_{\Lambda\to p\pi^-}} \frac{\epsilon^{\text{NormLine}}_{\Lambda\to p\pi^-}}{\epsilon^{\text{SignalLineSel}}_{\Lambda\to p\mu^-\bar{\nu}_\mu}} \tag{5.29}$$

and

$$\epsilon^{\text{SignalLineSel}}_{\Lambda\to p\mu^-\bar{\nu}_\mu} = \epsilon^{\text{SignalLine}}_{\Lambda\to p\mu^-\bar{\nu}_\mu} \cdot \epsilon^{\text{Selection}}_{\Lambda\to p\mu^-\bar{\nu}_\mu} \tag{5.30}$$

Where the current PDG value for the branching ratio of the Normalization Channel is $\mathcal{B}(\Lambda \to p\pi^-) = 64.1 \pm 0.5\%$,the NormLine Sselection + Stripping efficiency $\epsilon^{\text{NormLine}}_{\Lambda\to p\pi^-}=(1.5799\pm0.0085)\times10^{-4}$ for Magnet Down and $\epsilon^{\text{NormLine}}_{\Lambda\to p\pi^-}=(1.5798\pm0.0085)\times10^{-4}$ for Magnet Up polarity, and $N^{\text{NormLine}}_{\Lambda\to p\pi^-}$, $\epsilon^{\text{SignalLine}}_{\Lambda\to p\mu^-\bar{\nu}_\mu}$ and $\epsilon^{\text{Selection}}_{\Lambda\to p\mu^-\bar{\nu}_\mu}$ values for each year and polarity can be found in Tab. 5.15, Tab. 5.5 and Tab. 5.13 respectively.

TABLE 5.21: $\epsilon^{\text{SignalLineSel}}_{\Lambda\to p\mu^-\bar{\nu}_\mu}$ for each year and polarity.

	Magnet Down	Magnet Up
$\epsilon^{\text{SignalLineSel}}_{\Lambda\to p\mu^-\bar{\nu}_\mu}$ 2018	$(1.0810 \pm 0.0070) \times 10^{-4}$	$(1.0860 \pm 0.0070) \times 10^{-4}$
$\epsilon^{\text{SignalLineSel}}_{\Lambda\to p\mu^-\bar{\nu}_\mu}$ 2017	$(1.0870 \pm 0.0070) \times 10^{-4}$	$(1.1030 \pm 0.0070) \times 10^{-4}$
$\epsilon^{\text{SignalLineSel}}_{\Lambda\to p\mu^-\bar{\nu}_\mu}$ 2016	$(1.1020 \pm 0.0070) \times 10^{-4}$	$(1.0820 \pm 0.0070) \times 10^{-4}$

As explained in Subsection 5.6.3, $\epsilon^{\text{NormLine}}_{\Lambda\to p\pi^-}$ was computed by fitting the MinBias MC sample passing the NormLine. This MinBias MC sample is only available for 2018MD and 2018MU, and the results are very similar for both cases. We will use this $\epsilon^{\text{NormLine}}_{\Lambda\to p\pi^-}$ value also for 2017 and 2016.

As we will fit the Signal in all the Run II Data, without separating by year and polarity, we should weight the $\epsilon^{\text{SignalLineSel}}_{\Lambda\to p\mu^-\bar{\nu}_\mu}$.

$$\epsilon^{\text{SignalLineSel}}_{\Lambda\to p\mu^-\bar{\nu}_\mu} = \frac{\sum_{\text{YearPol}} (N_{\text{YearPol}}{}^{\text{NormLine}}_{\Lambda\to p\pi^-} \cdot \epsilon_{\text{YearPol}}{}^{\text{SignalLineSel}}_{\Lambda\to p\mu^-\bar{\nu}_\mu})}{\sum_{\text{YearPol}} (N_{\text{YearPol}}{}^{\text{NormLine}}_{\Lambda\to p\pi^-})} \tag{5.31}$$

The result is $\epsilon^{\text{SignalLineSel}}_{\Lambda\to p\mu^-\bar{\nu}_\mu} = (1.0902 \pm 0.0027) \times 10^{-4}$. With all this values we can finally compute α:

$$\alpha = (1.073 \pm 0.011) \times 10^{-8} \tag{5.32}$$

5.7 EFFICIENCY CORRECTION

This value should be corrected after the update of the efficiencies, using PIDCalib2 and TrackCalib2.

5.7.1 PID CORRECTION

5.7.1.1 SIGNAL STRIPPING LINE

As it was previously mentioned, the efficiency for the signal passing the SignalLine can be obtained from the production logs (see tab 5.5). But the SignalLine includes some PID cuts that must be corrected using PIDCalib2. This can not be done using a stripping filtered sample, where only events passing the SignalLine cuts are recorded. Taking that into account, a private $\Lambda \rightarrow p\mu^{-}\bar{\nu}_{\mu}$ simulation has been produced.

This private sample was produced using the same Gauss/v49r20, Boole/v30r4, Moore/v25r4 and Brunel/v50r7 versions that were used in the central stripping filtered production (listed in the appendices, A.8.11). Then, the tuples were produced using DaVinci/v44r10p5 and StdAllNoPIDsProtons and StdAllNoPIDsMuons as input for the CombineParticles. Notice that the Signal Stripping Line uses StdLooseProtons and StdAllLooseMuons as input particles and those StandardParticles already include some kinematic, detector requirementes or PID cuts.

- StdLooseProtons: (PT > 250*MeV) & (MIPCHI2DV(PRIMARY) > 4.) & RequiresDet='RICH' & CombDLL(p-pi) > -5.0
- StdAllLooseMuons: RequiresDet='MUON' & IsMuon=True

In order to validate our private simulation, we checked that, by applying the stripping line cuts to it, we reproduce the stripping filtered production stripping efficiency.

We are supposing that $\epsilon^{\text{SignalLine}}_{Lpmu} = \epsilon^{\text{SignalLine}}_{CutsNoPID} \times \epsilon^{\text{SignalLine}}_{\text{CutsPID}}$, so we have to calculate each efficiency separately.

The first one, $\epsilon^{\text{SignalLine}}_{CutsNoPID}$, can be obtained applying just the NoPID Stripping Line cuts (see Tab. 5.1), including also the non PID StdLooseProtons and StdAllLooseMuons cuts and requiring InMuonAcc for the muon. Applying these cuts to the private MC we obtain a new sample that will be used as input for PidCalib2.

The $\epsilon^{\text{SignalLine}}_{\text{CutsPID}}$ will be the product of the efficiency of the muon PID cuts and the proton ones.

The PIDCalib2 commands and the followed procedure is explained in detail in the appendices (A.10.1). In our case we should use the Mu_nopt calibration sample instead of usual Mu, since the default muon calibration sample has a transverse momentum cut of 800 MeV/c and a total momentum cut of 3 GeV/c not compatible with our signal momentum distribution. Different binning schemes were designed taking into account the P, η and nSPDHits distributions to validate the results and to compute the systematic uncertainty (A.11).

The original $\epsilon^{\text{SignalLine}}_{\text{CutsPID}}$ is computed applying the PID cuts to the private simulation after having applied the others stripping cuts. The original efficiency is 46.20 ± 0.54 %

and the PIDCalib2 result is $\epsilon^{\text{SignalLine}}_{\text{CutsPID}} = 46.59 \pm 0.65$ %. This new value will replace the original $\epsilon^{\text{SignalLine}}_{\text{CutsPID}}$ in the α parameter computation.

5.7.1.2 NORMALISATION STRIPPING LINE

The NormLine was designed to have its non-PID cuts aligned with the SignalLine ones but, as it was mentioned in Sec. 5.5.3, the pi_IP_OWNPV>1 correspondent cut is missing in the NormLine.

In this case we used the MinBias MC production to compute the efficiencies. A sample where we use StdAllNoPIDsProtons and StdAllNoPIDsPions for the CombineParticles algorithm was created. In the NormLine case, the input particles are StdLooseProtons and StdAllLoosePions, which already include the following cuts:

- StdLooseProtons: (PT > 250*MeV) & (MIPCHI2DV(PRIMARY) > 4.) & RequiresDet='RICH' & CombDLL(p-pi) > -5.0
- StdAllLoosePions: RequiresDet='RICH' & RequiresDet='CALO'

So, following the same procedure applied to correct the SignalLine PID efficiency, we should apply the non-PID cuts to the $\Lambda \rightarrow p\pi^-$ events from the MinBias MC sample and compute the PID cuts efficiencies for this sample using PIDCalib2.

As it was detailed in the previous case, we should study the binning variables distributions (P, ETA, nSPDHits) of the MinBiasMC sample once the non-PID cuts were applied in order to design the binning files for the proton and the pion.

In addition, we should use the Pi_KS sample when making the efficiency histograms and computing the efficiency for the pion case, since the usual Pi sample momentum distribution does not match our pion ones.

The commands and followed procedure is explained in detail in the appendices (A.10.2).

The original $\epsilon^{\text{NormLine}}_{\text{CutsPID}} = 47.0 \pm 1.4$ % and the PIDCalib2 result is $\epsilon^{\text{NormLine}}_{\text{CutsPID}} = 42.50 \pm 0.14$ %.

5.7.2 TRACKING CORRECTION

Tracking related cuts are aligned in both lines, which should cancel most systematic uncertainties. Anyway, since the kinematic properties of the reconstructed particles are slightly different in the $\Lambda \rightarrow p\pi^-$ and signal we should correct the tracking efficiencies, something that can be done using TrackCalib2.

Any tracks that do not fall into the momentum-η spectrum provided by TrackCalib (such as tracks with a momentum below 5 GeV/c) are assigned a correction factor of 1.00 ± 0.05 as recommended by the TrackCalib authors. This is something that happens 76.04 % of $\Lambda \rightarrow p\pi^-$ pions and for 81.21 % of Signal muons.

Even for those events falling inside the momentum-eta spectrum provided by TrackCalib the correction is very small, both for protons and muon/pions.

The TrackCalib correction is almost done and will be included in the following days.

5.7.2.1 SIGNAL STRIPPING LINE

The corrected efficiency is:

The original $\epsilon^{\text{SignalLine}}_{\text{CutsTracking}} = 0.4347 \pm 0.0052\,\%$ and the TrackCalib2 result is $\epsilon^{\text{SignalLine}}_{\text{CutsTracking}} = 0.435 \pm 0.027\,\%$.

5.7.2.2 NORM STRIPPING LINE

The original $\epsilon^{\text{NormLine}}_{\text{CutsTracking}} = 0.1175 \pm 0.0045\,\%$ and the TrackCalib2 result is $\epsilon^{\text{NormLine}}_{\text{CutsTracking}} = 0.1170 \pm 0.0090\,\%$.

5.7.3 FINAL NORMALISATION RESULT

The final corrected result is

$$\alpha = (9.61 \pm 0.35) \times 10^{-9} \tag{5.33}$$

5.8 SIGNAL YIELD FIT

The signal yield in SignalLine can be obtained using different approaches. For example, we can attempt to fit the signal yield in any of the corrected mass variables using our simulation as a template, employing a Kernel Density Estimation (KDE) to obtain a probability density function (PDF). The main challenge associated with this strategy is the low background MC statistics, which results in significant uncertainties when using a KDE or challenges in modeling the background PDF.

An alternative two-dimensional fitter was developed to tackle this issue. The $MCorr(p\pi)$ and $M(p\pi)$ plane is divided into bins, as illustrated in Fig. 5.29, and the 2D fitter can provide the yield of each channel in the data by utilizing the MC distributions for each respective channel.

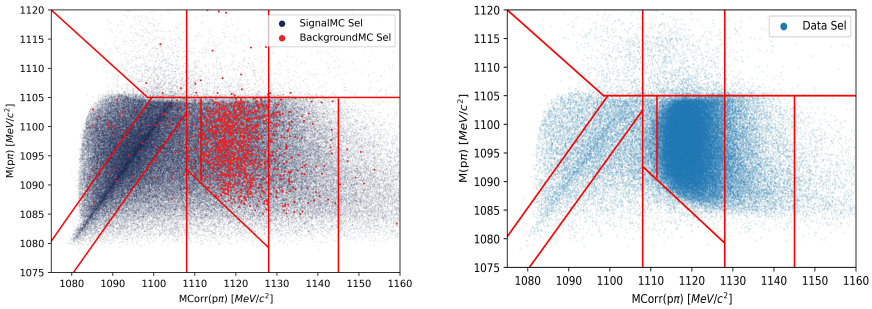

FIGURE 5.29: Proposed binning of the $MCorr(p\pi)$ vs $M(p\pi)$ plane to perform a bi-dimensional fit. In the left plot we can see the selected Signal and $\Lambda \rightarrow p\pi^-$ behaviour in the 2D plane and in the right one the data distribution in it.

The proposed binning scheme was crafted to encapsulate the behavior of both the signal and the background in the two-dimensional plane. Primarily, the signal exhibits a distinct concentration around the $MCorr(p\pi) = M(p\pi)$ line. The diagonal bin is expected to have the highest signal purity. The two bins situated immediately to the right and left of this diagonal bin also display a pronounced signal purity. By amalgamating these three bins, we enhance our sensitivity for measuring the signal yield in the data.

The central bin exhibits a pronounced background purity. It's intentionally designed to encompass the region with the most concentrated background. In the bins positioned immediately to the right and left of the central bin, we anticipate a substantial presence of both signal and background. This mixed composition aids in accurately fitting the quantities of each component. The remaining bins serve as control regions.

In line with these concepts, four additional binning schemes were developed (see Fig. 5.35). Some of these schemes feature more uniformly sized bins, while one has a narrower diagonal region, aiming to more accurately encapsulate the signal concentration around the $MCorr(p\pi) = M(p\pi)$ line.

In order to perform the fit we need the MC templates passing the SignalLine selection for each of the considered channels: Signal, eDIF, $\Lambda \rightarrow p\pi^-$ and combinatorial background.

5.8.1 FIT MC TEMPLATES

In this section, we will explain the process of obtaining the various templates for the signal yield fit. The Signal, eDIF, and $\Lambda \rightarrow p\pi^-$ samples are derived from their respective Stripping Filtered MC samples. First of all, as it was explained in Sec. 5.4, correspondant truth-matching conditions for each channel, that are detailed in the appendices A.3 are applied. Then, the selection detailed in Sec. 5.5.2.4 is applied to all the samples. Regarding the combinatorial background, the sample was obtained as explained below:

5.8.1.1 COMBINATORIAL BACKGROUND

The combinatorial background is also a challenge for this analysis. Once again, the main issue arises from the restrictive nature of the stripping line, which limits the availability of a sufficiently large combinatorial background sample.

The combinatorial background MC sample is chosen by requiring MinBias MC events that pass the SignalLine to not meet any of the truth-matching conditions detailed in Appendix A.3 for Signal, eDIF, $\Lambda \rightarrow p\pi^-$, and $K^0_S \rightarrow \pi^+\pi^-$. This essentially involves excluding these channels (all the observed peaking backgrounds) from the MinBias MC sample.

To estimate the general properties of the combinatorial background, we can select data with $\rho_{SV} < 2$ ($\rho_{SV} = \sqrt{SV^2_X + SV^2_Y}$), which would be completely dominated by such events. Figure 5.30 illustrates how the shape of these events aligns with the observed combinatorial background in Data.

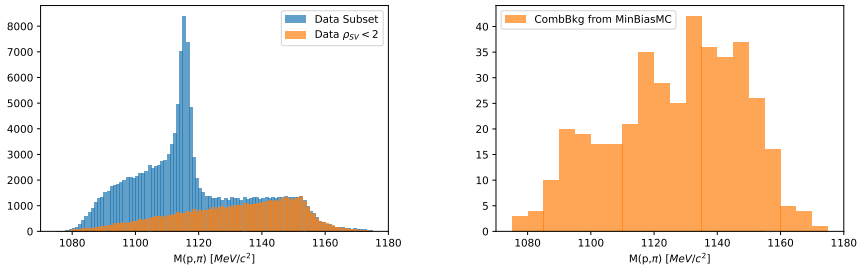

FIGURE 5.30: Data subset $M(p\pi)$ comparison with the $\rho_{SV} < 2$ data suggests that those events are completely dominated by combinatorial background (left). In the right plot we can see the $M(p\pi)$ distribution for combinatorial background extracted from MinBias MC passing SignalLine.

Something that we can do is to estimate the amount of CombBkg in Data by comparing the total amount of data, the amount of data satisfying $\rho_{SV} < 2$ and the

size of the data subset that matches the $\rho_{SV} < 2$ combinatorial background shape. The estimated result is ~ 491000 combinatorial background events in Data passing SignalLine.

Our initial approach involves extracting the combinatorial background template from the MinBias MC sample that passes the SignalLine. The idea was to remove Signal, Lppi, eDIF, and Kspipi events using the TRUE ID and TRUE vertex position information. Its $M(p\pi)$ distribution can be found in Fig. 5.30. This sample consists of 406 events.

We can apply the $P_L(\nu_\mu) > 0$ selection cut to this combinatorial background sample and calculate the efficiency of the cut. Since 40 events passed this requirement, we find an efficiency of $\epsilon^{P_L(\nu_\mu)>0}_{\text{CombBkg}}$=0.099 ± 0.015.

Considering this efficiency and the amount of combinatorial background observed in Data, ~ 491000 events, we expect ~ 48375 combinatorial background events with positive longitudinal neutrino momentum in Data, something that doesn't seem compatible with the amount of data passing the cut, considering the expected amount of signal and $\Lambda \to p\pi^-$ background.

However, having only 40 events is not sufficient to extract reliable properties or create a significant template. We should explore other sources of combinatorial background, and the stripping filtered Signal MC and stripping filtered $\Lambda \to p\pi^-$ MC samples are good starting points.

5.8.1.2 COMBINATORIAL BACKGROUND IN STRIPPING FILTERED MC SAMPLES

Applying the same TRUE ID and vertex requirements that we previously used to select combinatorial background to the Stripping Filtered Signal MC sample, we find a concerning result. As it can be seen in Fig. 5.31, most of the MC events are in fact misidentified $\Lambda \to p\mu^-\bar{\nu}_\mu$ (ghosts). The same happens with the Lppi stripping filtered MC sample.

Since misidentification is observed in the stripping filtered MC samples, it is reasonable to assume that the Combinatorial Background extracted from the MinBias MC sample may also contain both signal and, mainly, $\Lambda \to p\pi^-$ events. This poses a risk as it could lead to an overestimation of the efficiency of the positive longitudinal neutrino momentum requirement for combinatorial background events ($\epsilon^{P_L(\nu_\mu)>0}_{\text{CombBkg}}$), specially considering that this selection is specifically designed to remove combinatorial background.

5.8.1.3 BDT TO SEPARATE GHOSTS AND COMBINATORIAL BACKGROUND

One possible solution to assess the accuracy of the estimation $\epsilon^{P_L(\nu_\mu)>0}_{\text{CombBkg}}$ is to train a Boosted Decision Tree (BDT) to distinguish between signal and combinatorial background in the events identified as combinatorial background from the Signal Stripping Filtered Monte Carlo (MC) sample. The same procedure can also be performed on the Lppi Stripping Filtered MC samples.

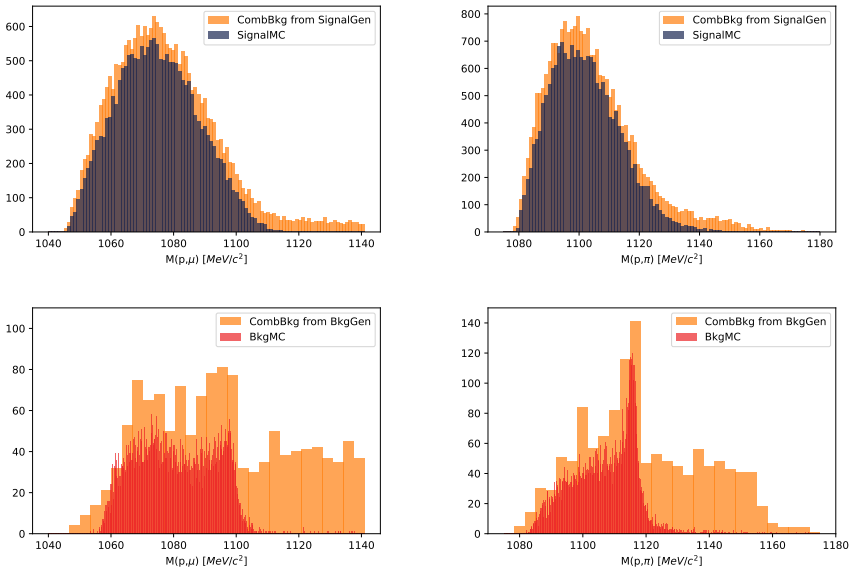

FIGURE 5.31: $M(p\mu)$ and $M(p\pi)$ distributions of "Comb Bkg MC " from Signal (top) and Lppi (bottom) stripping filtered MC samples where it is easy to see that most of events identified as combinatorial background are in fact misidentified signal or Lppi background events.

A sklearn GradientBoostingClassifier [64] was trained using as signal the $\Lambda \rightarrow p\mu^- \bar{\nu}_\mu$ MC and as background the $\rho_{SV} < 2$ data. The training variables were $M(p\mu)$, APLA, Armenteros α, Lambda ETA, Lambda PT and Lambda EndVertex_Z.

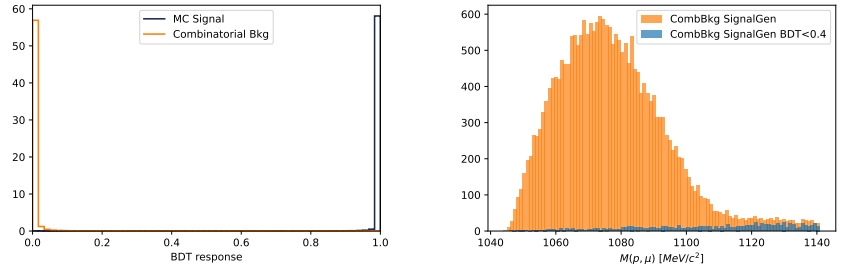

FIGURE 5.32: The BDT response can be used to separate $\Lambda \rightarrow p\pi^-$ and Signal from combinatorial background (left). In the plot placed at the right the effect of selecting events with BDT response < 0.8 in the events identified as combinatorial background from the Stripping Filtered MC sample can be found.

This process serves two purposes. Firstly, it allows us to enhance the statistics of our combinatorial background MC sample by separating the signal and combinatorial

background components (see Fig. 5.32). Secondly, we can evaluate the BDT response values for combinatorial background events from the MinBias MC sample that satisfy the $P_L(\nu_\mu) > 0$ cut. This enables us to determine whether these events are genuine combinatorial background or potential misidentifications as Signal or Lppi.

Figure 5.33 demonstrates that a significant number of events identified as combinatorial background from the MinBias MC sample exhibit signal and peaking background characteristics. More importantly, the events selected with $P_L(\nu_\mu) > 0$ are highly unlikely to be combinatorial background. This indicates that our previous estimation of $\epsilon_{\text{CombBkg}}^{P_L(\nu_\mu)>0}$ has greatly overestimated its value.

Furthermore, it is not appropriate to utilize the events identified as combinatorial background from the MinBias MC with a positive neutrino longitudinal momentum as the combinatorial background template in the signal yield fit.This is because the resulting template would be completely dominated by Lppi, as can be seen in the bottom plots of Figure 5.33.

Since we have now obtained the combinatorial background from the signal stripping filtered MC sample (selected using the BDT), we can compute the efficiency $\epsilon_{\text{CombBkg}}^{P_L(\nu_\mu)>0}$ for those events with a BDT response < 0.4. The result is $\epsilon_{CombBkgBDT<0.4}^{P_L(\nu_\mu)>0} = 0$. However, this does not imply that there is no combinatorial background in the data with $P_L(\nu_\mu) > 0$, as the BDT does not select every single combinatorial background event and we cannot directly compute the efficiency. But it is evident that the combinatorial background is effectively suppressed when applying $P_L(\nu_\mu) > 0$.

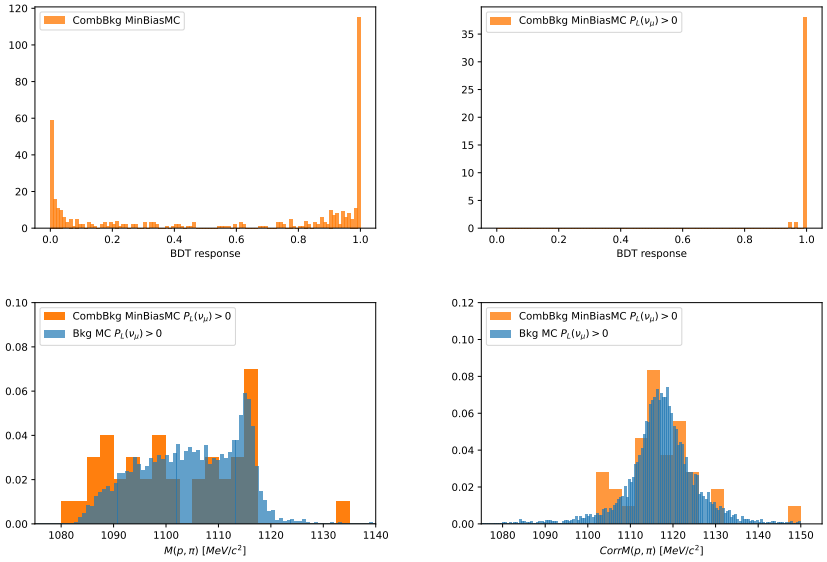

FIGURE 5.33: Top plots show BDT response for all events identified as combinatorial background in the MinBias MC sample (left) and for those events passing the $P_L(\nu_\mu) > 0$ cut (right). Bottom plots are $M(p\pi)$ and $CorrM(p\pi)$ distributions for "combinatorial background" from MinBias MC sample and for Lppi bkg MC, both passing $P_L(\nu_\mu) > 0$.

Taking all that information into account, the best option for selecting a combinatorial background template is to combine the events identified as combinatorial background from both the MinBias MC sample and the background-stripping filtered MC sample. Since we are only interested on the number of signal events, we are not concerned by the fact that most events in our combinatorial background sample are in fact $\Lambda \longrightarrow p\pi^-$ ghosts.

5.8.2 MC WEIGHT

To account for the discrepancies between the Monte Carlo (MC) and Data, we performed a reweighting of the MC to align its properties with those observed in the Data. The variables that we are reweighting are Λ P_T and η. By fitting the $\Lambda \longrightarrow p\pi^-$ contribution in the NormLine region of the Data, we can extract the P_T and η distributions of $\Lambda \longrightarrow p\pi^-$ in the Data and apply corresponding reweighting factors to the MC.

The first part of the process is analogous to the one followed when fitting the NormLine to extract the yield of $\Lambda \longrightarrow p\pi^-$ events.(Subsection 5.6.2). In this case we obtained the sWeights using the hepstats package from the fit results and then we passed those sWeights to a GBreweighter from the hep_ml package. So, the GBReweighter is trained using the whole $\Lambda \longrightarrow p\pi^-$ data sample passing NormLine, selected with the sWeights method, to correct the differences between MC and Data in Λ P_T and η distributions.

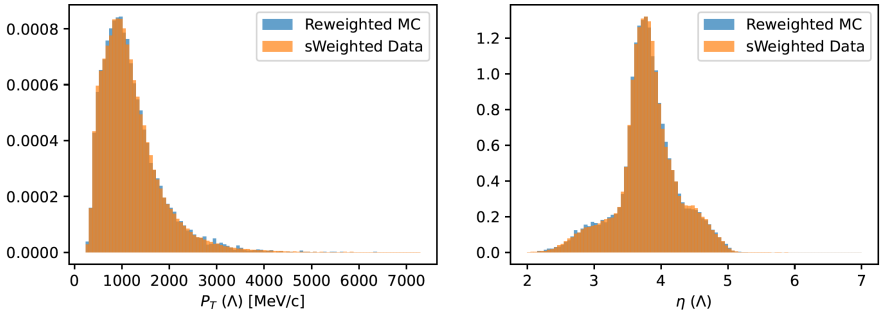

FIGURE 5.34: Reweighting result for $\Lambda \longrightarrow p\pi^-$ MC passing NormLine. Λ transverse momentum is depicted in the left plot and its pseudorapidity in the right one.

This reweighter, already trained to correct the discrepancies between MC and Data, was used then to predict the corresponding reweighing of $\Lambda \longrightarrow p\pi^-$ MC passing SignalLine. The reweighted histograms can be found in Fig. 5.34.

5.8.3 FIT

The 2D fitter takes as input the number of entries for each channel in each bin, utilizing the MC distributions as templates, and outputs the corresponding number of occurrences for each channel in the Data. It performs a log likelihood calculation using Poisson statistics, addressing the low statistics issue.

The maximum likelihood with binned data case procedure [38] is followed to fit the contribution of each channel to the selected data. For each bin, the fitter computes a $\chi^2 = 2(-\text{OBS} \cdot log(\text{EXP}) + \text{EXP})$, where OBS is the observed amount of selected data in the bin and EXP is the expected sum of all the components in the bin:

$$\text{EXP} = f_{\Lambda \to p\mu^- \bar{\nu}_\mu} \cdot \frac{\mathcal{B}(\Lambda \to p\mu^- \bar{\nu}_\mu)}{\alpha} + f_{\Lambda \to p\pi^-} \cdot N_{\Lambda \to p\pi^-} + f_{eDIF} \cdot N_{eDIF} + f_{Comb} \cdot N_{Comb}$$

where the fractions of each channel in each bin are extracted from the MC samples, the α parameter was already computed previously in this thesis and the $\mathcal{B}(\Lambda \to p\mu^- \bar{\nu}_\mu)$ and number of each background channel are being fitted. In the fitting process, a Gaussian constraint for the normalization parameter (α) is incorporated. This approach effectively integrates prior knowledge about α into the fit.

Different binning schemes were used and the blinded results are presented in Tab. 5.22. Result are blinded by multiplying the α normalisation parameter by a random number between 0 and 3 (blinding constant). Three different modes were implemented, the first one (first column) sets the $\Lambda \to p\pi^-$ and $\Lambda \to p(\pi^- \to \mu^- \bar{\nu}_\mu)$ ratio to the one observed in the MinBias MC passing the selection, the second mode (second column) lets this ratio free and the third one (third column) considers also the combinatorial background channel. As it was discussed in the section 5.8.1, the MC template for the combinatorial background is very likely mismatched $\Lambda \to p\pi^-$, and the expected contribution of combinatorial background to the selected sample is extremely low.

TABLE 5.22: Blinded $\mathcal{B}(\Lambda \to p\mu^- \bar{\nu}_\mu)$ fit result for different binning schemes and background templates are included.

Scheme	Merged Lppi+eDIF	Lppi,eDIF	Lppi,eDIF,CombBkg
Binning 1 ($\times 10^{-4}$)	$\mathcal{B}$ = 3.865 ± 0.051	$\mathcal{B}$ = 3.913 ± 0.068	$\mathcal{B}$ = 3.780 ± 0.066
Binning 2 ($\times 10^{-4}$)	$\mathcal{B}$ = 3.793 ± 0.052	$\mathcal{B}$ = 4.041 ± 0.074	$\mathcal{B}$ = 3.734 ± 0.067
Binning 3 ($\times 10^{-4}$)	$\mathcal{B}$ = 3.806 ± 0.051	$\mathcal{B}$ = 3.965 ± 0.072	$\mathcal{B}$ = 3.753 ± 0.059
Binning 4 ($\times 10^{-4}$)	$\mathcal{B}$ = 3.865 ± 0.049	$\mathcal{B}$ = 3.899 ± 0.073	$\mathcal{B}$ = **3.845 ± 0.059**
Binning 5 ($\times 10^{-4}$)	$\mathcal{B}$ = 3.808 ± 0.051	$\mathcal{B}$ = 3.964 ± 0.070	$\mathcal{B}$ = 3.750 ± 0.059

Binning Scheme 1 coincides with the one shown in Fig. 5.29, while the other binning schemes can be found in Fig. 5.35. The selected central value is $\mathcal{B}(\Lambda \rightarrow p\mu^{-}\bar{\nu}_{\mu})$ =(3.845 ± 0.059 (stat)) × 10^{-4} (blinded) and the systematic uncertainty is determined by considering the largest deviation from the results obtained with other binning schemes and modes, obtaining 5.1 %.

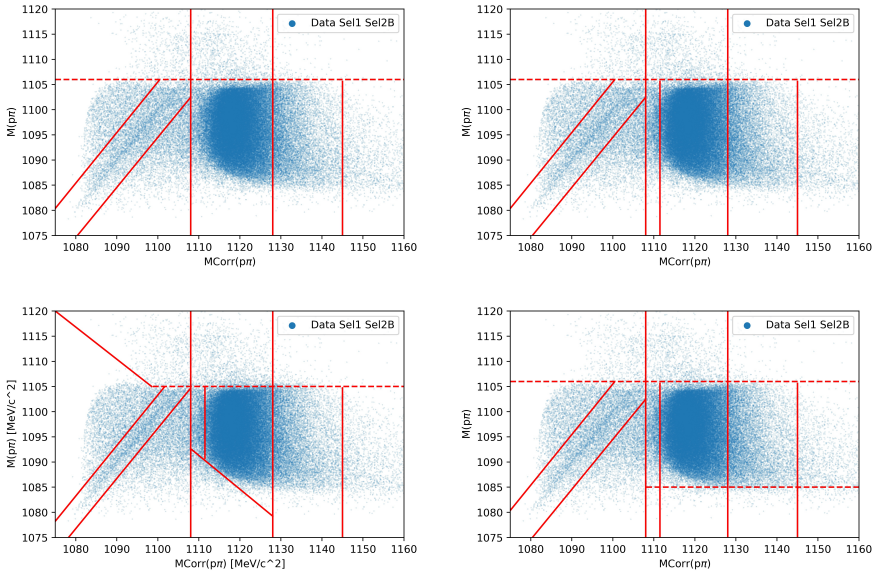

FIGURE 5.35: Proposed binnings of the $MCorr(p\pi)$ vs $M(p\pi)$ plane to perform a bi-dimensional fit. Top left is Binning Scheme 2, Top Right Binning Scheme 3, Bottom left is Binning Scheme 4 and Bottom Right Binning Scheme 5. Binning Scheme 4 was selected to be the default, since its diagonal bin is tighter and more sensitive to the Signal behaviour.

5.8.3.1 1-DIMENSIONAL FIT CHECK

Even though the background MC statistics are insufficient to perform a fully valid fit in 1D, we can still conduct a fit in $MCorr(p\pi)$ as a check. This is possible because the background distribution in that variable exhibits a satisfactory agreement with a double-sided Crystal Ball PDF, allowing us to model the background accurately.

The blinded branching ratio result with the signal yield extracted from this fit is $\mathcal{B}(\Lambda \to p\mu^-\bar{\nu}_\mu) = (4.02 \pm 0.18) \times 10^{-4}$, in good agreement with the 2-dimensional fit result.

The 1D fit of the $MCorr(p\pi)$ distribution can be seen in Fig. 5.36.

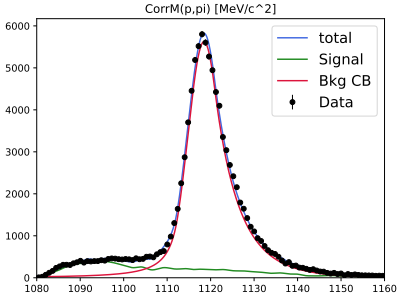

FIGURE 5.36: A 1D fit of the $MCorr(p\pi)$ distribution is performed to extract the signal yield in the Signal Line region after the selection. The background component is fitted using a double-sided Crystal Ball PDF, while the signal component is modeled using a Kernel Density Estimation (KDE).

5.9 SYSTEMATIC UNCERTAINTIES

The entire analysis was structured with the primary goal of minimizing systematic uncertainties. It employs TISTISTIS Data for both the NormLine and SignalLine, ensuring that the cuts used in the Stripping lines are consistent across both lines. The only difference lies in the PID criteria for muons and pions. Furthermore, these PID cuts have been minimized to the extent possible, with the selection completely basaed on kinematic requirements. As a result, this approach should lead to the cancellation of most systematic uncertainties.

As we are using $\Lambda \rightarrow p\pi^-$ as normalisation, we should include its branching ratio uncertainty as systematic uncertainty.

Regarding PidCalib2 and TrackCalib2, the software packages used to correct the MC efficiencies for the Stripping lines PID and tracking cuts, results are affected by the chosen binning. To take into account this systematic source of uncertainty, we can estimate how the obtained efficiency varies by changing the binning scheme. The choosen binning schemes and results can be found in the appendices (A.11).

The systematic uncertainty associated with the signal yield fit, which is the predominant factor, was previously detailed in Section 5.8.3. This uncertainty, 5.1 %, could potentially be reduced to 3.64 % if the third mode, accounting for the presence of combinatorial background, were excluded. As discussed earlier, the expected contribution of combinatorial background is minimal. However, we chose to incorporate a "combinatorial background" sample into the fitting process. This sample, despite being dominated by mismatched $\Lambda \rightarrow p\pi^-$, was the unique method to assess the impact of this background.

It's important to note that the presence of $\Lambda \rightarrow p\pi^-$ within the combinatorial background sample is not inherently problematic. In principle, there is no issue in fitting the $\Lambda \rightarrow p\pi^-$ contribution to the selected data using one sample instead of the other, as the total $\Lambda \rightarrow p\pi^-$ count will ultimately be determined by combining both samples. The issue primarily arises from fitting a portion of the $\Lambda \rightarrow p\pi^-$ contribution using a sample with significantly fewer statistics. This discrepancy leads to a more pronounced difference in the results and contributes to an increased systematic uncertainty..

The determination of the final systematic uncertainty for TrackCalib2 is currently a Work In Progress (WIP). Additionally, other potential sources of systematic uncertainty are under consideration (refer to Table 5.23). However, their contribution to the overall systematic uncertainty is anticipated to be minimal.

The total systematic uncertainty is anticipated to be approximately 6.0 %, without any significant variations expected.

TABLE 5.23: Systematic uncertainties that affect the $\mathcal{B}(\Lambda \to p\mu^- \bar{\nu}_\mu)$ measurement.

Source	**Relative Uncertainty (%)**
$\mathcal{B}(\Lambda \to p\pi^-)$	0.78 %
NormLine Fit	expected to be negligible
PidCalib Signal Line	1.61 %
PidCalib NormLine	1.04 %
Tracking	$\approx$ 1.0 % (WIP)
$\Lambda \to p\mu^- \bar{\nu}_\mu$ yield (fit)	5.1 %
Signal fit template	expected to be negligible
Other sources	-

CHAPTER 6

RESULTS AND CONCLUSIONS

THE AIM OF THIS THESIS is to precisely measure $\mathcal{B}(\Lambda \to p\mu^-\bar{\nu}_\mu)$ and test lepton flavour universality in $s \to u$ transitions. Any deviation from LFU would indicate the presence of new beyond the Standard Model physics. With this purpose, data from the LHCb, produced through proton-proton collisions at the LHC with a centre-of-mass energy of 13 TeV, collected during its second data taking period (2016-2018), is analyzed.

6.1 RESULTS

In 2021, BESIII published the first measurement of the absolute branching fraction of $\Lambda \to p\mu^-\bar{\nu}_\mu$, obtaining the best branching fraction measurement till the date, $\mathcal{B}(\Lambda \to p\mu^-\bar{\nu}_\mu)) = (1.48 \pm 0.21) \times 10^{-4}$ [6].

Our measured blinded result, $\mathcal{B}(\Lambda \to p\mu^-\bar{\nu}_\mu) = (3.485 \pm 0.059(\text{stat}) \pm 0.23(\text{syst})) \times 10^{-4}$, shows a significantly reduced uncertainty. We should consider that this blinded result ought to be divided by the blinding constant, which is expected to be approximately equal to the ratio of our value to the measured $\mathcal{B}(\Lambda \to p\mu^-\bar{\nu}_\mu)$ result. It should also be noted that the calculation of the systematic uncertainty is not completely finalized, so the final result of this uncertainty may vary slightly.

6.2 CONCLUSIONS

The BESII result has an uncertainty of 14.19%. With this selection and the fit result, we anticipate a statistical uncertainty of 1.5% and a systematic uncertainty of 6.0%. This implies a total uncertainy of 6.2% and aligns with our goal of achieving the most precise measurement of the $\mathcal{B}(\Lambda \to p\mu^-\bar{\nu}_\mu)$ using LHCb data.

Regarding V_{us}, we have derived its dependence on $\mathcal{B}(\Lambda \to p\mu^-\bar{\nu}_\mu)$

$$|V_{us}|^2 \simeq \frac{\mathcal{B}^{\mathrm{SM}}(B_1 \to B_2\mu^-\bar{\nu}_\mu)\ (4.652 \pm 0.035) \times 10^{-12}}{(1.06 \times 0.06) \times 10^{-14}} = \mathcal{B}^{\mathrm{SM}}(B_1 \to B_2\mu^-\bar{\nu}_\mu)\cdot(437\pm26)$$

with the achieved uncertainty in $\mathcal{B}(\Lambda \to p\mu^-\bar{\nu}_\mu)$ and using the BESIII measurement as central value, our V_{us} derivation is $V_{us} \simeq 0.254 \pm 0.011$

This result also has important consequences in the ratio between the muonic and electron mode, $R^{\mu e}$. This LFU observable is predicted by theory to be $R^{\mu e} = 0.153 \pm 0.008$ working at next-to-leading order [26]. Considering that the electron mode has already been measured precisely, $\mathcal{B}(\Lambda \to pe^-\bar{\nu}_e) = (8.34 \pm 0.14) \times 10^{-4}$ [78], the achieved precision in $\mathcal{B}(\Lambda \to p\mu^-\bar{\nu}_\mu)$ could be enough to find a sensitive deviation with the SM prediction.

To provide some examples, a measurement with the BESIII central value and our uncertainty ($R^{\mu e}_{\mathrm{exp}} = 0.177 \pm 0.011$) will imply a 1.8 σ deviation with the SM prediction, and an unblinded central value of 1.84×10^{-4} with our uncertainty will lead to a 5 σ deviation.

This analysis opens the door for starting a extensive campaign measuring semileptonic hyperon decays branching ratios at LHCb, being $\Xi^- \to \Lambda\mu^-\bar{\nu}_\mu$ the most promising one to start with. Its branching ratio has an uncertainty at the 100 % level and having a bigger mass difference between the mother and daughter baryons make it more suitable for using our strategy for separating the SHD from the combinatorial background using the longitudinal neutrino momentum.

This result shows again that LHCb is a versatile detector that can obtain leading measurements even besides its original purpose. The LHCb collaboration has already published the world's most precise measurement in $K^0_S \to \mu^+\mu^-$, $K^0_S \to \mu^+\mu^-\mu^+\mu^-$, and $\Sigma^+ \to p\mu^+\mu^-$ [2] [4], [3]. This $\mathcal{B}(\Lambda \to p\mu^-\bar{\nu}_\mu)$ measurement will enlarge the list of leading strange measurements performed by our collaboration.

CHAPTER 7

RESUMO

7.1 INTRODUCIÓN

O modelo estándar (SM) é o marco teórico que describe as partículas fundamentais observadas ate o momento e as súas interaccións a través de tres das catro interaccións fundamentais: a electromagnética, a feble e a forte.

No SM, a materia está composta por partículas con número cuántico de spin semienteiro chamadas fermións. Por outra banda, as interaccións están mediadas por partículas con número cuántico de spin enteiro, chamadas bosons.

Existen dous tipos de fermións, os leptons e os quarks. En ambas categorías observamos o mesmo patrón, con dous tipos de partículas (quarks up e down nos quarks e electron e neutrino electrónico no leptons) e dúas copias máis pesadas destes dobretes de partículas.

Desde un punto de vista matemático, a simetría Gauge electro-feble $SU(2)_W \times U(1)_Y$ é quiral e, como consecuencia, os quarks e os leptóns organízanse en tres dobretes con quiralidade a esquerdas: Q_L^i con i=1,2,3, onde $Q_L^1=\begin{pmatrix} u_L \\ d_L \end{pmatrix}$, $Q_L^2=\begin{pmatrix} c_L \\ s_L \end{pmatrix}$, $Q_L^3=\begin{pmatrix} t_L \\ b_L \end{pmatrix}$ e L_L^i with i=1,2,3, where $L_L^1=\begin{pmatrix} \nu_{e_L} \\ e_L \end{pmatrix}$, $L_L^2=\begin{pmatrix} \nu_{\mu_L} \\ \mu_L \end{pmatrix}$, $L_L^3=\begin{pmatrix} \nu_{\tau_L} \\ \tau_L \end{pmatrix}$. Por outra banda, os correspondentes singletes a dereitas son u_R, d_R, c_R, s_R, t_R and b_R nos quarks e e_R, μ_R, τ_R nos leptons. Paga a pena resaltar que, polo que sabemos ata agora, non existen neutrinos a dereitas.

Os quarks, en contraste cos leptóns, vense afectados pola interacción forte, que está mediada por gluóns e que os confina tipicamente en parellas de quarks (mesons) ou tripletes de quarks (barións).

O fotón é o mediador da forza electromagnética e os bosóns $W^{\pm}$ e Z^0 son os mediadores da interacción feble. No SM as partículas carecen de masa nunha orixe e adquírena mediante a súa interacción co campo de Higgs. Ca descuberta no ano 2012 polas colaboracións CMS e ATLAS no LHC, o modelo estándar completouse.

7.1.1 ESTRUTURA DE SABOR DO SM

Existen seis tipos de quarks e seis tipos de leptóns. Cada tipo é considerado un sabor diferente. O sabor consérvase nas interaccións fortes e electromagnéticas. Pero, a través de correntes cargadas febles, os quarks e os leptóns poden mudar dun sabor a outro. Un exemplo básico é o decaemento beta dos nucleos atómicos, onde un neutrón decae a un protón, un electrón e un anti-neutrino. En realidade, o proceso fundamental que está tendo lugar é

$$d \rightarrow u\, e^{-}\, \overline{\nu}_e$$

onde o quark d decae a un quark up un electrón e un anti-neutrino electrónico a través do intercambio dun bosón W^{-}. Este decaemento é análogo ao que estudaremos nesta tese $\Lambda \rightarrow p\mu^{-}\bar{\nu}_{\mu}$. A diferenza ven de que no noso caso estudamos unha transición $s \rightarrow u$ e en que os leptóns no estado final pertenzen á segunda xeración.

No SM podemos escoller unha base de sabor invariante gauge onde só un dos dous acopoplos de Yukawa é diagonal. Podemos escoller $Y^d = diag(y_d, y_s, y_b)$ e $Y^u = V^{+} \times diag(y_u, y_c, y_t)$ ou $Y^d = V \times diag(y_d, y_s, y_b)$ e $Y^u = diag(y_u, y_c, y_t)$, onde V é a matriz unitaria.

Para diagonalizar tamén a segunda matriz necesitamos rotar separadamente u_L e d_L, así que non temos unha base invariante gauge. Esta matriz V aparece nas interaccións gauge de correntes cargadas.

Estas interaccións de corrente cargada, mediadas por un bosón $W^{\pm}$, poden escribirse como

$$J^{\mu}_{W} = \frac{-g}{\sqrt{2}}\, \overline{u}_L\, \gamma^{\mu} W^{+}_{\mu}\, V_{CKM}\, d_L + h.c.$$

o que basicamente significa que as interaccións febles acóplanse a parellas $\begin{pmatrix} u \\ d' \end{pmatrix}$, $\begin{pmatrix} c \\ s' \end{pmatrix}$ e $\begin{pmatrix} t \\ b' \end{pmatrix}$, onde d', s' e b' son combinacións lineais dos estados físicos d, s, b:

$$\begin{pmatrix} d' \\ s' \\ b' \end{pmatrix} = \begin{pmatrix} V_{ud} & V_{us} & V_{ub} \\ V_{cd} & V_{cs} & V_{cb} \\ V_{td} & V_{ts} & V_{tb} \end{pmatrix} \begin{pmatrix} d \\ s \\ b \end{pmatrix}$$

Esta mestura non trivial xorde exclusivamente do sector de Higgs. Só as interaccións mediadas por $W^{\pm}$ e as interaccións co bosón de Higgs son física de sabor. A rotación do sector dereito non é observabél e as correntes neutras permanecen diagonais en sabor.

A matriz unitaria de mestura de quarks 3×3 en cuestión denomínase matriz CKM, como honra a Cabibbo, Kobayashi e Maskawa. Orixinalmente, Cabibbo propuxo esta estrutura de matriz para dúas xeracións en 1963. Unha década despois, Kobayashi e Maskawa ampliaron esta formulación para acomodar tres xeracións. Esencialmente, a matriz CKM encapsula información sobre a intensidade das interaccións febles que cambian de sabor. Cada elemento da matriz tradúcese na amplitude de probabilidade para unha transición dun sabor de cuark j a outro sabor de cuark i. As probabilidades

destas transicións son proporcionais a $|V_{ij}|^2$. Deste xeito, unha medida do $\mathcal{B}(\Lambda \to p\mu^-\bar{\nu}_\mu)$ implica tamén unha medida do elemento da matriz CKM V_{us}.

Unha das características máis relevantes da matriz CKM é a súa unitariedade ($(V_{CKM}^\dagger V_{CKM})_{ij} = (V_{CKM}V_{CKM}^\dagger)_{ij} \equiv \delta_{ij}$). Observar unha desviación da unitariedade sería un síntoma de física alén do SM, como a presenza dunha cuarta xeración, estando isto en conflicto cas observacións actuais que claramente indican que só existen 3 xeracións.

Ata o de agora, en contraste co que acontece cos quarks, sempre observamos consistentemente que o número leptónico, ou número de xeración leptónica, sempre se conserva nos decaementos de partículas. Por exemplo, no caso $\Lambda \to p\mu^-\bar{\nu}_\mu$ non é preciso medir o sabor do anti-neutrino no estado final pra saber que é de tipo muónico, xa que ó numero leptónico no estado inicial é o.

Mentres que as interaccións dos quarks co bosón $W^\pm$ dependen do seu sabor, vindo rexidas pola matriz CKM, todos os leptóns cargados interactúan co bosón W nas interaccións febles uniformemente, sen importar o seu sabor. A isto chámaselle Universalidade Leptónica (LFU) e é notabél considerando as significativas diferenzas de masa entre os leptóns.

Esta universalidade emerxe naturalmente da estrutura do SM, particularmente da forma en que os leptóns se acoplan aos bosóns W e Z. Na esencia, as constantes de acoplamento que gobernan a intensidade da interacción entre os leptóns e estes bosóns permanecen uniformes para cada sabor de leptón. Isto é o que leva á predición de que os procesos febles deberían mostrar esta universalidade a través dos sabores dos leptóns. As probas experimentais da LFU tipicamente implican comparar as taxas de procesos como desintegracións ou dispersións entre diferentes sabores de leptóns e buscar desviacións das relacións esperadas.

Calquera desviación observada na LFU implicaría a descuberta de física mais alá do SM (BSM), que precisaría ser explicada con novas partículas como os leptoquarks ou modelos cun dobrete de dous Higgs.

No contexto do noso decaemento semileptónico de hyperon ($\Lambda \to p\mu^-\bar{\nu}_\mu$), o observábel

$$R^{\mu e} = \frac{\Gamma(B_1 \to B_2\mu^-\bar{\nu}_\mu)}{\Gamma(B_1 \to B_2 e^-\bar{\nu}_e)},$$

é sensíbel a violacións na LFU, xa que os acoplos aos leptóns cargados dos bosóns gauge son idénticos no SM, vindo a única diferenza nas taxas de desintegración da diferenza nas masas dos leptóns.

7.1.2 DECAEMENTOS SEMILEPTÓNICOS DE HYPERONS (SHD)

Os hyperóns son aqueles barións compostos por, polo menos, un quark s e ningún quark máis pesado, sendo a partícula Λ (uds) o hyperón máis lixeiro. QCD, a teoría que descrebe no SM a interacción forte, presenta un simetría de sabor SU(3). Esta simetría é exacta en QCD e permite intercambiar os sabores dos quarks sen consecuencias. Considerando os quarks confinados dentro de hadróns, poderíamos intercambiar os diferentes sabores de quarks sen alterar nada. aínda así, esta simetría non é exacta debido ás diferentes masas dos quarks.

Cando reparamos no espectro de masas dos quarks podemos observar que os quarks u, d e s presentan masas significativamente menores que as do resto de quarks. Por isto, a escalas de enerxías onde a interacción forte é a predominante, a diferenza entre as masas dos quarks u, d e s é suficientemente pequena como para consideralos case intercambiabéis en termos das dinámicas de QCD. Isto implica unha simetría de sabor SU(3) aproximada, que é especialmente interesante para os hyperóns.

No SM, o lagranxiano responsabél da transición de quarks $s \to u$ durante o decaemento semileptónico dun barión a outro barión a un leptón (l) e un antineutrino ($\bar{\nu}_l$), orixínase do termo de interacción feble do lagranxiano do SM. Este termo particular pertence ás correntes cargadas mediados polos bosóns $W^{\pm}$.

Pra enerxías muito menores que a escala de ruptura da simetría electro-feble, que ven dada por $v = (\sqrt{2}G_F)^{1/2} \approx 246$ GeV, todos os procesos con correntes cargadas que incluen quarks up e strange poden ser explicadoss pola interacción de catro corpos de Fermi (V - A) × (V - A). O lagranxiano efectivo sen considerar contribucións BSM é:

$$\mathcal{L} = -\frac{G_F V_{us}}{\sqrt{2}} \sum_{l=e,\mu} [\bar{l}\gamma_\mu(1-\gamma_5)\nu_l].[\bar{u}\gamma_\mu(1-\gamma_5)s] + h.c.$$

Debemos ter en conta que esta non é puramente unha transición $s \to u$, xa que a transición acontece dentro dun ambiente bariónico. Nun decaemento semileptónico de hyperón xenérico ($B_1(p_1) \to B_2(p_2)l^-(p_l)\bar{\nu}_l(p_\nu)$) podemos separar os elementos de matriz leptónicos e bariónicos. As correntes hadrónicas son parametrizadas con factores de forma, sendo a corrente axial:

$$\langle B_2(p_2)|\bar{u}\gamma_\mu s|B_1(p_1)\rangle = \bar{u}_2(p_2)\Big[f_1(q^2)\gamma_\mu + \frac{f_2(q^2)}{M_1}\sigma_{\mu\nu}q^\nu + \frac{f_3(q^2)}{M_1}q_\mu\Big]u_1(p_1)$$

e a corrente vectorial hadrónica:

$$\langle B_2(p_2)|\bar{u}\gamma_\mu\gamma_5 s|B_1(p_1)\rangle = \bar{u}_2(p_2)\Big[g_1(q^2)\gamma_\mu + \frac{g_2(q^2)}{M_1}\sigma_{\mu\nu}q^\nu + \frac{g_3(q^2)}{M_1}q_\mu\Big]\gamma_5 u_1(p_1)$$

onde $u_{1,2}$ e $M_{1,2}$ son as amplitudes de spinor e masas de $B_{1,2}$ respectivamente, q é o momento transferido ao par leptónico ($q = p_1 - p_2$) e $\sigma_{\mu\nu} = [\gamma_\mu, \gamma_\nu]/2$. .

A simetría de sabor aproximada SU(3) presente nos hyperóns regula o espazo de fases dos decaementos e permite unha expansión sistemática dos observábeis baseada no parámetro xenéricp que goberna a ruptura de simetría

$$\delta = \frac{M_1 - M_2}{M_1}$$

Expandido en δ até next-to-leading order (NLO) e desprezando m_e, a taxa de desintegración integrada de ($B_1 \to B_2 e^- \bar{\nu}_e$) indo até orde δ^2 ven dada por

$$\Gamma^{\mathrm{SM}}(B_1 \to B_2 e^- \bar{\nu}_e) \simeq \frac{G_F^2 |V_{us}\, f_1(0)|^2 \Delta^5}{60\pi^3}\Big[\big(1-\frac{3}{2}\delta\big) + 3\big(1-\frac{3}{2}\delta\big)\frac{g_1(0)^2}{f_1(0)^2} - 4\delta\frac{g_2(0)}{f_1(0)}\frac{g_1(0)}{f_1(0)}\Big]$$

Física BSM pode contribuir aos acoplos do SM, sendo o lagranxiano efectivo máis xeral:

$$\mathcal{L} = -\frac{G_F V_{us}}{\sqrt{2}}(1+\epsilon_L+\epsilon_R)\times\sum_{l=e,\mu}[\bar{l}\gamma_\mu(1-\gamma_5)\nu_l.\bar{u}[\gamma_\mu-(1-2\epsilon_R)\gamma_\mu\gamma_5]s + \bar{l}(1-\gamma_5)\nu_l.\bar{u}[\epsilon_S-\epsilon_P\gamma_5]s+\epsilon_T\bar{l}\sigma_{\mu\nu}(1-\gamma_5)s] + h.c.$$

Un observábel que permite testear a LFU pódese definir como o ratio entre os modos muónico e electrónico

$$R^{\mu e} = \frac{\Gamma(B_1\longrightarrow B_2\mu^-\bar{\nu}_\mu)}{\Gamma(B_1\longrightarrow B_2 e^-\bar{\nu}_e)}$$

é sensíbel a contribucións BSM. É importante resaltar que nesta fraccións a dependencia nos factores de forma simplifícase. Traballando a NLO, chegamos a:

$$R^{\mu e}_{\mathrm{SM}} = \sqrt{1-\frac{m_\mu^2}{\Delta^2}}\left(1-\frac{9}{2}\frac{m_\mu^2}{\Delta^2}-4\frac{m_\mu^4}{\Delta^4}\right)+\frac{15}{2}\frac{m_\mu^4}{\Delta^4}\operatorname{arctanh}\left(\sqrt{1-\frac{m_\mu^2}{\Delta^2}}\right)$$

onde $\Delta = M_2 - M_1$.

Este LFU test está predito pola teoría cunha precisión notábel, $R^{\mu e} = 0.153 \pm 0.008$. Esta predicción tamén se destaca porque a este nivel de precisión teórica ($O(\frac{(M_1-M_2)^2}{M_1^2})$) a fracción non depende dos factores de forma.

A fracción dos observábeis SM e BSM é

$$\frac{R^{\mu e}_{\mathrm{NP}}}{R^{\mu e}_{\mathrm{SM}}} = 1 + r_S\epsilon_S + r_T\epsilon_T$$

dependendo fortemente a sensitividade dos SHD aos coeficientes de Wilson da canle SHD.

A taxa de decaemento do modo muónico pódese expresar como:

$$\Gamma^{\mathrm{SM}}(B_1\longrightarrow B_2\mu^-\bar{\nu}_\mu)\simeq\frac{G_F^2|V_{us}\,f_1(0)|^2\Delta^5}{60\pi^3}\left[\left(1-\frac{3}{2}\delta\right)+3\left(1-\frac{3}{2}\delta\right)\frac{g_1(0)^2}{f_1(0)^2}-4\delta\frac{g_2(0)}{f_1(0)}\frac{g_1(0)}{f_1(0)}\right]\left(\sqrt{1-\frac{m_\mu^2}{\Delta^2}}\left(1-\frac{9}{2}\frac{m_\mu^2}{\Delta^2}-4\frac{m_\mu^4}{\Delta^4}\right)+\frac{15}{2}\frac{m_\mu^4}{\Delta^4}\operatorname{arctanh}\left(\sqrt{1-\frac{m_\mu^2}{\Delta^2}}\right)\right)$$

7.1.3 MOTIVACIÓN DESTA MEDIDA

Nas últimas décadas o foco estivo no sector de maior masa da matriz CKM. A pesar disto, é no sector de baixa masa, V_{ud} e V_{us}, onde se pode acadar unha maior precisión e un test máis preciso da unitariedade da matriz CKM. Esta unitariedade implica

$$|V_{ud}|^2 + |V_{us}|^2 + |V_{ub}|^2 \equiv 1$$

Dado que a contribución do elemento $|V_{ub}|^2$ é practicamente desprezábel (aproximadamente 1.3×10^{-5}), esta relación redúcese á universalidade de Cabibbo ($|V_{ud}| \approx cos\ \theta_{12}$, $|V_{us}| \approx sin\ \theta_{12}$).

Xa que $|V_{ud}|$ foi medido xa con grande precisión, cun valor de $|V_{ud}| = 0.97436 \pm 0.00016$, o foco móvese a V_{us}.

De feito, empregando as mellores medidas de V_{ud}, V_{us} e V_{ub} obtemos

$$|V_{ud}|^2 + |V_{us}|^2 + |V_{ub}|^2 = 0.9985 \pm 0.0007$$

mostrando unha tensión de 2.2σ ca unitariedade na primeira ringleira da matriz CKM.

Ademais, as medidas de V_{us} en decaementos leptónicos ($K_{\mu 2}$) e semileptónicos (K_{l3}) de kaóns mostran unha discrepancia de 3σ. Esta diferenza pode ser un indicio de BSM. Tendo isto en conta, tórnase vital atopar outros xeitos de medir V_{us} de forma precisa. Os SHD son unha alternativa prometedora.

Pero o maior interese dos SHD é que son un excelente marco de estudo pra investigar a LFU. Desde un punto de vista teórico, demostrouse que os SHD poden ser sensíbeis a dinámicas BSM que rompen a universalidade leptónica. Estes decaementos están controlados por un pequeno parámetro de ruptura de simetría δ que permite expansións sistemáticas e predicións precisas. Os modos muónicos son especialmente sensíbeis a contribucións BSM.

No caso de $\Lambda \to p\mu^- \bar{\nu}_\mu$, o observábel de LFU test está predito pola teoría como $R^{\mu e} = 0.153 \pm 0.008$ traballando a next-to-leading order. A mellor medida deste observábel foi realizada por BESIII no 2021, obtendo $R^{\mu e} = 0.178 \pm 0.028$, consistente dentro das incertezas ca predicción.

aínda así, considerando que o modo electrónico foi medido cunha maior precisión $\mathcal{B}(\Lambda \to pe^- \bar{\nu}_e) = (8.34 \pm 0.14) \times 10^{-4}$, a maior parte da incerteza ven da medida de BESIII do modo muónico, $\mathcal{B}(\Lambda \to p\mu^- \bar{\nu}_\mu) = [1.48 \pm 0.21, (\text{stat}) \pm 0.08, (\text{syst})] \times 10^{-4}$.

Aumentar a precisión en $\mathcal{B}(\Lambda \to p\mu^- \bar{\nu}_\mu)$ é esencial para probar a universalidade leptónica en transicións $s \to u$.

7.2 CONDICIÓNS EXPERIMENTAIS

O LHC é o maior e máis potente acelerador de partículas do mundo. Consiste nun anel de 27 km de circunferencia, composto dunha serie de elementos pra acelerar e manter en órbita as partículas. Dentro do acelerador, dous feixes de partículas de alta enerxía viaxan en direccións opostas. Os feixes fanse colidir en catro puntos de interacción correspondentes a catro detectores ATLAS, CMS, ALICE e LHCb.

LHCb é un dos catro grandes detectores recollendo datos no LHC. O seu nome provén do principal propósito pra o que foi pensado, detectar os decaementos de partículas contendo quarks b. Estas partículas, formadas nas colisións de protóns do LHC, tenden a xerarse e a decaer sen alonxarse moito da dirección de incidencia do feixe. Isto refléxase na forma do detector que non cubre todo o ángulo sólido ao redor

da interacción, senón que se extende na dirección "cara adiante" cunha aceptancia en pseudorapidity de $1.6 \leq \eta \leq 4.9$.

LHCb está composto de diferentes subdetectores. Basicamente dispomos dun localizador de vértices (**VELO**) (pra determinar a traxectoria das partículas perto do punto de interacción co obxetivo de separar os puntos onde as partículas son xeradas (PV) de onde decaen (SV), un detector chamado **RICH** (pra identificar que tipo de partícula produce cada traza a partir da súa masa e carga), **T-stations** (que nos permiten obter a traxectoria e momento das partículas cargadas), **ECAL** (que detecta electróns e fotóns e mide a súa enerxía), **HCAL** (que mide a enerxía depositada dos hadrons e **Muon Chambers** (situadas ao final do detector pra detectar muóns).

Esta análise emprega datos recollidos no LHCb durante o Run 2 (2016-2018).

7.3 ANÁLISE

A análise principal desta tese é a medida do $\mathcal{B}(\Lambda \rightarrow p\mu^-\bar{\nu}_\mu)$. O maior desafío relacionado con esta medida en LHCb é discriminar o sinal de outras canles que pican en certas masas, principalmente $\Lambda \rightarrow p\pi^-$ e $K^0_S \rightarrow \pi^+\pi^-$. Ademais destes fondos, o fondo combinatorio tamén nos crea problemas, xa que no sinal temos un neutrino e polo tanto momento perdido no estado final. Isto fai que as distribucións de $\Lambda \rightarrow p\mu^-\bar{\nu}_\mu$ poden resultar parecidas ás do fondo combinatorio. Na análise empréganse só trazas tipo long, xa que non estamos limitados pola estatística e estas presentan unha mellor resolución.

O $\mathcal{B}(\Lambda \rightarrow p\mu^-\bar{\nu}_\mu)$ obterase empregando como input o $\mathcal{B}(\Lambda \rightarrow p\pi^-)$. $\Lambda \rightarrow p\pi^-$ será a súa vez a canle de normalización.

Polo tanto, podemos definir un parámetro α que relaciona o $\mathcal{B}(\Lambda \rightarrow p\mu^-\bar{\nu}_\mu)$ co número de eventos de sinal reconstruídos $N^{reco}_{p\mu\nu}$,

$$\mathcal{B}(\Lambda \rightarrow p\mu^-\bar{\nu}_\mu) = \alpha N^{reco}_{p\mu\nu}$$

sendo

$$\alpha = \frac{\mathcal{B}(\Lambda \rightarrow p\pi^-)}{N^{reco}_{p\pi}} \frac{\epsilon_{p\pi}}{\epsilon_{p\mu\nu}}$$

Dúas Stripping lines (selección offline) foron escritas con este propósito, a de normalización (NormLine) pra seleccionar $\Lambda \rightarrow p\pi^-$ e medir a súa producción en LHCb e a de sinal (SignalLine) pra facer o mesmo co $\Lambda \rightarrow p\mu^-\bar{\nu}_\mu$. Ambas seleccións comparten o mesmos cortes pra reducir os sistemáticos, ca única diferenza nos cortes de ID e na xanela de masas.

Dispomos de simulación (MC) de MinBias pra 2018 MD and 2018 MU, e producións de $\Lambda \rightarrow p\pi^-$ e $\Lambda \rightarrow p\mu^-\bar{\nu}_\mu$ MC pasando a SignalLine pra 2016, 2017 e 2018 cas configuracións Magnet Up e Magnet Down. A producción de $\Lambda \rightarrow p\mu^-\bar{\nu}_\mu$ foi xerada empregando un modelo de EvtGen desenvolto como parte desta tese e que ten en conta a taxa de decaemento diferencial do sinal. O modelo foi escrito de xeito que poida ser empregado no futuro pra calquera SHD.

7.3.1 FIT DA CANLE DE NORMALIZACIÓN

O primeiro paso é eliminar a contaminación de $K_S^0 \to \pi^+\pi^-$ presente na NormLine. Pra isto podemos aplicar o seguinte corte (Cut 1 | Cut 2) no plano de Armenteros-Podolanski, onde os cortes son:

$$\text{Cut 1} : QPT > \left(25.2 + \sqrt{(25.2)^2 - 4.\left(25^2 - 200^2.\left(1 - \frac{\alpha^2}{0.815^2}\right)\right)}\right)/2$$

$$\text{Cut 2} : QPT < \left(25.2 + \sqrt{(25.2)^2 - 4.\left(25^2 - 130^2.\left(1 - \frac{\alpha^2}{0.815^2}\right)\right)}\right)/2$$

Unha vez eliminado o $K_S^0 \to \pi^+\pi^-$ (este corte aplícase a MC e datos pasando a NormLine a partir deste momento), podemos proceder co fit, onde a pdf total está composta dunha double sided crystal ball + exponencial. Comezamos cun fit do $\Lambda \to p\pi^-$ MC puro, pra extraer os catro valores das colas da función double sided crystal ball.

A continuación procedemos a facer o fit dos datos da NormLine, onde se aplicou o corte pra eliminar $K_S^0 \to \pi^+\pi^-$ previamente, fixando os valores das colas obtidos no paso anterior. Isto danos o número de $\Lambda \to p\pi^-$ nos datos que pasaron a NormLine.

Por último, repetimos este fit a todo o MinBias MC que pasa a NormLine, pra obter a eficiencia do $\Lambda \to p\pi^-$ de reconstrucción + pasar a NormLine ($\epsilon^{NormLine}_{\Lambda\to p\pi^-}$), dividindo o número de $\Lambda \to p\pi^-$ no fit entre o número total de $\Lambda \to p\pi^-$ no MC sample previo á reconstrucción.

Dividindo o número de $\Lambda \to p\pi^-$ nos datos que pasaron a NormLine entre $\epsilon^{NormLine}_{\Lambda\to p\pi^-}$ obtemos o número de sucesos de $\Lambda \to p\pi^-$ en LHCb no Run 2. Podemos dividir este numero entre $\mathcal{B}(\Lambda \to p\pi^-)$ pra saber o número total de partículas Λ xeradas en LHCb no Run2.

7.3.2 EFICIENCIA DE SELECCIÓN DO SINAL

O seguinte paso será obter a eficiencia do sinal, o último valor que precisamos pra calcular o parámetro α. Esta eficiencia encapsula os procesos de reconstrucción, stripping e selección.

Neste caso a selección está baseada nun corte no plano momento transverso perdido vs masa ca hipótese protón-muón ($\not{p}_T$ vs $M(p\mu)$, motivados por unha estratexia quinemática que permite recuperar a información de momento do neutrino:

$$\text{Sel1} = \left(\not{p}_T > 16\right) \,\&\, \left(M(p,\mu) < (1116.3 - 1.03\not{p}_T)\right) \,\&\, \left(M(p,\mu) > (1122.683 - 2\not{p}_T)\right)$$

e un corte seleccionando os eventos que caen nas rexións do plano de Armenteros onde a sinal presenta maior pureza.

A eficiencia desta selección obtense aplicando os cortes á simulación de $\Lambda \to p\mu^-\bar{\nu}_\mu$ pasando a SignalLine. Esta eficiencia debera ser multiplicada pola eficiencia de xeración, reconstrucción e stripping, que podemos obter directamente dos rexistros da producción oficial de LHCb.

Unha vez calculada esta eficiencia, dispomos de todos os elementos precisos pra calcular o parámetro α.

7.3.3 CORRECCIÓN DAS EFICIENCIAS

O cálculo das eficiencias que entran no parámetro α parten de supor que a simulación reproduce de forma fiabél os datos. Pero isto pode non ser así, especialmente no relacionado á resposta fronte aos cortes de PID e tracking. Por este motivo, procedemos a correxir estes valores empregando as ferramentas de LHCb PidCalib e TrackCalib.

Unha vez aplicadas estas correccións, tanto ás efiencias de normalización como de sinal, obtemos un valor de α correxido e fiabél.

7.3.4 FIT POST SELECCIÓN DO SINAL

O último paso é obter o número de eventos de $\Lambda \to p\mu^-\bar{\nu}_\mu$ nos datos que pasan a SignalLine seleccionados. Dada a dificuldade pra obter MC de $\Lambda \to p\pi^-$ e fondo combinatorio pasando a selección, decidimos facer un fit 2D pra mitigar o problema de baixa estatística de MC.

Este fit faise no plano $MCorr(p,\pi)$ vs $M(p,\pi)$, onde $MCorr(p,\pi)$ é unha variable creada supondo que o pión decae posteriormente a un muón e un antineutrino. Este plano permite separar de xeito satisfactorio $\Lambda \to p\pi^-$, $\Lambda \to p(\pi^- \to \mu^-\bar{\nu}_\mu)$ e $\Lambda \to p\mu^-\bar{\nu}_\mu$. Pra verificar o resultado e obter a incerteza sistemática asociada, empregamos diferentes bineados e modos de fit. Os resultados mostran unha boa compatibilidade entre eles e cun fit 1D na variable $MCorr(p,\pi)$. aínda así, a maior parte da incerteza sistemática da medida provén deste fit bidimensional.

7.3.5 SISTEMÁTICOS

A análise foi pensada dende un comezo pra reducir os sistemáticos todo o posibél, escollendo un modo de normalización cunha quinemática moi similar, empregando datos TISTISTIS e fixando os mesmos cortes en ambas seleccións offline. aínda así, diferentes fontes de erro sistemático son consideradas, especialmente as relacionadas ca corrección do parámetro α empregando PIDCalib e TrackCalib. aínda así, o erro sistemático está dominado polo fit do sinal (5.1 %).

7.3.6 CONCLUSIÓNS

Esta medida do $\mathcal{B}(\Lambda \to p\mu^-\bar{\nu}_\mu)$ está aínda multiplicada por un factor de blinding, un procedemento habitual no campo da física de altas enerxías. Ainda así, a incerteza estatística (1.5 %) e sistemática (6.0 %) acadada mellora significativamente a mellor

medida de $\mathcal{B}(\Lambda \to p\mu^- \bar{\nu}_\mu)$ realizada ata o de agora por BESIII, que presentaba unha incerteza do 14 %. A nosa medida terá importantes consecuencias na comprensión de $R^{\mu e}$, sendo sensíbel a desviacións significativas do SM. Será, polo tanto, un importante test da LFU en transicións $s \to u$

Cabe destacar que esta é a primeira vez que se mide a razón de ramificación dun hyperón en LHCb e tamén a primeira vez que se mide un decaemento semileptónico dunha partícula strange en LHCb.

APPENDIX A

APPENDIX

A.1 STRIPPING LINE EFFICIENCIES

A.1.1 SIGNAL PASSING SIGNALLINE

This efficiencies can be obtained by running in lxplus lb-dirac dirac-bookkeeping-rejection-stats -P sample-number, where sample-number will take the values depicted on Tab. A.1.

TABLE A.1: Production sample codes for each year and polarity.

	Magnet Down	Magnet Up
Sample Code 2018	131673	131676
Sample Code 2017	131679	131682
Sample Code 2016	131685	131688

A.1.2 $\Lambda \longrightarrow p\pi^-$ PASSING NORMLINE

The $\Lambda \longrightarrow p\pi^-$ Stripping Filtered Production Reconstruction Efficiency can be obtained by running in lxplus lb-dirac dirac-bookkeeping-rejection-stats -P sample-number, where sample-number will take the values depicted on Tab. A.2.

A.2 TRIGGER LINES FIRING MORE OFTEN IN SELECTED EVENTS

An interesting study is to check wich trigger Lines are firing more often in selected events for NormLine and SignalLine. The result can be seen in Figs. A.1, A.2, A.3.

TABLE A.2: Production sample codes for each year and polarity.

	Magnet Down	Magnet Up
Sample Code 2018	131695	131698
Sample Code 2017	131701	131704
Sample Code 2016	131707	131710

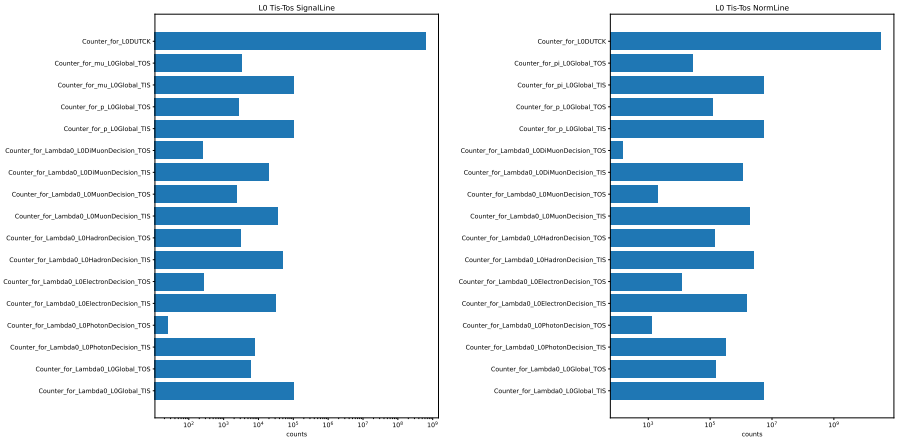

FIGURE A.1: Lo Trigger Lines firing more often in Selected Events. SignalLine case is depicted in the left plot and NormLine in the right one. Missing lines have counter = 0

A.3 BACKGROUND SOURCES

A.3.1 PID AND VERTEX REQUIREMENTS FOR EACH CHANNEL (MC, SIGNALLINE)

This appendix contains the truth-matching and vertex requirements for each channel, which are detailed below. As a reminder, 3122 is the numerical code for Λ, 2212 for p, 211 for π^+ and 13 for μ^-, where the negative numbers are associated to the correspondent antiparticles:

Selection requirements for the signal channel ($\Lambda \to p\mu^-\bar{\nu}_\mu$)

The requirements for selecting signal in the MC samples are detailed in Tab. A.3. The TRUE ID of each particle should match the corresponding number code to ensure correct MC association. Both the proton and the muon are required to have a Λ as their mother particle. These two particles should originate from the same vertex, which should also coincide with the Λ end vertex. Lastly, to confirm that both particles come from the same mother, the MC key of their respective mothers must match.

Below is the explicit code that ensures the satisfaction of the given conditions:

((Lambdao_TRUEID=3122 & p_TRUEID=2212 & mu_TRUEID=13) |

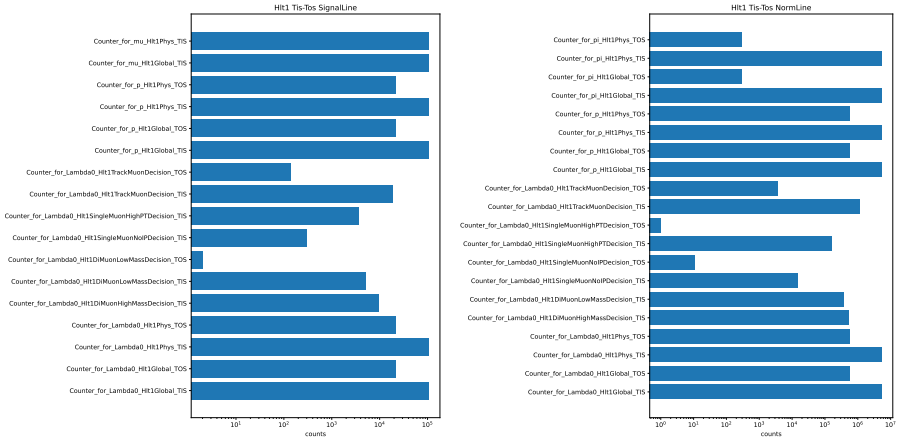

FIGURE A.2: Hlt1 Trigger Lines firing more often in Selected Events. SignalLine case is depicted in the left plot and NormLine in the right one. Missing lines have counter = 0

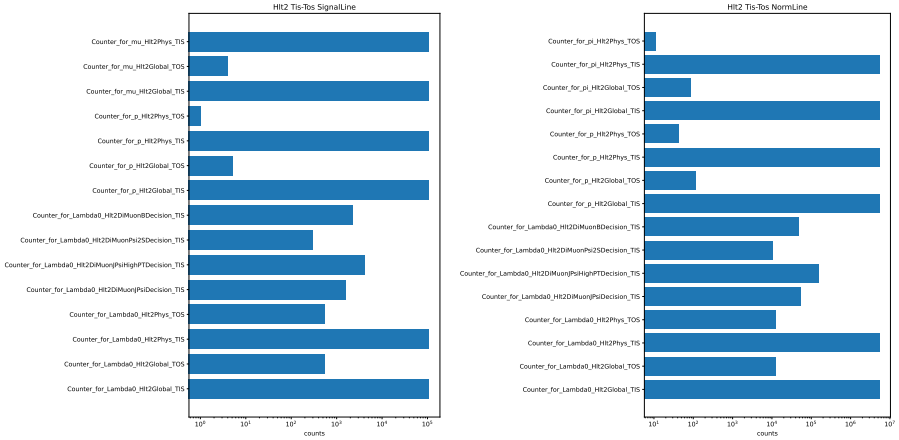

FIGURE A.3: Hlt2 Trigger Lines firing more often in Selected Events. SignalLine case is depicted in the left plot and NormLine in the right one. Missing lines have counter = 0

(Lambdao_TRUEID=-3122 & p_TRUEID=-2212 & mu_TRUEID=-13)) &
abs(mu_MC_MOTHER_ID)=3122 & abs(p_MC_MOTHER_ID)=3122 &
Lambdao_TRUEENDVERTEX_Z=mu_TRUEORIGINVERTEX_Z &
p_TRUEORIGINVERTEX_Z=mu_TRUEORIGINVERTEX_Z &
p_MC_MOTHER_KEY=mu_MC_MOTHER_KEY

Selection requirements for $\Lambda \to p\pi^-$

The requirements for selecting $\Lambda \to p\pi^-$ in the MC samples are detailed in Tab.

Requirement	Λ	p	μ^-
TRUE ID	3122	2212	13
TRUE ID CC	-3122	-2212	-13
abs(MOTHER ID)		3122	3122
ORIGIN VERTEX		Λ End Vertex	Λ End Vertex
MOTHER KEY		Λ KEY	Λ KEY

TABLE A.3: Requirements to select signal in the MC samples.

A.4. The TRUE ID of each particle should match the corresponding number code to ensure correct MC association. Both the proton and the pion are required to have a Λ as their mother particle. These two particles should originate from the same vertex, which should also coincide with the Λ end vertex. Lastly, to confirm that both particles come from the same mother, the MC key of their respective mothers must match.

Requirement	Λ	p	π^-
TRUE ID	3122	2212	-211
TRUE ID CC	-3122	-2212	211
abs(MOTHER ID)		3122	3122
ORIGIN VERTEX		Λ End Vertex	Λ End Vertex
MOTHER KEY		Λ KEY	Λ KEY

TABLE A.4: Requirements to select $\Lambda \rightarrow p\pi^-$ in the MC samples.Note that, in contrast to the muon, the sign of the negative pion is '-'.

Below is the explicit code that ensures the satisfaction of the given conditions:

((Lambdao_TRUEID=3122 & p_TRUEID=2212 & mu_TRUEID=-211) |
(Lambdao_TRUEID=-3122 & p_TRUEID=-2212 & mu_TRUEID=211)) &
abs(mu_MC_MOTHER_ID)=3122 & abs(p_MC_MOTHER_ID)=3122 &
Lambdao_TRUEENDVERTEX_Z=mu_TRUEORIGINVERTEX_Z &
p_TRUEORIGINVERTEX_Z=mu_TRUEORIGINVERTEX_Z &
p_MC_MOTHER_KEY=mu_MC_MOTHER_KEY

Selection requirements for eDIF ($\Lambda \rightarrow p(\pi^- \rightarrow \mu^- \bar{\nu}_\mu)$)

The requirements for selecting $\Lambda \rightarrow p(\pi^- \rightarrow \mu^- \bar{\nu}_\mu)$ in the MC samples are detailed in Tab. A.5. The TRUE ID of each particle should match the corresponding number code to ensure correct MC association. The proton is required to have a Λ as its mother particle and the muon is required to have a pion as mother and a Λ as grandmother. The muon should not originate from the Λ end vertex . Lastly, to confirm that both particles come from the same mother, the MC key of the proton mother and muon grandmother must match.

Below is the explicit code that ensures the satisfaction of the given conditions:

Requirement	Λ	p	μ^-
TRUE ID	3122	2212	13
TRUE ID CC	-3122	-2212	-13
abs(MOTHER ID)		3122	211
abs(GRANDMOTHER ID)			3122
ORIGIN VERTEX			not Λ End Vertex
KEY REQUIREMENT		mother = Λ KEY	Grandmother = Λ KEY

TABLE A.5: Requirements to select $\Lambda \to p(\pi^- \to \mu^- \bar{\nu}_\mu)$.

((Lambdao_TRUEID=3122 & p_TRUEID=2212 & mu_TRUEID=13) |
(Lambdao_TRUEID=-3122 & p_TRUEID=-2212 & mu_TRUEID=-13)) &
abs(p_MC_MOTHER_ID)=3122 & abs(mu_MC_MOTHER_ID)=211 &
abs(mu_MC_GD_MOTHER_ID)=3122 &
p_MC_MOTHER_KEY=mu_MC_GD_MOTHER_KEY &
Lambdao_TRUEENDVERTEX_Z≠mu_TRUEORIGINVERTEX_Z

Selection requirements for $K_S^0 \to \pi^+\pi^-$ The requirements for selecting $K_S^0 \to \pi^+\pi^-$ in the MC samples are detailed in Tab. A.6. The TRUE ID of each particle should match the corresponding number code to ensure correct MC association. Both pions are required to have a K_S^0 as their mother particle. These two particles should originate from the same vertex, which should also coincide with the K_S^0 end vertex. This sample is only used to design the selection and reject this channel and to remove this kind of events from the combinatorial background sample. Requirements are looser to remove also mismatched $K_S^0 \to \pi^+\pi^-$ from the combinatorial background sample.

Requirement	K_S^0	π^+	π^-
TRUE ID	310	211	-211
abs(MOTHER ID)		310	310
ORIGIN VERTEX		K_S^0 End Vertex	K_S^0 End Vertex
MOTHER KEY		K_S^0 KEY	K_S^0 KEY

TABLE A.6: Requirements to select $K_S^0 \to \pi^+\pi^-$ in the MC samples.

Below is the explicit code that ensures the satisfaction of the given conditions:

((Lambdao_TRUEID=3122 & p_TRUEID=2212 & mu_TRUEID=13) |
(Lambdao_TRUEID=-3122 & p_TRUEID=-2212 & mu_TRUEID=-13)) &
abs(mu_MC_MOTHER_ID)=3122 & abs(p_MC_MOTHER_ID)=3122 &
Lambdao_TRUEENDVERTEX_Z=mu_TRUEORIGINVERTEX_Z &
p_TRUEORIGINVERTEX_Z=mu_TRUEORIGINVERTEX_Z &
p_MC_MOTHER_KEY=mu_MC_MOTHER_KEY

A.4 PID AND VERTEX REQUIREMENTS FOR EACH CHANNEL (MC, NORMLINE)

Selection requirements for $\Lambda \rightarrow p\pi^-$

The requirements for selecting $\Lambda \rightarrow p\pi^-$ in the MC samples are detailed in Tab. A.4. The TRUE ID of each particle should match the corresponding number code to ensure correct MC association. Both the proton and the pion are required to have a Λ as their mother particle. These two particles should originate from the same vertex, which should also coincide with the Λ end vertex. Lastly, to confirm that both particles come from the same mother, the MC key of their respective mothers must match.

Requirement	Λ	p	π^-
TRUE ID	3122	2212	-211
TRUE ID CC	-3122	-2212	211
abs(MOTHER ID)		3122	3122
ORIGIN VERTEX		Λ End Vertex	Λ End Vertex
MOTHER KEY		Λ KEY	Λ KEY

TABLE A.7: Requirements to select $\Lambda \rightarrow p\pi^-$ in the MC samples.

Below is the explicit code that ensures the satisfaction of the given conditions:

((Lambdao_TRUEID=3122 & p_TRUEID=2212 & pi_TRUEID=-211) |
(Lambdao_TRUEID=-3122 & p_TRUEID=-2212 & pi_TRUEID=211)) &
abs(p_MC_MOTHER_ID) =3122 & abs(pi_MC_MOTHER_ID) =3122 &
p_MC_MOTHER_KEY=pi_MC_MOTHER_KEY &
p_TRUEORIGINVERTEX_Z=pi_TRUEORIGINVERTEX_Z

A.5 AVERAGE CONTRIBITION AFTER TIGHT PID CUTS.

We appled a mu_ProbNNmu > 0.8 to the MinBias MC sample after the Stripping process in SignalLine to study the average contribution to the sample afterwards. Result can be found in Tab. A.8.

Applying tight PID cuts increases the signal purity but also elevates the average contribution of the combinatorial background. For $\Lambda \rightarrow p\pi^-$, we have a stripping-filtered production, which also includes $\Lambda \rightarrow p(\pi^- \rightarrow \mu^-\bar{\nu}_\mu)$ events. This is not the case for the combinatorial background, where our primary source of MC is the MinBias sample passing the SignalLine. Consequently, a better strategy is to try to remove as much comb. background as possible, preserving more $\Lambda \rightarrow p\pi^-$ since we understand its behavior.

Another significant issue is that adding more PID cuts will necessitate correcting the PID efficiencies using PIDCalib2. A tight cut will reduce the statistics of the calibration samples, which are already low for our low-pt case. This will substantially increase our uncertainties.

TABLE A.8: Average contribution of each decay channel to the MinBias MC sample after the Stripping process in SignalLine and after require mu_ProbNNmu > 0.8. In the non-obvious cases, reconstructed particles are written in bold symbols.

Decay	Contribution
$\Lambda \rightarrow p\pi^-$	(27.7 ± 4.1) %
Combinatorial Background and Others	(40.3 ± 4.5) %
$\Lambda \rightarrow p(\pi^- \rightarrow \mu^- \bar{\nu}_\mu)$	(18.5 ± 3.5) %
$\Lambda \rightarrow p\mu^- \bar{\nu}_\mu$	(10.1 ± 2.8) %
$K^0_S \rightarrow \pi^+\pi^-$	(0.84 ± 0.84) %
$\Xi^- \rightarrow (\Lambda \rightarrow \boldsymbol{p}\pi^-)\boldsymbol{\pi^-}$	(1.7 ± 1.2) %
$\Xi^- \rightarrow (\Lambda \rightarrow \boldsymbol{p}\pi^-)(\pi^- \rightarrow \boldsymbol{\mu}\bar{\nu}_\mu)$	(0.84 ± 0.84) %

A.6 SEARCH FOR PEAKING BACKGROUNDS IN COMBINATORIAL BACKGROUND (MINBIAS MC)

An additional check was performed to ensure the absence of peaking backgrounds by replacing the mass hypothesis for the combinatorial background MC events. See Fig. A.4. M(p,π) distribution can be found in Fig. 5.30.

A.7 NEW VARIABLES

This is the code to compute **MCorr(pπ)** using Minuit:

```
def FCN3(psc):
    ppi = psc*p2
    pL = ppi + p1
    uL = vunit(pL)
    return 1 - abs(vdot(uL,flight))
fit = Minuit(FCN3 ,psc = 1.0, limit_psc = (0, 100))
fit.migrad()
ppi = fit.values["psc"]*p2
MppiCorr = sqrt(IM2(p1,ppi,Species[2212]['mass'], Species[211]['mass']))
```

Where flight is $\hat{\boldsymbol{f}}$, p1 the proton momentum and p2 the pion one.

A.8 DAVINCI VERSIONS AND TAGS

A.8.1 DATA 2018

(S34rop1, DaVinci/v44r10p2)

MD

DDDB: dddb-20190206-3 Condition DB:cond-20180202

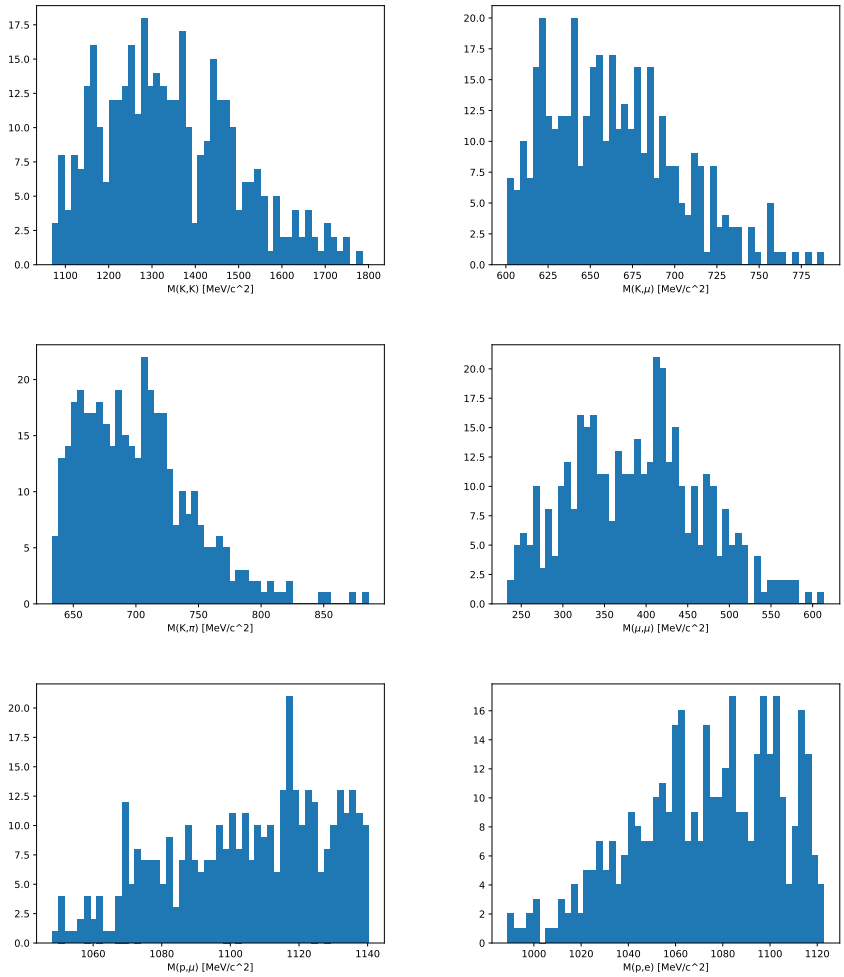

FIGURE A.4: Search for peaking backgrounds by replacing the mass hypothesis for the combinatorial background MC events.

BKQuery("/LHCb/Collision18/Beam6500GeV-VeloClosed-MagDown
/Real Data/Reco18/Stripping34rop1/90000000/LEPTONIC.MDST")

MU

DDDB: dddb-20190206-3 Condition DB:cond-20180202
BKQuery("/LHCb/Collision18/Beam6500GeV-VeloClosed-MagUp/
Real Data/Reco18/Stripping34rop1/90000000/LEPTONIC.MDST")

A.8.2 DATA 2017

(S29r2p1, DaVinci/v42r9p2)

MD
DDDB: dddb-20190206-3 Condition DB:cond-20191004-2
BKQuery("/LHCb/Collision17/Beam6500GeV-VeloClosed-MagDown/
Real Data/Reco17/Stripping29r2p1/90000000/LEPTONIC.MDST")

MU
DDDB: dddb-20190206-3 Condition DB:cond-20191004-2
BKQuery("/LHCb/Collision17/Beam6500GeV-VeloClosed-MagUp/
Real Data/Reco17/Stripping29r2p1/90000000/LEPTONIC.MDST")

A.8.3 DATA 2016

(S28r2, DaVinci/v44r10p5)

MD
DDDB: dddb-20190206-3 Condition DB:cond-20191004-1
BKQuery("/LHCb/Collision16/Beam6500GeV-VeloClosed-MagDown/
Real Data/Reco16/Stripping28r2/90000000/LEPTONIC.MDST")

MU
DDDB: dddb-20190206-3 Condition DB:cond-20191004-1
BKQuery("/LHCb/Collision16/Beam6500GeV-VeloClosed-MagUp/
Real Data/Reco16/Stripping28r2/90000000/LEPTONIC.MDST")

A.8.4 LPPI STRIPPING FILTERED 2018

(S34rop1, DaVinci/v44r10p2)

MD
DDDB: dddb-20170721-3 Condition DB: sim-20190430-vc-md100
BKQuery("MC/2018/Beam6500GeV-2018-MagDown-Nu1.6-25ns-Pythia8/Sim09k/
Trig0x617d18a4/Reco18/Turbo05-WithTurcal/Stripping34rop1Filtered/ 33102103/
LAMBDA2PMUNU.STRIP.DST")

MU
DDDB: dddb-20170721-3 Condition DB: sim-20190430-vc-mu100
BKQuery("MC/2018/Beam6500GeV-2018-MagUp-Nu1.6-25ns-Pythia8/Sim09k/
Trig0x617d18a4/Reco18/Turbo05-WithTurcal/Stripping34rop1Filtered/ 33102103/
LAMBDA2PMUNU.STRIP.DST")

A.8.5 LPPI STRIPPING FILTERED 2017

(S29r2p1, DaVinci/v42r9p2)

MD
DDDB: dddb-20170721-3 Condition DB: sim-20190430-1-vc-md100
BKQuery("MC/2017/Beam6500GeV-2017-MagDown-Nu1.6-25ns-Pythia8/Sim09k/
Trigox62661709/Reco17/Turbo04a-WithTurcal/Stripping29r2p1Filtered/ 33102103/
LAMBDA2PMUNU.STRIP.DST")

MU
DDDB: dddb-20170721-3 Condition DB: sim-20190430-1-vc-mu100
BKQuery("MC/2017/Beam6500GeV-2017-MagUp-Nu1.6-25ns-Pythia8/Sim09k/
Trigox62661709/Reco17/Turbo04a-WithTurcal/Stripping29r2p1Filtered/ 33102103/
LAMBDA2PMUNU.STRIP.DST")

A.8.6 LPPI STRIPPING FILTERED 2016

(S28r2, DaVinci/v44r10p5)

MD
DDDB: dddb-20170721-3 Condition DB: sim-20170721-2-vc-md100
BKQuery("MC/2016/Beam6500GeV-2016-MagDown-Nu1.6-25ns-Pythia8/Sim09k/
Trigox6139160F/Reco16/Turbo03a/Stripping28r2Filtered/ 33102103/LAMBDA2PMUNU.STRIP.DST")

MU
DDDB: dddb-20170721-3 Condition DB: sim-20170721-2-vc-mu100
BKQuery("MC/2016/Beam6500GeV-2016-MagUp-Nu1.6-25ns-Pythia8/Sim09k/
Trigox6139160F/Reco16/Turbo03a/Stripping28r2Filtered/ 33102103/LAMBDA2PMUNU.STRIP.DST")

A.8.7 LPMUNU STRIPPING FILTERED 2018

(S34rop1, DaVinci/v44r10p2)

MD
DDDB: dddb-20170721-3 Condition DB: sim-20190430-vc-md100
BKQuery("MC/2018/Beam6500GeV-2018-MagDown-Nu1.6-25ns-Pythia8/Sim09k/
Trigox617d18a4/Reco18/Turbo05-WithTurcal/Stripping34rop1Filtered/
33512008/LAMBDA2PMUNU.STRIP.DST")

MU
DDDB: dddb-20170721-3 Condition DB: sim-20190430-vc-mu100
BKQuery("MC/2018/Beam6500GeV-2018-MagUp-Nu1.6-25ns-Pythia8/Sim09k/

Trig0x617d18a4/Reco18/Turbo05-WithTurcal/Stripping34r0p1Filtered/
33512008/LAMBDA2PMUNU.STRIP.DST")

A.8.8 LPMUNU STRIPPING FILTERED 2017

(S29r2p1, DaVinci/v42r9p2)

MD
DDDB: dddb-20170721-3 Condition DB: sim-20190430-1-vc-md100
BKQuery("MC/2017/Beam6500GeV-2017-MagDown-Nu1.6-25ns-Pythia8/Sim09k/
Trig0x62661709/Reco17/Turbo04a-WithTurcal/Stripping29r2p1Filtered/
33512008/LAMBDA2PMUNU.STRIP.DST")

MU
DDDB: dddb-20170721-3 Condition DB: sim-20190430-1-vc-mu100
BKQuery("MC/2017/Beam6500GeV-2017-MagUp-Nu1.6-25ns-Pythia8/Sim09k/
Trig0x62661709/Reco17/Turbo04a-WithTurcal/Stripping29r2p1Filtered/
33512008/LAMBDA2PMUNU.STRIP.DST")

A.8.9 LPMUNU STRIPPING FILTERED 2016

(S28r2, DaVinci/v44r10p5)

MD
DDDB: dddb-20170721-3 Condition DB: sim-20170721-2-vc-md100
BKQuery("MC/2016/Beam6500GeV-2016-MagDown-Nu1.6-25ns-Pythia8/Sim09k/
Trig0x6139160F/Reco16/Turbo03a/Stripping28r2Filtered/
33512008/LAMBDA2PMUNU.STRIP.DST")

MU
DDDB: dddb-20170721-3 Condition DB: sim-20170721-2-vc-mu100
BKQuery("MC/2016/Beam6500GeV-2016-MagUp-Nu1.6-25ns-Pythia8/Sim09k/
Trig0x6139160F/Reco16/Turbo03a/Stripping28r2Filtered/
33512008/LAMBDA2PMUNU.STRIP.DST")

A.8.10 MINBIAS MC 2018

(S34r0p1, DaVinci/v44r10p2)

MD
DDDB: dddb-20170721-3 Condition DB: sim-20190430-vc-md100
BKQuery("MC/2018/Beam6500GeV-2018-MagDown-Nu1.6-25ns-Pythia8/ Sim09k/

Trigox617d18a4/Reco18/30000000/LDST")

MU
DDDB: dddb-20170721-3 Condition DB: sim-20190430-vc-mu100
BKQuery("MC/2018/Beam6500GeV-2018-MagUp-Nu1.6-25ns-Pythia8/ Sim09k/
Trigox617d18a4/Reco18/30000000/LDST")

A.8.11 SIGNAL PRIVATE PRODUCTION TO CORRECT STRIPPING EFF:

YEAR: 2016 MD
EventType=33512008

APPCONFIGOPTS_Gauss=
/cvmfs/lhcb.cern.ch/lib/lhcb/DBASE/AppConfig/v3r395/options
APPCONFIGOPTS_Boole=
/cvmfs/lhcb.cern.ch/lib/lhcb/DBASE/AppConfig/v3r374/options
APPCONFIGOPTS_Moore_1=
/cvmfs/lhcb.cern.ch/lib/lhcb/DBASE/AppConfig/v3r297/options
APPCONFIGOPTS_Moore_2=
/cvmfs/lhcb.cern.ch/lib/lhcb/DBASE/AppConfig/v3r297/options
APPCONFIGOPTS_Moore_3=
/cvmfs/lhcb.cern.ch/lib/lhcb/DBASE/AppConfig/v3r355/options
APPCONFIGOPTS_Brunel=
/cvmfs/lhcb.cern.ch/lib/lhcb/DBASE/AppConfig/v3r401/options
DECFILESROOT=
/cvmfs/lhcb.cern.ch/lib/lhcb/DBASE/Gen/DecFiles/v30r57
LBPYTHIA8ROOT=
/cvmfs/lhcb.cern.ch/lib/lhcb/GAUSS/GAUSS_v49r20/Gen/LbPythia8

GAUSS:

```
source /cvmfs/lhcb.cern.ch/lib/LbEnv.sh -c x86\_64-slc6-gcc48-opt

lb-run Gauss/v49r20 gaudirun.py \${APPCONFIGOPTS\_Gauss}/Gauss/Beam6500GeV-\
${magnet}100-2016-nu1.6.py \${APPCONFIGOPTS\_Gauss}/Gauss/EnableSpillover-25ns.py
\${APPCONFIGOPTS\_Gauss}/Gauss/DataType-\${year}.py
\${APPCONFIGOPTS\_Gauss}/Gauss/RICHRandomHits.py
\${DECFILESROOT}/options/\${EventType}.py
\$LBPYTHIA8ROOT/options/Pythia8.py
\${APPCONFIGOPTS\_Gauss}/Gauss/G4PL\_FTFP\_BERT\_EmNoCuts.py
\${mainDir}/extraOptionsGauss.py

BOOLE:

source /cvmfs/lhcb.cern.ch/lib/LbEnv.sh -c x86\_64-slc6-gcc49-opt
```

```
lb-run Boole/v30r4 gaudirun.py \${APPCONFIGOPTS\_Boole}/
Boole/Default.py
\${APPCONFIGOPTS\_Boole}/Boole/EnableSpillover.py
\${APPCONFIGOPTS\_Boole}/Boole/DataType-2015.py
\${APPCONFIGOPTS\_Boole}/Boole/Boole-SetOdinRndTrigger.py
\${mainDir}/extraOptionsBoole.py

MOORE L0:

source /cvmfs/lhcb.cern.ch/lib/LbEnv.sh -c x86\_64-slc6-gcc48-opt

lb-run Moore/v25r4 gaudirun.py
\${APPCONFIGOPTS\_Moore\_1}/L0App/L0AppSimProduction.py
\${APPCONFIGOPTS\_Moore\_1}/L0App/L0AppTCK-0x160F.py
\${APPCONFIGOPTS\_Moore\_1}/L0App/ForceLUTVersionV8.py
\${APPCONFIGOPTS\_Moore\_1}/L0App/DataType-2016.py
\${APPCONFIGOPTS\_Moore\_1}/Persistency/Compression-ZLIB-1.py
\${mainDir}/extraOptionsMooreL0.py

MOORE HLT1:

source /cvmfs/lhcb.cern.ch/lib/LbEnv.sh -c
x86\_64-slc6-gcc48-opt \par

lb-run Moore/v25r4 gaudirun.py
\${APPCONFIGOPTS\_Moore\_2}/Moore/
MooreSimProductionForSeparateL0AppStep2015.py
\${APPCONFIGOPTS\_Moore\_2}/Conditions/TCK-0x5138160F.py
\${APPCONFIGOPTS\_Moore\_2}/L0App/DataType-2016.py
\${APPCONFIGOPTS\_Moore\_2}/Persistency/Compression-ZLIB-1.py
\${APPCONFIGOPTS\_Moore\_2}/Moore/MooreSimProductionHlt1.py
\${mainDir}/extraOptionsMooreL1.py

MOORE HLT2:

source /cvmfs/lhcb.cern.ch/lib/LbEnv.sh
-c x86\_64-slc6-gcc48-opt

lb-run Moore/v25r4 gaudirun.p \${APPCONFIGOPTS\_Moore\_3}/Moore/
MooreSimProductionForSeparateL0AppStep2015.py
\${APPCONFIGOPTS\_Moore\_3}/Conditions/TCK-0x6139160F.py
\${APPCONFIGOPTS\_Moore\_3}/L0App/DataType-2016.py
\${APPCONFIGOPTS\_Moore\_3}/Persistency/Compression-ZLIB-1.py
\${APPCONFIGOPTS\_Moore\_3}/Moore/MooreSimProductionHlt2.py
\${mainDir}/extraOptionsMooreL2.py
```

```
BRUNEL:

source /cvmfs/lhcb.cern.ch/lib/LbEnv.sh
-c x86\_64-slc6-gcc49-opt \par

lb-run Brunel/v50r7 gaudirun.py
\${APPCONFIGOPTS\_Brunel}/Brunel/DataType-2016.py
\${APPCONFIGOPTS\_Brunel}/Brunel/MC-WithTruth.py
\${APPCONFIGOPTS\_Brunel}/Brunel/SplitRawEventOutput.4.3.py
\${mainDir}/extraOptionsBrunel.py

Where basically the extraOptions file are:

LHCbApp().DDDBtag  = "dddb-20170721-3"
LHCbApp().CondDBtag  = "sim-20170721-2-vc-"+pol+"100"

DAVINCI:
DaVinci version: DaVinci/v44r10p5

tags:
DaVinci().DDDBtag  = "dddb-20170721-3"
DaVinci().CondDBtag = "sim-20170721-2-vc-md100"

\#dddb-20190206-3
\#cond-20191004-1


Particles:


from StandardParticles import
StdLooseProtons, StdAllLooseMuons
\#StdAllNoPIDsProtons,StdAllNoPIDsMuons
```

We are supposing that $\epsilon_{Lpmu}^{SignalLine} = \epsilon_{CutsNoPID}^{SignalLine} \times \epsilon_{CutsPID}^{SignalLine}$, so we have to calculate each efficiency separately.

The first one, $\epsilon_{CutsNoPID}^{SignalLine}$, can be obtained applying just the NoPID Stripping Line cuts:

```
 if ((((tReco.Lambda0_TRUEID==3122) and
 (tReco.p_TRUEID==2212) and (tReco.mu_TRUEID==13)) |
 ((tReco.Lambda0_TRUEID==-3122) and (tReco.p_TRUEID==-2212)
 and (tReco.mu_TRUEID==-13))) and
 (tReco.Lambda0_TRUEENDVERTEX_Z==tReco.mu_TRUEORIGINVERTEX_Z)
```

```
and ((tReco.p_TRUEORIGINVERTEX_Z==tReco.mu_TRUEORIGINVERTEX_Z))):

   if tReco.Lambda0_M<1141 and tReco.mu_TRACK_CHI2NDOF<3
       and tReco.mu_IPCHI2_OWNPV>60  and tReco.mu_IP_OWNPV>1 and
       tReco.mu_TRACK_GhostProb<0.2 and
       tReco.p_TRACK_GhostProb<0.2 and
       tReco.p_TRACK_CHI2NDOF<3 and
       tReco.p_IPCHI2_OWNPV>16 and
       tReco.Lambda0_IP_OWNPV>0.2 and
       tReco.Lambda0_VCHI2NDOF<9 and tReco.Lambda0_AMAXDOCA<0.3
       and tReco.Lambda0_BPVLTIME>0.009
       and tRe\co.Lambda0_BPVVDCHI2>50 and
       tReco.Lambda0_MIPDV_PRIMARY>0.2:

                   counterStrippingNoPID+=1

                   if tReco.mu_ProbNNmu>0.3 and
                   tReco.mu_isMuon==True and
                   tReco.mu_ProbNNpi<0.7 and
                   tReco.mu_ProbNNk<0.7 and
                   tReco.p_ProbNNp>0.3 and
                   tReco.p_ProbNNmu<0.7 and
                   tReco.p_ProbNNk<0.7:

        counterStrippingPID+=1
```

This can be done for Reconstructed tuples using as input for the CombineParticles StdLooseProtons and StdAllLooseMuons or StdAllNoPIDsProtons and StdAllNoPIDsMuons.

The results are:
NoPIDsParticles:$\epsilon^{SignalLine}_{CutsNoPIDs} = 0.025189530$
LooseParticles:$\epsilon^{SignalLine}_{CutsNoPIDs} = 0.0089420$

A.9 DECFILES

A.9.1 LPPI: TIGHTCUT (33102103)

```
# EventType: 33102103
#
# Descriptor: [Lambda0 -> pi- p+]cc
#
# NickName: Lambda_ppi=PHSP,TightCut
#
# Cuts: LoKi::GenCutTool/TightCut
#
# Documentation: Lambda0 decay to p+ pi- with phase space model,
Tight cut.
#  * Lambda0 endvertex z in [-1m,0.8m]
#  * Lambda0 endvertex radial cut at 38mm
# EndDocumentation
#
# CPUTime: < 1 min
#
# InsertPythonCode:
# #
# from Configurables import LoKi__GenCutTool
# from Gauss.Configuration import *
# gen = Generation()
# gen.SignalPlain.addTool ( LoKi__GenCutTool , 'TightCut' )
# #
# tightCut = gen.SignalPlain.TightCut
# tightCut.Decay     = '[^(Lambda0 => ^p+ ^pi-)]CC'
# tightCut.Preambulo += [
#   "from GaudiKernel.SystemOfUnits import meter, millimeter, GeV, MeV" ,
#    "inAcc        =  in_range ( 0.005 , GTHETA , 0.400 )         " ,
#    "inEta        =  in_range ( 1.95  , GETA   , 5.050 )         " ,
#    "goodTrack    =  inAcc & inEta" ,
#    "GVX = LoKi.GenVertices.PositionX() " ,
#    "GVY = LoKi.GenVertices.PositionY() " ,
#    "GVZ = LoKi.GenVertices.PositionZ() " ,
#    "vx    =  GFAEVX ( GVX, 100 * meter )  " ,
#    "vy    =  GFAEVX ( GVY, 100 * meter )  " ,
#    "rho2  =  vx**2 + vy**2  " ,
#    "rhoK  = rho2 < (38 * millimeter )**2 " ,
#   "decay = in_range ( -1 * meter, GFAEVX ( GVZ, 100 * meter ), 0.8 * meter ) ",
#    "goodpion = (GPZ > 0) & (GPT > 100*MeV ) & (GP > 3.0*GeV)",
#    "goodproton = (GPT > 275*MeV ) & (GP > 12.25*GeV)"
# ]
```

```
# tightCut.Cuts      =    {
#    "[Lambda0]cc"   : "decay & rhoK",
#    "[p+]cc"         : "goodTrack & goodproton " ,
#    "[pi-]cc"         : "goodTrack & goodpion"
#                        }
# EndInsertPythonCode
#
# PhysicsWG: RD
# Tested: Yes
# Responsible: Alexandre Brea Rodriguez
# Email: alexandre.brea.rodriguez@cern.ch
# Date: 20201221
#
Decay Lambda0sig
  1.000         p+        pi-        PHSP;
Enddecay
CDecay anti-Lambda0sig
#
End
#
```

A.9.2 LPMUNU: TIGHTCUT SHD (33512008)

```
# EventType: 33512008
#
# Descriptor: [Lambda0 -> p+ mu- anti-nu_mu]cc
#
# NickName: Lambda_pmunuSHD=TightCut
#
# Cuts: LoKi::GenCutTool/TightCut
#
# Documentation: Lambda0 decay to p+ mu- anti-nu_mu with SHD model.
prob=0.615, probcos=0.366001501202 tight generator cut
#  * Lambda0 endvertex z in [-1m,0.8m]
#  * Lambda0 endvertex radial cut at 38mm
# EndDocumentation
#
# CPUTime: < 1 min
#
# InsertPythonCode:
# #
# from Configurables import LoKi__GenCutTool
# from Gauss.Configuration import *
# gen = Generation()
```

```
# gen.SignalPlain.addTool ( LoKi__GenCutTool , 'TightCut' )
# #
# tightCut = gen.SignalPlain.TightCut
# tightCut.Decay     = '[^(Lambda0 => ^p+ ^mu- nu_mu~)]CC'
# tightCut.Preambulo += [
#    "from GaudiKernel.SystemOfUnits import meter, millimeter, GeV" ,
#    "GY          =  LoKi.GenParticles.Rapidity () ## to be sure " ,
#    "inY         =  in_range ( 1.9   , GY     , 4.6   )         " ,
#    "inAcc       =  in_range ( 0.005 , GTHETA , 0.400 )         " ,
#    "inEta       =  in_range ( 1.95  , GETA   , 5.050 )         " ,
#    "goodTrack    =  inAcc & inEta" ,
#    "GVX = LoKi.GenVertices.PositionX() " ,
#    "GVY = LoKi.GenVertices.PositionY() " ,
#    "GVZ = LoKi.GenVertices.PositionZ() " ,
#    "vx    = GFAEVX ( GVX, 100 * meter ) " ,
#    "vy    = GFAEVX ( GVY, 100 * meter ) " ,
#    "rho2  =  vx**2 + vy**2 " ,
#    "rhoK  = rho2 < (38 * millimeter )**2 " ,
#   "decay = in_range ( -1 * meter, GFAEVX ( GVZ, 100 * meter ), 0.8 * meter ) ",
# ]
# tightCut.Cuts      =    {
#    "[Lambda0]cc"  : "decay & rhoK",
#   "[mu-]cc"        : "goodTrack " ,
#   "[p+]cc"         : "goodTrack "
#                       }
# EndInsertPythonCode
# PhysicsWG: RD
# Tested: Yes
# Responsible: Alexandre Brea Rodriguez
# Email: alexandre.brea.rodriguez@cern.ch
# Date: 20190101
#
#Alias      MyLambda0      Lambda0
#Alias      Myanti-Lambda0     anti-Lambda0
#ChargeConj MyLambda0          Myanti-Lambda0
Decay Lambda0sig
  1.000         p+        mu-        anti-nu_mu        SHD;
Enddecay
CDecay anti-Lambda0sig
#
End
```

A.10 PIDCALIB2

A.10.1 SIGNAL LINE

In our case we should run the following commands:

```
pidcalib2.make_eff_hists -c "Brunel_InMuonAcc == 1.0" --sample Turbo16
--magnet down --particle Mu_nopt --pid-cut "Brunel_MC15TuneV1_ProbNNmu>0.3
& Brunel_MC15TuneV1_ProbNNpi<0.7 & Brunel_MC15TuneV1_ProbNNk<0.7"
--cut "Brunel_IsMuon & Brunel_TRCHI2NDOF<3 & Brunel_TRACK_GHOSTPROB<0.2
& Brunel_IPCHI2>60" --bin-var Brunel_P --bin-var Brunel_ETA --bin-var
nSPDhits --binning-file binning-file_noPT.txt --output-dir pidcalib_output/
```

```
pidcalib2.make_eff_hists --sample Turbo16 --magnet down --particle P
--pid-cut "Brunel_DLLp>-5 & Brunel_MC15TuneV1_ProbNNp > 0.3 &
Brunel_MC15TuneV1_ProbNNmu < 0.7 & Brunel_MC15TuneV1_ProbNNk < 0.7"
--cut "Brunel_PT>250 & Brunel_HasRich==1 & Brunel_TRCHI2NDOF<3 &
Brunel_TRACK_GHOSTPROB<0.2 & Brunel_IPCHI2>16" --bin-var Brunel_P
--bin-var Brunel_ETA --bin-var nSPDhits --binning-file
proton_binning-file.txt --output-dir pidcalib_output/
```

Where the -c "InMuonAcc == 1.0" option was included because we want to separate the efficiency related to the Muon System acceptance and the muon PID efficiency, so the InMuonAcc cut was applied previously to the PIDCalib process. In our case we should also use the Mu_nopt instead of usual Mu, since the default muon calibration sample has a transverse momentum cut of 800 $\boldsymbol{MeV/c}$ and a total momentum cut of 3 GeV/c. The Brunel prefix for the variables indicates that we are using the offline variables, since the aliases without this prefix are used for values at the trigger stages.

Concerning the binning JSON file indicating the bin edges, it was designed taking into account the nSPDHits and the muon and proton ETA and P distributions after applying all the NoPID cuts detailed before (A.5).

To compute the corrected efficiencies for the proton and the muon of the private Signal MC sample after the non-PID selection Cuts, the applied commands were:

```
pidcalib2.ref_calib --sample Turbo16 --magnet down --ref-file
data/LambdapmunuSIM_2016MD_NoPIDS_ETA_Cuts.root -t "T"
--histo-dir pidcalib_output --bin-vars '{"Brunel_P": "P",
"Brunel_ETA": "ETA", "nSPDhits": "nSPDHits"}' --ref-pars
'{"mu": ["Mu_nopt", "Brunel_MC15TuneV1_ProbNNmu>0.3 &
Brunel_MC15TuneV1_ProbNNpi<0.7 & Brunel_MC15TuneV1_ProbNNk<0.7"]}'
--output-file mu_md_ntuple_PID_eff.root
```

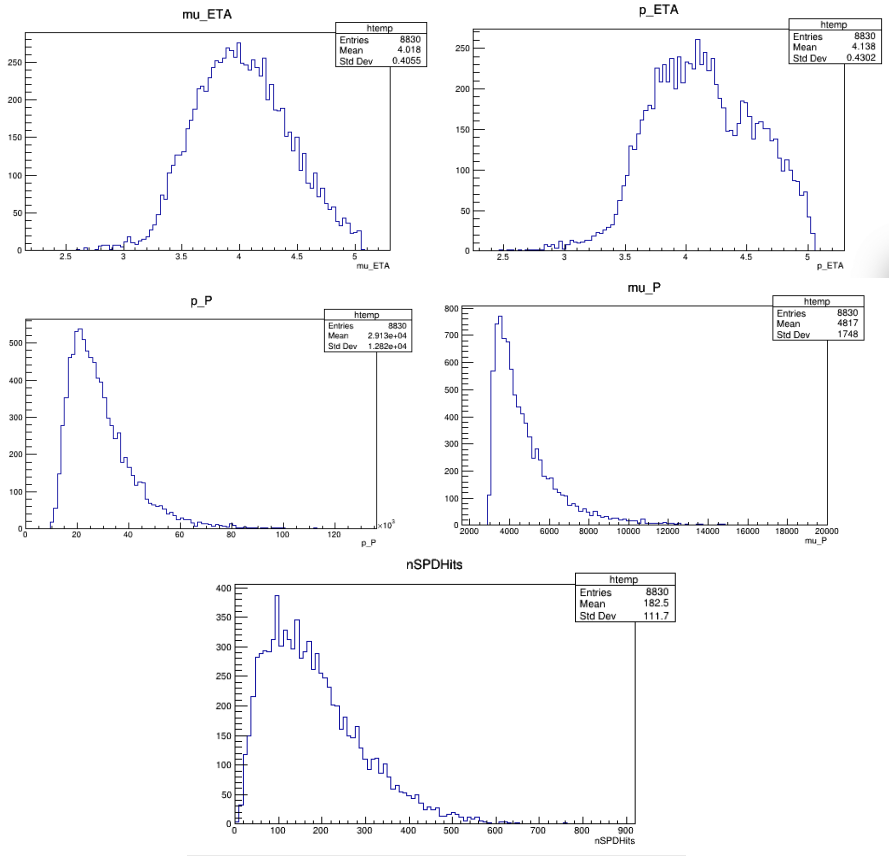

FIGURE A.5: Distributions of the binning variables after the non-PID selection Cuts for muon and proton tracks.

```
pidcalib2.ref_calib --sample Turbo16 --magnet down --ref-file
data/LambdapmunuSIM_2016MD_NoPIDS_ETA_Cuts.root -t "T"
--histo-dir pidcalib_output --bin-vars '{"Brunel_P": "P",
"Brunel_ETA": "ETA", "nSPDhits": "nSPDHits"}' --ref-pars '{"p": ["P",
"Brunel__DLLp > -5 & Brunel_MC15TuneV1_ProbNNp > 0.3 &
Brunel_MC15TuneV1_ProbNNmu < 0.7 & Brunel_MC15TuneV1_ProbNNk < 0.7"]}'
--output-file p_md_ntuple_PID_eff.root
```

A.10.2 NORM LINE

In this case, the commands to create the efficiency histograms for the proton and the pion case should be:

```
pidcalib2.make_eff_hists --sample Turbo18 --magnet down --particle Pi_KS
```

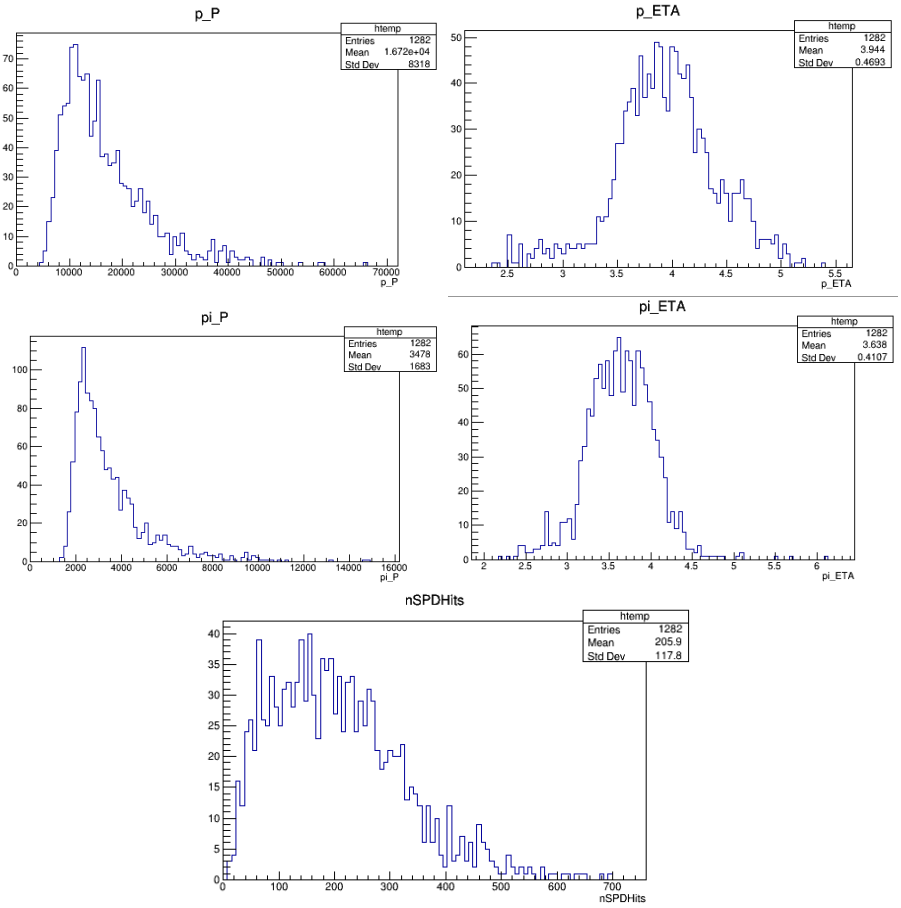

FIGURE A.6: Distributions of the binning variables after the non-PID selection Cuts for pion and proton tracks.

```
--pid-cut "Brunel_MC15TuneV1_ProbNNpi > 0.4 & Brunel_MC15TuneV1_ProbNNmu <
 0.7 & Brunel_MC15TuneV1_ProbNNk < 0.7" --cut "Brunel_IsMuon!=1 &
 Brunel_TRCHI2NDOF<3 & Brunel_TRACK_GHOSTPROB<0.2 & Brunel_IPCHI2>60 &
 Brunel_HasRich==1" --bin-var Brunel_P --bin-var Brunel_ETA --bin-var
 nSPDhits --binning-file Pi_KS_binning-file_noPT.txt --output-dir
 pidcalib_output/

 pidcalib2.make_eff_hists --sample Turbo18 --magnet down --particle P
--pid-cut "Brunel_DLLp>-5 & Brunel_MC15TuneV1_ProbNNp > 0.3 &
 Brunel_MC15TuneV1_ProbNNmu < 0.7 & Brunel_MC15TuneV1_ProbNNk < 0.7"
--cut "Brunel_PT>250 & Brunel_HasRich==1 & Brunel_TRCHI2NDOF<3 &
 Brunel_TRACK_GHOSTPROB<0.2 & Brunel_IPCHI2>16" --bin-var Brunel_P
--bin-var Brunel_ETA --bin-var nSPDhits --binning-file proton_binning-
```

```
file.txt --output-dir pidcalib_output/
```

Concerning the binning JSON file indicating the bin edges, it was designed taking into account the nSPDHits and the pion and proton ETA and P distributions after applying all the NoPID cuts detailed before (A.6).

And to compute the efficiencies:

```
pidcalib2.ref_calib --sample Turbo18 --magnet down --ref-file
data/LambdappiSIM_2018MD_NoPIDS_ETA_Cuts.root -t "T" --histo-dir
pidcalib_output --bin-vars '{"Brunel_P": "P", "Brunel_ETA": "ETA",
"nSPDhits": "nSPDHits"}' --ref-pars '{"pi": ["Pi_KS",
"Brunel_MC15TuneV1_ProbNNpi>0.4 & Brunel_MC15TuneV1_ProbNNmu<0.7 &
Brunel_MC15TuneV1_ProbNNk<0.7"]}' --output-file
pi_KS_md_ntuple_PID_eff.root

pidcalib2.ref_calib --sample Turbo18 --magnet down --ref-file
data/LambdappiSIM_2018MD_NoPIDS_ETA_Cuts.root -t "T" --histo-dir
pidcalib_output --bin-vars '{"Brunel_P": "P", "Brunel_ETA": "ETA",
"nSPDhits": "nSPDHits"}' --ref-pars '{"p": ["P",
"Brunel_DLLp>-5&Brunel_MC15TuneV1_ProbNNp>0.3&
Brunel_MC15TuneV1_ProbNNmu<0.7& Brunel_MC15TuneV1_ProbNNk<0.7"]}'
--output-file p_md_ntuple_PID_eff.root
```

A.11 PIDCALIB2 SCHEMES

A.11.1 SIGNAL STRIPPING LINE

PidCalib2 results are affected by the chosen binning. To take into account this systematic source of uncertainty, we can estimate how the obtained efficiency varies by changing the binning scheme.

Binning1:

```
{"Mu_nopt":
{"Brunel_P": [0, 2500, 5000, 7500, 10000, 15000, 20000],
"nSPDhits":[0, 200, 400, 600, 800, 1000],
"Brunel_ETA":[ 2.0, 3.0, 4.0, 5.0, 6.0]}}

{"P":
{"Brunel_P": [0,15000,25000,35000,50000,75000,100000,125000,180000],
"nSPDhits":[0, 200, 400, 600, 800, 1000],
"Brunel_ETA":[2.0,2.2,2.7,3.3,3.8,4.25,4.6,5.5]}}
```

$\epsilon_{CutsPID}^{SignalLine}$ = 46.1 ± 1.7 %

Binning2:

```
{"Mu_nopt":
{"Brunel_P": [0, 2500, 5000, 7500, 10000, 15000, 20000],
"nSPDhits":[0, 200, 400, 600, 800, 1000],
"Brunel_ETA":[ 2.0, 3.0, 4.0, 5.0, 6.0]}}

{"P":
{"Brunel_P": [0,15000,25000,35000,50000,75000,100000,125000,180000],
"nSPDhits":[0, 200, 400, 600, 800, 1000],
"Brunel_ETA":[2.0,2.5,3.0,4.0,5.0,5.5]}}
```

$\epsilon_{CutsPID}^{SignalLine}$ = 46.4 ± 1.7 %

Binning3:

```
{"Mu_nopt":
{"Brunel_P": [0, 2500, 5000, 7500, 10000, 15000, 20000],
"nSPDhits":[0, 200, 400, 600, 800, 1000],
"Brunel_ETA":[ 2.0, 3.0, 4.0, 5.0, 6.0]}}

{"P":
{"Brunel_P": [0,15000,30000,45000,60000,75000,100000,125000,160000],
"nSPDhits":[0, 200, 400, 600, 800, 1000],
"Brunel_ETA":[2.0,2.5,3.0,4.0,5.0,5.5]}}
```

$\epsilon_{CutsPID}^{SignalLine}$ = 46.2 ± 1.7 %

Binning4:

```
{"Mu_nopt":
{"Brunel_P": [0, 2500, 5000, 7500, 10000, 15000, 20000],
"nSPDhits":[0, 200, 400, 600, 800, 1000],
"Brunel_ETA":[ 2.0, 3.0, 4.0, 5.0, 6.0]}}

{"P":
{"Brunel_P": [5000,20000,35000,50000,65000,80000,95000,110000,160000],
"nSPDhits":[0, 200, 400, 600, 800, 1000],
"Brunel_ETA":[2.0,2.5,3.0,4.0,5.0,5.5]}}
```

$\epsilon_{CutsPID}^{SignalLine}$ = 45.2 ± 1.7 %

Binning5: (Lower value)

```
{"Mu_nopt":
{"Brunel_P": [0, 2500, 5000, 7500, 10000, 15000, 20000],
"nSPDhits":[0, 200, 400, 600, 800, 1000],
"Brunel_ETA":[ 2.0, 3.0, 4.0, 5.0, 6.0]}}

{"P":
{"Brunel_P":[0,20000,30000,40000,50000,65000,80000,95000,110000,160000],
"nSPDhits":[0, 200, 400, 600, 800, 1000],
"Brunel_ETA":[2.0,2.5,3.0,4.0,5.0,5.5]}}
```

$$\epsilon_{CutsPID}^{SignalLine} = 45.1 \pm 1.6\ \%$$

Binning6:

```
{"Mu_nopt":
{"Brunel_P": [0, 2500, 5000, 7500, 10000, 15000, 20000],
"nSPDhits":[0, 200, 400, 600, 800, 1000],
"Brunel_ETA":[ 2.0, 3.0, 4.0, 5.0, 6.0]}}

{"P":
{"Brunel_P":[0,20000,30000,40000,50000,65000,80000,95000,110000,160000],
"nSPDhits":[0, 50, 100, 200, 400, 600, 800, 1200],
"Brunel_ETA":[2.0,2.5,3.0,4.0,5.0,5.5]}}
```

$$\epsilon_{CutsPID}^{SignalLine} = 46.1 \pm 1.7\ \%$$

Binning7:

```
{"Mu_nopt":
{"Brunel_P": [0, 2500, 5000, 7500, 10000, 15000, 20000],
"nSPDhits":[0, 200, 400, 600, 800, 1000],
"Brunel_ETA":[ 2.0, 3.0, 4.0, 5.0, 6.0]}}

{"P":
{"Brunel_P": [0,15000,30000,45000,60000,75000,90000,105000,140000,180000],
"nSPDhits":[0, 50, 100, 200, 400, 600, 800, 1500],
"Brunel_ETA":[2.0,2.2,2.7,3.3,3.8,4.25,4.6,5.5]}}
```

$$\epsilon_{CutsPID}^{SignalLine} = 47.2 \pm 1.7\ \%$$

Binning8:

```
{"Mu_nopt":
{"Brunel_P": [0, 2500, 5000, 7500, 10000, 12500, 15000, 20000],
```

"nSPDhits":[0, 100, 200, 400, 600, 800, 1000],
"Brunel_ETA":[2.0, 3.0, 4.0, 5.0, 6.0]}}

{"P":
{"Brunel_P": [0,15000,30000,45000,60000,75000,90000,105000,140000,180000],
"nSPDhits":[0, 50, 100, 200, 400, 600, 800, 1500],
"Brunel_ETA":[2.0, 2.2, 2.7, 3.3, 3.8, 4.25, 4.6, 5.5]}}

$\epsilon_{CutsPID}^{SignalLine} = 47.5 \pm 2.3\ \%$

Binning9:

{"Mu_nopt":
{"Brunel_P": [0, 2500, 5000, 7500, 10000, 12500, 15000, 20000],
"nSPDhits":[0, 100, 250, 400, 600, 800, 1000],
"Brunel_ETA":[2.0, 3.0, 4.0, 5.0, 6.0]}}

{"P":
{"Brunel_P": [0,15000,30000,45000,60000,75000,90000,105000,140000,180000],
"nSPDhits":[0, 50, 100, 200, 400, 600, 800, 1500],
"Brunel_ETA":[2.0, 2.2, 2.7, 3.3, 3.8, 4.25, 4.6, 5.5]}}

$\epsilon_{CutsPID}^{SignalLine} = 46.9 \pm 2.2\ \%$

Binning10:

{"Mu_nopt":
{"Brunel_P": [0, 3000, 4500, 6000, 8000, 11000, 20000],
"nSPDhits":[0, 100, 250, 400, 600, 800, 1000],
"Brunel_ETA":[2.5, 3.0, 4.0, 5.0, 5.5]}}

{"P":
{"Brunel_P": [0,15000,30000,45000,60000,75000,90000,105000,140000,180000],
"nSPDhits":[0, 50, 100, 200, 400, 600, 800, 1500],
"Brunel_ETA":[2.0, 2.2, 2.7, 3.3, 3.8, 4.25, 4.6, 5.5]}}

$\epsilon_{CutsPID}^{SignalLine} = 47.3 \pm 2.3\ \%$

Binning11:

{"Mu_nopt":
{"Brunel_P": [0, 3000, 4500, 6000, 8000, 11000, 20000],
"nSPDhits":[0, 100, 250, 400, 600, 800, 1000],
"Brunel_ETA":[2.5, 3.0, 4.0, 5.0, 5.5]}}

```
{"P":
{"Brunel_P": [0,15000,30000,45000,60000,75000,90000,105000,140000,180000],
 "nSPDhits":[0, 50, 100, 200, 400, 600, 800, 1500],
 "Brunel_ETA":[2.0, 2.2, 2.7, 3.3, 3.8, 4.25, 4.6, 5.5]}}
```

$$\epsilon_{CutsPID}^{SignalLine} = 47.2 \pm 2.8\ \%$$

Binning12: (Higher Value)

```
{"Mu_nopt":
{"Brunel_P": [0, 3000, 4500, 6000, 8000, 11000, 20000],
 "nSPDhits":[0, 75, 150, 300, 400, 600, 1000],
 "Brunel_ETA":[2.5, 3.0, 4.0, 5.0, 5.5]}}

{"P":
{"Brunel_P": [0,15000,30000,45000,60000,75000,90000,105000,140000,180000],
 "nSPDhits":[0, 50, 100, 200, 400, 600, 800, 1500],
 "Brunel_ETA":[2.0, 2.2, 2.7, 3.3, 3.8, 4.25, 4.6, 5.5]}}
```

$$\epsilon_{CutsPID}^{SignalLine} = 48.2 \pm 3.3\ \%$$

Binning13:

```
{"Mu_nopt":
{"Brunel_P": [2000, 3000, 4500, 5000, 6000, 8000, 20000],
 "nSPDhits":[0, 75, 150, 300, 400, 600, 1000],
 "Brunel_ETA":[2.5, 3.0, 4.0, 5.0, 5.5]}}

{"P":
{"Brunel_P": [0,15000,30000,45000,60000,75000,90000,105000,140000,180000],
 "nSPDhits":[0, 50, 100, 200, 400, 600, 800, 1500],
 "Brunel_ETA":[2.0, 2.2, 2.7, 3.3, 3.8, 4.25, 4.6, 5.5]}}
```

$$\epsilon_{CutsPID}^{SignalLine} = 45.3 \pm 4.1\ \%$$

Binning14:

```
{"Mu_nopt":
{"Brunel_P": [0, 2500, 5000, 7500, 10000, 12500, 15000, 20000],
 "nSPDhits":[0, 100, 200, 400, 600, 800, 1000],
 "Brunel_ETA":[2.0, 3.0, 4.0, 5.0, 6.0]}}

{"P":
```

{"Brunel_P": [0,15000, 25000,35000, 50000, 75000, 100000,125000,180000],
"nSPDhits":[0, 50, 100, 200, 400, 600, 800, 1500],
"Brunel_ETA":[2.0, 2.2, 2.7, 3.3, 3.8, 4.25, 4.6, 5.5]}}

$$\epsilon_{CutsPID}^{SignalLine} = 47.6 \pm 2.3\ \%$$

SignalLine PidCalib2 result:

Computing the average of all the efficiencies obtained changing the binning, we obtain $\epsilon_{CutsPID}^{SignalLine} = 46.59 \pm 0.65\ \%$

We can take as systematic uncertainty the maximum difference from this average value obtained , which is 1.61 %.

A.11.2 NORM STRIPPING LINE

Binning 0:

{"Pi_KS": {"Brunel_P": [0,1000, 2000, 2500, 3000, 3500, 4000, 4500, 5500,
6500,7500, 8500, 10000, 13000, 16000],
"nSPDhits":[0, 50, 100, 150, 200, 300, 400, 500, 600, 750],
"Brunel_ETA":[2.2,2.5,2.7,3.0,3.3,3.8,4.0,4.25,4.6,5.2,6.5]}}

{"P": {"Brunel_P": [0,5000,8000,11000,13000,15000,20000,25000,30000,
35000,40000,50000,70000],
"nSPDhits":[0, 50, 100, 150, 200, 300, 400, 500, 600, 750],
"Brunel_ETA":[2.2,2.7,3.1,3.3,3.5,3.8,4.1,4.35,4.6,5.0,5.5]}}

$$\epsilon_{CutsPID}^{NormLine} = 42.64 \pm 0.54\ \%$$

Binning 1:

{"Pi_KS": {"Brunel_P": [0,1000, 2000, 2500, 3000, 3500, 4000, 4500, 5500,
6500,7500, 8500, 10000, 13000, 16000],
"nSPDhits":[0, 50, 100, 150, 200, 300, 400, 500, 600, 750],
"Brunel_ETA":[2.2,2.5,2.7,3.0,3.3,3.8,4.0,4.25,4.6,5.2,6.5]}}

{"P": {"Brunel_P": [0,15000, 25000,35000, 50000, 75000, 100000,125000,
180000],
"nSPDhits":[0, 50, 100, 200, 400, 600, 800, 1500],

"Brunel_ETA":[2.0, 2.2, 2.7, 3.3, 3.8, 4.25, 4.6, 5.5]}}

$\epsilon_{CutsPID}^{NormLine} = 44.84 \pm 0.29$ %

Binning 2:

{"Pi_KS": {"Brunel_P": [0,1000, 2000, 2500, 3000, 3500, 4000, 4500, 5500,
6500,7500, 8500, 10000, 13000, 16000],
"nSPDhits":[0, 50, 100, 150, 200, 300, 400, 500, 600, 750],
"Brunel_ETA":[2.2,2.5,2.7,3.0,3.3,3.8,4.0,4.25,4.6,5.2,6.5]}}

{"P": {"Brunel_P:[0,15000,30000,45000,60000,75000,
90000,105000,140000,180000],
"nSPDhits":[0, 50, 100, 200, 400, 600, 800, 1500],
"Brunel_ETA":[2.0, 2.2, 2.7, 3.3, 3.8, 4.25, 4.6, 5.5]}}

$\epsilon_{CutsPID}^{NormLine} = 45.98 \pm 0.27$ %

Binning 3:

{"Pi_KS": {"Brunel_P": [0,1000, 2000, 2500, 3000, 3500, 4000, 4500, 5500,
6500,7500, 8500, 10000, 13000, 16000],
"nSPDhits":[0, 50, 100, 150, 200, 300, 400, 500, 600, 750],
"Brunel_ETA":[2.2,2.5,2.7,3.0,3.3,3.8,4.0,4.25,4.6,5.2,6.5]}}

{"P": {"Brunel_P":[0,15000,30000,45000,60000,75000,100000,125000,160000],
"nSPDhits":[0, 200, 400, 600, 800, 1000],
"Brunel_ETA":[2.0,2.5,3.0,4.0,5.0,5.5]}}

$\epsilon_{CutsPID}^{NormLine} = 44.56 \pm 0.15$ %

Binning 4:

{"Pi_KS": {"Brunel_P": [0,1000, 2000, 2500, 3000, 3500, 4000, 4500, 5500,
6500,7500, 8500, 10000, 13000, 16000],

"nSPDhits":[0, 50, 100, 150, 200, 300, 400, 500, 600, 750],
"Brunel_ETA":[2.2,2.5,2.7,3.0,3.3,3.8,4.0,4.25,4.6,5.2,6.5]}}

{"P": {"Brunel_P": [0,5000,10000,15000,20000,30000,50000,80000],
"nSPDhits":[0, 200, 400, 600, 800, 1000],
"Brunel_ETA":[2.0,2.5,3.0,4.0,5.0,5.5]}}

$\epsilon_{CutsPID}^{NormLine} = 41.94 \pm 0.16$ %

Binning 5:

{"Pi_KS": {"Brunel_P": [0,1000, 2000, 2500, 3000, 3500, 4000, 4500, 5500,
6500,7500, 8500, 10000, 13000, 16000],
"nSPDhits":[0, 50, 100, 150, 200, 300, 400, 500, 600, 750],
"Brunel_ETA":[2.2,2.5,2.7,3.0,3.3,3.8,4.0,4.25,4.6,5.2,6.5]}}

{"P": {"Brunel_P": [0,2000,5000,7500,10000,12500,15000,20000, 30000,
45000,80000],
"nSPDhits":[0, 200, 400, 600, 800, 1000],
"Brunel_ETA":[2.0,2.5,3.0,4.0,5.0,5.5]}}

$\epsilon_{CutsPID}^{NormLine} = 41.46 \pm 0.17$ %

Binning 6:

{"Pi_KS": {"Brunel_P": [0,1000, 2000, 2500, 3000, 3500, 4000, 4500, 5500,
6500,7500, 8500, 10000, 13000, 16000],
"nSPDhits":[0, 50, 100, 150, 200, 300, 400, 500, 600, 750],
"Brunel_ETA":[2.2,2.5,2.7,3.0,3.3,3.8,4.0,4.25,4.6,5.2,6.5]}}

{"P": {"Brunel_P": [0,5000,9000,13000,16000,20000,30000,80000],
"nSPDhits":[0, 200, 400, 600, 800, 1000],
"Brunel_ETA":[2.0,2.5,3.0,4.0,5.0,5.5]}}

$\epsilon_{CutsPID}^{NormLine} = 42.80 \pm 0.34$ %

Binning 7:


```
{"Pi_KS": {"Brunel_P": [0,1000, 2000, 2500, 3000, 3500, 4000, 4500, 5500,
 6500,7500, 8500, 10000, 13000, 16000],
 "nSPDhits":[0, 50, 100, 150, 200, 300, 400, 500, 600, 750],
 "Brunel_ETA":[2.2,2.5,2.7,3.0,3.3,3.8,4.0,4.25,4.6,5.2,6.5]}}


{"P":{"Brunel_P": [0,5000,9000,13000,16000,20000,30000,80000],
 "nSPDhits":[0, 100, 200, 300, 400, 600, 800],
 "Brunel_ETA":[2.0, 2.2, 2.7, 3.3, 3.8, 4.25, 4.6, 5.5]}}
```


$\epsilon_{CutsPID}^{NormLine} = 42.88 \pm 0.29$ %

Binning 8:


```
{"Pi_KS": {"Brunel_P": [0, 2000, 2500, 3000, 3500, 4000,
 5000, 8000, 10000, 16000],
 "nSPDhits":[0, 50, 100, 150, 200, 300, 400, 500, 600, 750],
 "Brunel_ETA":[2.2,2.5,2.7,3.0,3.3,3.8,4.0,4.25,4.6,5.2,6.5]}}

{"P": {"Brunel_P": [0,5000,8000,11000,13000,15000,20000,
 25000,30000,35000,40000,50000,70000],
 "nSPDhits":[0, 50, 100, 150, 200, 300, 400, 500, 600, 750],
 "Brunel_ETA":[2.2,2.7,3.1,3.3,3.5,3.8,4.1,4.35,4.6,5.0,5.5]}}
```


$\epsilon_{CutsPID}^{NormLine} = 42.65 \pm 0.54$ %

Binning 9:


```
{"Pi_KS": {"Brunel_P": [0, 2000, 3000, 4000, 5000, 8000, 10000, 16000],
 "nSPDhits":[0, 50, 100, 150, 200, 300, 400, 500, 600, 750],
 "Brunel_ETA":[2.2,2.5,2.7,3.0,3.3,3.\
 8,4.0,4.25,4.6,5.2,6.5]}}

{"P": {"Brunel_P": [0,5000,8000,11000,13000,15000,20000,
 25000,30000,35000,40000,50000,70000],
 "nSPDhits":[0, 50, 100, 150, 200, 300, 400, 500, 600, 750],
 "Brunel_ETA":[2.2,2.7,3.1,3.3,3.5,3.8,4.1,4.35,4.6,5.0,5.5]}}
```

$\epsilon_{CutsPID}^{NormLine} = 42.77 \pm 0.53$ %

Binning 10:

```
{"Pi_KS": {"Brunel_P": [0, 2000, 2500, 3000, 3500, 4000, 5000, 8000,
10000, 16000],
"nSPDhits":[0, 100, 200, 400, 600, 750],
"Brunel_ETA":[2.2,2.5,2.7,3.0,3.3,3.8,4.0,4.25,4.6,5.2,6.5]}}
```

```
{"P": {"Brunel_P": [0,5000,8000,11000,13000,15000,20000,
25000,30000,35000,40000,50000,70000],
"nSPDhits":[0, 50, 100, 150, 200, 300, 400, 500, 600, 750],
"Brunel_ETA":[2.2,2.7,3.1,3.3,3.5,3.8,4.1,4.35,4.6,5.0,5.5]}}
```

$\epsilon_{CutsPID}^{NormLine} = 42.53 \pm 0.53$ %

Binning 11:

```
{"Pi_KS": {"Brunel_P": [0, 1800, 2200, 2500, 3000, 4000, 5000, 8000, 16000],
"nSPDhits":[0, 50, 100, 150, 200, 300, 400, 500, 600, 750],
"Brunel_ETA":[2.2,2.5,2.7,3.0,3.3,3.8,4.0,4.25,4.6,5.2,6.5]}}
```

```
{"P": {"Brunel_P": [0,5000,8000,11000,13000,15000,20000,
25000,30000,35000,40000,50000,70000],
"nSPDhits":[0, 50, 100, 150, 200, 300, 400, 500, 600, 750],
"Brunel_ETA":[2.2,2.7,3.1,3.3,3.5,3.8,4.1,4.35,4.6,5.0,5.5]}}
```

$\epsilon_{CutsPID}^{NormLine} = 42.64 \pm 0.54$ %

Binning 12:

```
{"Pi_KS": {"Brunel_P": [0, 2000, 2500, 3000, 4500, 7000, 10000, 16000],
"nSPDhits":[0, 100, 200, 300, 400, 600, 750],
"Brunel_ETA":[2.0,2.5,3.0,3.5,3.8,4.25,4.6,6.5]}}
```

```
{"P": {"Brunel_P": [0,5000,8000,11000,13000,15000,20000,
25000,30000,35000,40000,50000,70000],
"nSPDhits":[0, 50, 100, 150, 200, 300, 400, 500, 600, 750],
"Brunel_ETA":[2.2,2.7,3.1,3.3,3.5,3.8,4.1,4.35,4.6,5.0,5.5]}}
```


$\epsilon_{CutsPID}^{NormLine} = 42.61 \pm 0.53$ %

Binning 13:


```
{"Pi_KS": {"Brunel_P": [0,1000, 2000, 2500, 3000, 3500, 4000,
4500, 5500, 6500, 7500, 8500, 10000, 13000, 16000],
"nSPDhits":[0, 50, 100, 150, 200, 300, 400, 500, 600, 750],
"Brunel_ETA":[2.0,2.5,3.0,3.5,3.8,4.25,4.6,6.5]}}
```

```
{"P": {"Brunel_P": [0,5000,8000,11000,13000,15000,20000,
25000,30000,35000,40000,50000,70000],
"nSPDhits":[0, 50, 100, 150, 200, 300, 400, 500, 600, 750],
"Brunel_ETA":[2.2,2.7,3.1,3.3,3.5,3.8,4.1,4.35,4.6,5.0,5.5]}}
```


$\epsilon_{CutsPID}^{NormLine} = 42.63 \pm 0.53$ %

NormLine PidCalib2 result:

Computing the average of all the efficiencies obtained changing the binning, we obtain $\epsilon_{CutsPID}^{NormlLine} = 42.50 \pm 0.14$ %.

We can take as systematic uncertainty the maximum difference from this average value obtained , which is 1.04 %.

BIBLIOGRAPHY

[1] R. Aaij et al. "Allen: A High-Level Trigger on GPUs for LHCb". In: *Computing and Software for Big Science* 4.1 (Apr. 2020), p. 7. ISSN: 2510-2044. DOI: 10.1007/s41781-020-00039-7. URL: https://doi.org/10.1007/s41781-020-00039-7.

[2] R. Aaij et al. "Constraints on the $K_S^0 \to \mu^+\mu^-$ Branching Fraction". In: *Phys. Rev. Lett.* 125 (23 Dec. 2020), p. 231801. DOI: 10.1103/PhysRevLett.125.231801. URL: https://link.aps.org/doi/10.1103/PhysRevLett.125.231801.

[3] R. Aaij et al. "Evidence for the Rare Decay $\Sigma^+ \to p\mu^+\mu^-$". In: *Phys. Rev. Lett.* 120 (22 May 2018), p. 221803. DOI: 10.1103/PhysRevLett.120.221803. URL: https://link.aps.org/doi/10.1103/PhysRevLett.120.221803.

[4] R. Aaij et al. "Search for $K^0_{S(L)} \to \mu^+\mu^-\mu^+\mu^-$ decays at LHCb". In: *Phys. Rev. D* 108 (3 2023), p. L031102. DOI: 10.1103/PhysRevD.108.L031102. URL: https://link.aps.org/doi/10.1103/PhysRevD.108.L031102.

[5] Carlos Abellán Beteta et al. *Calibration and performance of the LHCb calorimeters in Run 1 and 2 at the LHC*. Tech. rep. 2020. arXiv: 2008.11556. URL: https://cds.cern.ch/record/2729028.

[6] M. Ablikim et al. "First Measurement of the Absolute Branching Fraction of $\Lambda \to p\mu^-\bar{\nu}_\mu$". In: *Phys. Rev. Lett.* 127.12 (2021), p. 121802. DOI: 10.1103/PhysRevLett.127.121802. arXiv: 2107.06704 [hep-ex].

[7] B. Adeva et al. "Roadmap for selected key measurements of LHCb". In: (Dec. 2009). arXiv: 0912.4179 [hep-ex].

[8] S. Agostinelli et al. "Geant4—a simulation toolkit". In: *Nuclear Instruments and Methods in Physics Research Section A: Accelerators, Spectrometers, Detectors and Associated Equipment* 506.3 (2003), pp. 250–303. ISSN: 0168-9002. DOI: https://doi.org/10.1016/S0168-9002(03)01368-8. URL: https://www.sciencedirect.com/science/article/pii/S0168900203013688.

[9] Rodrigo Alonso, Benjamin Grinstein, and Jorge Martin Camalich. "Lifetime of B_c^- Mesons Constrains Explanations for Anomalies in $B \to D^{(*)}\tau\nu$". In: *Phys. Rev. Lett.* 118 (8 2017), p. 081802. DOI: 10.1103/PhysRevLett.118.081802. URL: https://link.aps.org/doi/10.1103/PhysRevLett.118.081802.

[10] A. A. Alves Junior et al. "Prospects for Measurements with Strange Hadrons at LHCb". In: *JHEP* 05 (2019), p. 048. DOI: 10.1007/JHEP05(2019)048. arXiv: 1808.03477 [hep-ex].

[11] S Amato et al. *LHCb calorimeters: Technical Design Report*. Technical design report. LHCb. Geneva: CERN, 2000. URL: https://cds.cern.ch/record/494264.

[12] S Amato et al. *LHCb RICH: Technical Design Report*. Technical design report. LHCb. Geneva: CERN, 2000. URL: https://cds.cern.ch/record/494263.

[13] " Background rejection study in the search for $\Lambda^0 \to p^+\mu^-\overline{\nu}$". In: (2019). URL: https://cds.cern.ch/record/2688792.

[14] P R Barbosa-Marinho et al. *LHCb inner tracker: Technical Design Report*. Technical design report. LHCb. revised version number 1 submitted on 2002-11-13 14:14:34. Geneva: CERN, 2002. URL: https://cds.cern.ch/record/582793.

[15] P R Barbosa-Marinho et al. *LHCb muon system: Technical Design Report*. Technical design report. LHCb. Geneva: CERN, 2001. URL: https://cds.cern.ch/record/504326.

[16] P R Barbosa-Marinho et al. *LHCb outer tracker: Technical Design Report*. Technical design report. LHCb. Geneva: CERN, 2001. URL: https://cds.cern.ch/record/519146.

[17] G Barrand et al. "GAUDI: The software architecture and framework for building LHCb data processing applications". In: (2000). DOI: 10.1016/S0010-4655(01)00254-5. URL: https://cds.cern.ch/record/467678.

[18] J. Batley et al. "Measurement of the form factors of charged kaon semileptonic decays". In: *Journal of High Energy Physics* 2018 (2018). DOI: 10.1007/JHEP10(2018)150.

[19] Christian Bierlich et al. *A comprehensive guide to the physics and usage of PYTHIA 8.3*. 2022. arXiv: 2203.11601 [hep-ph].

[20] E. Blucher and W.J. Marciano. "Vud, Vus, the Cabibbo Angle and CKM Unitarity". In: *PDG* (2021). URL: https://pdg.lbl.gov/2021/reviews/rpp2021-rev-vud-vus.pdf.

[21] Christoph Bobeth and Andrzej J. Buras. "Leptoquarks meet ϵ'/ϵ and rare Kaon processes". In: *Journal of High Energy Physics* 2018.2 (Feb. 2018). DOI: 10.1007/jhep02(2018)101. URL: https://doi.org/10.1007%2Fjhep02%282018%29101.

[22] Nicola Cabibbo, Earl C. Swallow, and Roland Winston. "SEMILEPTONIC HYPERON DECAYS". In: *Annual Review of Nuclear and Particle Science* 53.1 (2003), pp. 39–75. DOI: 10.1146/annurev.nucl.53.013103.155258. eprint: https://doi.org/10.1146/annurev.nucl.53.013103.155258. URL: https://doi.org/10.1146/annurev.nucl.53.013103.155258.

[23] Nicola Cabibbo, Earl C. Swallow, and Roland Winston. "Semileptonic hyperon decays and CKM unitarity". In: *Phys. Rev. Lett.* 92 (2004), p. 251803. DOI: 10.1103/PhysRevLett.92.251803. arXiv: hep-ph/0307214.

[24] R. Calabrese et al. "Performance of the LHCb RICH detectors during LHC Run 2". In: *Journal of Instrumentation* 17.07 (July 2022), P07013. DOI: 10.1088/1748-0221/17/07/p07013. URL: https://doi.org/10.1088%2F1748-0221%2F17%2F07%2Fp07013.

[25] Alejandro Celis. "LHC phenomenology of two-Higgs-doublet models in the LHC era". PhD thesis. Valencia U., 2014.

[26] Hsi-Ming Chang, Martin González-Alonso, and Jorge Martin Camalich. "Nonstandard Semileptonic Hyperon Decays". In: *Phys. Rev. Lett.* 114.16 (2015), p. 161802. DOI: 10.1103/PhysRevLett.114.161802. arXiv: 1412.8484 [hep-ph].

[27] Ling-Lie Chau and Wai-Yee Keung. "Comments on the Parametrization of the Kobayashi-Maskawa Matrix". In: *prl* 53.19 (Nov. 1984), pp. 1802–1805. DOI: 10.1103/PhysRevLett.53.1802.

[28] Siddhartha Chib and Edward Greenberg. "Understanding the Metropolis-Hastings Algorithm". In: *The American Statistician* 49.4 (1995), pp. 327–335. ISSN: 00031305. URL: http://www.jstor.org/stable/2684568 (visited on 10/13/2023).

[29] Veronika Chobanova et al. "Probing SUSY effects in $K_S^0 \to \mu^+\mu^-$". In: *Journal of High Energy Physics* 2018.5 (May 2018). DOI: 10.1007/jhep05(2018)024. URL: https://doi.org/10.1007%2Fjhep05%282018%29024.

[30] Gregory Ciezarek et al. "A Challenge to Lepton Universality in B Meson Decays". In: *Nature* 546 (2017), pp. 227–233. DOI: 10.1038/nature22346. arXiv: 1703.01766 [hep-ex].

[31] Vincenzo Cirigliano et al. "Precision Beta Decay as a Probe of New Physics". In: (July 2019). arXiv: 1907.02164 [nucl-ex].

[32] LHCb Collaboration. *LHCb VELO Upgrade Technical Design Report*. Tech. rep. 2013. URL: https://cds.cern.ch/record/1624070.

[33] LHCb collaboration. *Parameters of Simo8 Monte Carlo productions*. 2014. URL: https://twiki.cern.ch/twiki/bin/view/LHCb/SettingsSim08#Minimum_Bias_Definition.

[34] LHCb collaboration et al. *The LHCb upgrade I*. 2023. arXiv: 2305.10515 [hep-ex].

[35] The LHCb Collaboration. *LHCb reoptimized detector design and performance: Technical Design Report*. Technical design report. LHCb. Geneva: CERN, 2003. URL: https://cds.cern.ch/record/630827.

[36] The LHCb Collaboration. *LHCb VELO (VErtex LOcator): Technical Design Report*. Technical design report. LHCb. Geneva: CERN, 2001. URL: https://cds.cern.ch/record/504321.

[37] The LHCb Collaboration. "The LHCb Detector at the LHC". In: *Journal of Instrumentation* 3.08 (Aug. 2008), S08005. DOI: 10.1088/1748-0221/3/08/S08005. URL: https://dx.doi.org/10.1088/1748-0221/3/08/S08005.

[38] G. Cowan. *Statistical data analysis*. Oxford University Press, USA, 1998.

[39] Giancarlo D'Ambrosio and Teppei Kitahara. "Direct CP Violation in $K_S^0 \to \mu^+\mu^-$". In: *Physical Review Letters* 119.20 (Nov. 2017). DOI: 10.1103/physrevlett.119.201802. URL: https://doi.org/10.1103%2Fphysrevlett.119.201802.

[40] Sacha Davidson and Sébastien Descotes-Genon. ""Minimal Flavour Violation" for leptoquarks". In: *Journal of High Energy Physics* 2010.11 (Nov. 2010). DOI: 10.1007/jhep11(2010)073. URL: https://doi.org/10.1007%2Fjhep11%282010%29073.

[41] Ramandeep Singh Dehal et al. "GPU Computing Revolution: CUDA". In: *2018 International Conference on Advances in Computing, Communication Control and Networking (ICACCCN)*. 2018, pp. 197–201. DOI: 10.1109/ICACCCN.2018.8748495.

[42] Francesco Dettori. "Production measurements at LHCb with the first data". In: *Particles and fields. Proceedings, Meeting of the Division of the American Physical Society, DPF 2009, Detroit, USA, July 26-31, 2009*. 2009. arXiv: 0909.5596 [hep-ex].

[43] Luca Di Luzio, Admir Greljo, and Marco Nardecchia. "Gauge leptoquark as the origin of B-physics anomalies". In: *Phys. Rev. D* 96.11 (2017), p. 115011. DOI: 10.1103/PhysRevD.96.115011. arXiv: 1708.08450 [hep-ph].

[44] Lars Eklund. *The LHCb Upgrade*. 2017. arXiv: 1709.04709 [physics.ins-det].

[45] Lyndon Evans and Philip Bryant. "LHC Machine". In: *Journal of Instrumentation* 3.08 (Aug. 2008), S08001. DOI: 10.1088/1748-0221/3/08/S08001. URL: https://dx.doi.org/10.1088/1748-0221/3/08/S08001.

[46] Ferruccio Feruglio, Paride Paradisi, and Andrea Pattori. "Revisiting Lepton Flavor Universality in B Decays". In: *Phys. Rev. Lett.* 118 (1 2017), p. 011801. DOI: 10.1103/PhysRevLett.118.011801. URL: https://link.aps.org/doi/10.1103/PhysRevLett.118.011801.

[47] Oliver Fischer et al. "Unveiling hidden physics at the LHC". In: *The European Physical Journal C* 82.8 (Aug. 2022). DOI: 10.1140/epjc/s10052-022-10541-4. URL: https://doi.org/10.1140%2Fepjc%2Fs10052-022-10541-4.

[48] Dordei Francesca. "LHCb detector and trigger performance in Run II". In: *EPJ Web of Conferences* 164 (Jan. 2017), p. 01016. DOI: 10.1051/epjconf/201716401016.

[49] M Frank et al. "Deferred High Level Trigger in LHCb: A Boost to CPU Resource Utilization". In: *Journal of Physics: Conference Series* 513.1 (June 2014), p. 012006. DOI: 10.1088/1742-6596/513/1/012006. URL: https://dx.doi.org/10.1088/1742-6596/513/1/012006.

[50] A. Garcia and P. Kielanowski. *THE BETA DECAY OF HYPERONS*. Ed. by A. Bohm. Vol. 222. 1985. DOI: 10.1007/3-540-15184-2.

[51] Admir Greljo and David Marzocca. "High- p_T dilepton tails and flavor physics". In: *The European Physical Journal C* 77.8 (2017). DOI: 10.1140/epjc/s10052-017-5119-8. URL: https://doi.org/10.1140%2Fepjc%2Fs10052-017-5119-8.

[52] Diego Guadagnoli and Patrick Koppenburg. *Lepton-flavor violation and lepton-flavor-universality violation in b and c decays*. 2023. arXiv: 2207.01851 [hep-ph].

[53] J. C. Hardy and I. S. Towner. "Superallowed $0^+ \rightarrow 0^+$ nuclear β decays: 2020 critical survey, with implications for V_{ud} and CKM unitarity". In: *Phys. Rev. C* 102 (4 Oct. 2020), p. 045501. DOI: 10.1103/PhysRevC.102.045501. URL: https://link.aps.org/doi/10.1103/PhysRevC.102.045501.

[54] Bob Holdom et al. "Four Statements about the Fourth Generation". In: *PMC Physics A* 3 (Apr. 2009). DOI: 10.1186/1754-0410-3-4.

[55] Gino Isidori and Rene Unterdorfer. "On the short-distance constraints from $K_{L,S} \to \mu^+\mu^-$". In: *Journal of High Energy Physics* 2004.01 (Jan. 2004), pp. 009–009. DOI: 10.1088/1126-6708/2004/01/009. URL: https://doi.org/10.1088%2F1126-6708%2F2004%2F01%2F009.

[56] D. J. Lange. "The EvtGen particle decay simulation package". In: *Nucl. Instrum. Meth.* A462 (2001), pp. 152–155. DOI: 10.1016/S0168-9002(01)00089-4.

[57] Christina Agapopoulou on behalf of the LHCb collaboration. "Commissioning LHCb's GPU high level trigger". In: *Journal of Physics: Conference Series* 2438.1 (Feb. 2023), p. 012017. DOI: 10.1088/1742-6596/2438/1/012017. URL: https://dx.doi.org/10.1088/1742-6596/2438/1/012017.

[58] "LHCb detector performance". In: *International Journal of Modern Physics A* 30.07 (2015), p. 1530022. DOI: 10.1142/S0217751X15300227. URL: https://doi.org/10.1142/S0217751X15300227.

[59] "LHCb magnet: Technical design report". In: (2000).

[60] *LHCb Upgrade GPU High Level Trigger Technical Design Report*. Tech. rep. Geneva: CERN, 2020. DOI: 10.17181/CERN.QDVA.5PIR. URL: https://cds.cern.ch/record/2717938.

[61] Mikołaj Misiak and Matthias Steinhauser. "Weak radiative decays of the B meson and bounds on $M_H^{\pm}$ mass in the Two-Higgs-Doublet Model". In: *The European Physical Journal C* 77.3 (2017). DOI: 10.1140/epjc/s10052-017-4776-y. URL: https://doi.org/10.1140%2Fepjc%2Fs10052-017-4776-y.

[62] E. Noether. "Invariante Variationsprobleme". ger. In: *Nachrichten von der Gesellschaft der Wissenschaften zu Göttingen, Mathematisch-Physikalische Klasse* 1918 (1918), pp. 235–257. URL: http://eudml.org/doc/59024.

[63] K.A. Olive. "Review of Particle Physics". In: *Chinese Physics C* 38.9 (Aug. 2014), p. 090001. DOI: 10.1088/1674-1137/38/9/090001. URL: https://dx.doi.org/10.1088/1674-1137/38/9/090001.

[64] F. Pedregosa et al. "Scikit-learn: Machine Learning in Python". In: *Journal of Machine Learning Research* 12 (2011), pp. 2825–2830.

[65] Antonio Pich. "The Standard Model of Electroweak Interactions; rev. version". In: (2008). DOI: 10.5170/CERN-2006-003.1. URL: https://cds.cern.ch/record/819632.

[66] J. Podolanski and R. Armenteros. "Analysis of V-events". In: *Phil. Mag.* 45 (1954), p. 13.

[67] Miguel Ramos Pernas. "Search for $K_S^0 \to \mu^+\mu^-$ and trigger developments at LHCb". Presented 24 Jul 2020. Santiago de Compostela U., 2020. URL: https://cds.cern.ch/record/2728965.

[68] A Brea Rodríguez. "Semileptonic Hyperon Decays at LHCb". In: *Journal of Physics: Conference Series* 1526.1 (Apr. 2020), p. 012022. DOI: 10.1088/1742-6596/1526/1/012022. URL: https://dx.doi.org/10.1088/1742-6596/1526/1/012022.

[69] E Santovetti. "The LHCb muon detector". In: *Nucl. Instrum. Methods Phys. Res., A* 462.1-2 (2001), pp. 297–300. DOI: 10.1016/S0168-9002(01)00127-9. URL: https://cds.cern.ch/record/506638.

[70] Erhard Schmidt. "Zur Theorie der linearen und nichtlinearen Integralgleichungen. I. Teil: Entwicklung willkürlicher Funktionen nach Systemen vorgeschriebener". In: *Mathematische Annalen* 63 (1907), pp. 433–476. URL: http://eudml.org/doc/158296.

[71] B. Sciascia. "Precision tests of the Standard Model with leptonic and semileptonic kaon decays". In: *Nuclear Physics B - Proceedings Supplements* 181-182 (Sept. 2008), pp. 83–88. DOI: 10.1016/j.nuclphysbps.2008.09.008. URL: https://doi.org/10.1016%2Fj.nuclphysbps.2008.09.008.

[72] Chien-Yeah Seng et al. "Improved Ke3 radiative corrections sharpen the Kμ2–Kl3 discrepancy". In: *Journal of High Energy Physics* 2021.11 (Nov. 2021). DOI: 10.1007/jhep11(2021)172. URL: https://doi.org/10.1007%2Fjhep11%282021%29172.

[73] M. Tanabashi et al. "Review of particle physics". In: *Phys. Rev.* D98 (2018), p. 030001. DOI: 10.1103/PhysRevD.98.030001.

[74] "The matter-antimatter asymmetry problem". In: (2014). URL: https://cds.cern.ch/record/1998489.

[75] Lei Wang, Jin Min Yang, and Yang Zhang. "Two-Higgs-doublet models in light of current experiments: a brief review". In: *Communications in Theoretical Physics* 74.9 (2022), p. 097202. DOI: 10.1088/1572-9494/ac7fe9. URL: https://dx.doi.org/10.1088/1572-9494/ac7fe9.

[76] Steven Weinberg. "Charge Symmetry of Weak Interactions". In: *Phys. Rev.* 112 (4 Nov. 1958), pp. 1375–1379. DOI: 10.1103/PhysRev.112.1375. URL: https://link.aps.org/doi/10.1103/PhysRev.112.1375.

[77] Lincoln Wolfenstein. "Parametrization of the Kobayashi-Maskawa Matrix". In: *Phys. Rev. Lett.* 51 (21 Nov. 1983), pp. 1945–1947. DOI: 10.1103/PhysRevLett.51.1945. URL: https://link.aps.org/doi/10.1103/PhysRevLett.51.1945.

[78] R. L. Workman et al. "Review of Particle Physics". In: *PTEP* 2022 (2022), p. 083C01. DOI: 10.1093/ptep/ptac097.

[79] C. S. Wu et al. "Experimental Test of Parity Conservation in Beta Decay". In: *Phys. Rev.* 105 (4 Feb. 1957), pp. 1413–1415. DOI: 10.1103/PhysRev.105.1413. URL: https://link.aps.org/doi/10.1103/PhysRev.105.1413.

GLOSSARY

ALICE A Large Ion Collider Experiment xiii, 17, 108

ATLAS A ToroidaL AparatuS xiii, 17, 43, 108

BSM Beyond the Standard Model 7, 9–12, 14, 106, 108

CMS Compact Muon Solenoid xiii, 17, 43, 108

LFU Lepton Flavor Universality 7, 8, 11, 14, 105, 107, 108

LHC Large Hadron Collider 17–19, 21, 28, 36, 101, 108

LHCb Large Hadron Collider beauty iii, v, xiii, 8, 13, 17–19, 28, 29, 35–40, 42, 43, 45, 48, 51, 54, 56–60, 65, 73, 80, 101, 102, 108–110

MC Monte Carlo 30, 33, 38–40, 45, 46, 48–50, 54, 55, 57, 58, 60–62, 64, 66, 67, 71–84, 86, 87, 89–95, 97, 98, 109–111

NP New Physics 7, 11, 14

PV Primary Vertex 19, 27, 68, 70

QCD Quantum Chromodynamics 8, 9

SHD Semileptonic Hyperon Decays 9

SM Standard Model 1–4, 6–12, 31, 36, 41, 45, 105, 106

SV Secondary Vertex 19

VELO Vertex Locator 21, 22, 27–29, 42–44

AGRADECIMENTOS

Poucas vezes temos a oportunidade de agradecer devidamente às pessoas que nos ajudaram a chegar onde estamos. No meu caso, formam uma lista considerável. Em primeiro lugar, quereria agradecer àqueles com quem dei meus primeiros passos na física e com quem ainda mantenho uma amizade valiosa: Fidel e Marcos Argibay.

À medusa Gabi, a Gonzalo e a Julián, que iniciaram o doutoramento comigo e com quem compartilhei os melhores momentos no IGFAE ao longo dos últimos seis anos.

A Miriam, Martino e Miguel, que me acolheram no lendário e agora extinto despacho 26 e que me ajudaram em tudo o que precisei até hoje.

E a Pablo, Asier, Moncho e Saul, que devolveram o pulso a esse 26 revitalizado, ao qual voltei depois da pandemia. Também a Marcos, meu elo ca nova guarda e o único responsável por todo elemento estético presente nesta tese.

Aos conveners do meu working group: Marta Calvi, Anna Lupato e Mark Smith, por dar-me a sua confiança para tomar diferentes responsabilidades dentro da colaboração e ajudar-me na procura do meu postdoc. Também a Rosen Matev e a Barbara Sciacia, por criar uma atmosfera de trabalho maravilhosa.

A Eloi, Erlantz, Pablo M. Agulló e Carlos, por iluminar aqueles três longos meses da minha estadia no CERN.

A Alessandra, Oscar, Verónica e Carlos que, junto com muitos dos já mencionados, foram a alegria das minhas manhãs.

A Abraham Gallas, por permitir-me conhecer à afetuosa pessoa por trás do implacável Team Leader e pela sua confiança em mim para a docência.

A María Vieites, pela sua ajuda altruísta corrigindo o material das minhas entrevistas e pelo tratamento amável que sempre me dispensou.

A Diego, o verdadeiro artífice das ideias mais valiosas desta tese.

A Adrián, meu companheiro nesta viagem de vidas paralelas.

Aos meus grandes amigos Manu, Keko, Diego E., Diego S., Vigo de Boqueixón, Carlos, Oja, Joe e Mosquera do BI, a Pastrana e a Abraham. Todos eles foram um pilar de apoio, muitas vezes sem sequer o saberem, afastando preocupações e tristezas dos meus dias.

A Alejandro e a Xabi, os homens da Terra Verde.

À minha família: avoa Sefa, avô Anxo, Martina, Laura, Silvia, Salomé e Marcos.

A Álvaro, meu grande amigo, com quem ressuscitei a poesia e a quem entrego a chave da cidade, agora que, após tanta resistência, me preparo para deixá-la.

É com as pessoas mais próximas que frequentemente desabafamos nossas preocupações. Por isso, minha mãe testemunhou meus piores momentos durante estes anos, que também foram complicados para ela. Por ser a principal responsável de todo o que sou, qualquer coisa que eu diga é insignificante comparado ao que ela merece.

A Iara, a pessoa que mais quero neste mundo.

Ao meu pai, com quem compartilhei todas as sextas-feiras desde que nasci.

Aos meus avós Alberto e Mari, com quem iniciei este caminho e que infelizmente não puderam ver o seu final. Gostaria tanto de poder mostrar-lhes até onde cheguei, pois só eles verdadeiramente entenderiam o que significa.

A Fati, meu apoio e felicidade, que leva aguardando que escreva para ela desde antes de que começasse a escrever esta tese. Passam os anos e os nossos futuros continuam entrelaçados.

Por último, a Xabi. A pessoa que me resgatou academicamente e que me permitiu voltar a acreditar em mim mesmo. Que me guiou passo a passo, ajudando-me a tomar sempre as melhores decisões. Com ele compartilhei os momentos mais elevados e também os mais duros deste caminho. Sem a sua ajuda, nada disto teria sido possível. Neste mundo acadêmico, onde muitas vezes perdemos a esperança nas pessoas, ele devolveu-ma.

Para rematar, lamento profundamente não ter dedicado o tempo que mereciam a todas as pessoas que quero. Se algo aprendi, é que nada justifica desaparecer para os demais.

Estou de volta.

Theoretical studies have demonstrated that Semileptonic Hyperon Decays (SHD) can be sensitive to Beyond the Standard Model dynamics that break leptonic flavour universality (LFU). The LFU test observable defined as the ratio between muon and electron modes is sensitive to non standard scalar and tensor contributions. Moreover there is a precise SM theoretical prediction.
$\Lambda \rightarrow p\ \mu\ \nu$ was proposed as one of the most promising SHD to be studied at LHCb, due to its high acceptance efficiency and abundance in LHCb events. In addition, the electron mode has already been measured precisely and an improvement in the measurement of the BR directly translates into tighter bounds in LFU in s-u quark transitions.
In this thesis is presented the blinded measurement of the branching fraction and its consequences.